DIODE LASER PUMPED 1645-nm Er:YAG LASERS

AS SOURCES FOR DIFFERENTIAL ABSORPTION

LIDAR METHANOMETRY

Geoffrey A. Wilson
B.S., Sonoma State University, Rohnert Park, California, 1984

A thesis submitted to the faculty
of the Oregon Graduate Institute of Science and Technology
in partial fulfillment of the
requirements for the degree
Master of Science
in
Applied Physics

November, 1989

The thesis "Diode Laser Pumped 1645-nm Er:YAG Lasers as Sources for Differential Absorption Lidar Methanometry" by Geoffrey A. Wilson has been examined and approved by the following Examination Committee:

_____
Richard A. Elliott, Advisor
Professor

_____
Richard K. DeFreez
Associate Professor

_____
Thomas M. Loehr
Professor

_____
Joel C. Johnson
Electro-Scientific Corporation

ACKNOWLEDGMENTS

Table of Contents

List of Figures

List of Tables

ABSTRACT

DIODE LASER PUMPED 1645-nm Er:YAG LASERS

AS SOURCES FOR DIFFERENTIAL ABSORPTION

LIDAR METHANOMETRY

Geoffrey A. Wilson, M.S.

Oregon Graduate Institute of Science and Technology, 1989

Supervising Professor: Richard A. Elliott

The purpose of this thesis is to design a diode laser pumped 1645-nm Er:YAG laser source for a DIfferential Absorption Lidar (DIAL) methanometer. Two major tasks are undertaken.

First, the absorption spectroscopy of methane and the methanometer performance requirements for a specific application are used to estimate the 1645-nm power needed. The application of coal mine methanometry is chosen to exemplify the design process because of its practical relevance and stringent source requirements (50 mW CW 1645-nm power with a 0.2-cm^{-1} linewidth).

Secondly, a model is developed to predict the pump power needed to obtain 50 mW output from an end-pumped Er:YAG laser, and how this may

be minimized with respect to the available design parameters. It is found that ≈800 mW of CW pump power with good beam quality are necessary.

The design of optical systems for efficiently coupling the pump beam to the gain medium is discussed. The design presented is about 80 % efficient, and thus ≈1 W of CW diode laser power is needed. It is observed that grating surface-emitting phased array diode lasers and edge-emitting phased array diode lasers operating in phase are the only potential candidates. Although no such devices capable of supplying 1 W of CW power have been reported to date, there is reason to believe they will soon be forthcoming.

1. INTRODUCTION

This thesis explores the possibility of using a diode laser pumped erbium-doped yttrium aluminum garnet (Er:YAG) laser emitting at 1645 nm as a light source for the optical detection of methane. It is the latest installment in a line of research begun in 1978 at Bethlehem Steel Corporation's Homer Research Laboratories (HRL) and continued[1] at the Oregon Graduate Institute of Science and Technology (OGI). A more complete discussion of the general problem can be found in Reference 1.

The ultimate goal is to develop a hand-held, real-time device for the remote detection and assay of methane gas, hereafter referred to as a methanometer. The DIfferential Absorption Light detection and ranging (DIAL) technique was chosen to satisfy safety and remote detection requirements.

The methanometer consists of a transmitter (laser light source) and a receiver (detectors and signal-processing electronics). Since these are contained in the same unit, which is small compared to the distances probed, the methanometer is "one-ended" and relies on backscattering to return some of the transmitted light to the receiver. The scope of this thesis is limited to the design of the transmitter. Receiver characteristics are considered only to the extent necessary to establish performance standards for the transmitter.

Tasks to which the proposed methanometer is well-suited include the assay of methane in coal mines and the detection of leaks along a natural gas pipeline. The former application requires spatial resolution and quantitative measurement with a relatively low sensitivity (≈ 1000 parts per million) to map the formation of potentially explosive pockets of methane. The latter is better served by greater sensitivity and rapidity of measurement to quickly locate a leak in a large search area, with quantitative measurement and spatial resolution having a low priority. The latter would have the significant advantage of utilizing relatively efficient backscattering from solid objects such as foliage or buildings, while the former would have to rely on Mie backscattering from coal dust particles. All factors considered, the coal mining application places more rigorous demands on the transmitter and is therefore specialized to for the remainder of the thesis.

Aside from use in a methanometer due to the fortuitous overlap of the 1645-nm emission line and a methane absorption line, the proposed laser is of little interest because of inherent inefficiencies. One favorable aspect is that this particular emission wavelength falls in the 1.4-2.0 μm eye-safe spectrum. When $\lambda < 1.4$ μm, retinal damage is a constant danger from a high-power, directional beam, especially an invisible infrared beam. In the eye-safe range, absorption is distributed along the optical path within the eye to minimize the possibility of injury. When $\lambda > 2.0$ μm, absorption occurs at the surface of the cornea and the danger of damage increases again[2].

Much research, particularly in the U.S.S.R., has been directed toward developing 2.9-μm Er:YAG lasers[3]. This has generated a considerable body of spectroscopic data which has aided in developing this thesis.

Chapter 2 gives a brief history of methane detection techniques to reveal the motivation for the research initiated at HRL. The absorption spectroscopy of methane is discussed, and prior research at HRL and OGI is summarized. Variously pumped 1645-nm Er:YAG lasers are compared, the advantages of diode laser pumping are mentioned, and the sources of inherent Er:YAG inefficiencies are identified.

The design of a methanometer for coal mine use is discussed in Chapter 3. It is shown that 50 mW of tunable, continuous-wave (CW) light at 1645 nm is sufficient to fulfill requirements[4] for such a device. Some details, notably the design of the tuning etalon, are outside the scope of this thesis and are not discussed.

Chapter 4 discusses the spectroscopy of Er:YAG and introduces a set of rate equations appropriate for finding the population inversion during simultaneous pumping at 788 nm and stimulated emission at 1645 nm. An approximate analytical expression for the gain is derived for use in Chapter 5. The measurement of the pump and stimulated wavelength cross-sections by absorption spectroscopy at OGI is discussed.

Chapter 5 presents a semi-quantitative argument to show that only the end-pumped geometry is consistent with the good match between the pump beam and the cavity mode needed to overcome the inherent inefficiencies. A more rigorous end-pumped rod model is developed, and computer-generated results are presented. It is estimated that nearly 800 mW of 788-nm pump light in a high-quality beam are needed to obtain 50 mW of output from an optimized Er:YAG laser. The model is modified for application to Nd:YAG, and is shown to yield results which compare well with experiment.

Concluding remarks and ideas for future research appear in Chapter 6.

Appendix A contains the source code and documentation for the FOR-TRAN programs used to generate numerical results in Chapters 4 and 5.

Appendix B discusses options for diode laser pumps and presents a formalism useful in the design of optical systems for coupling the pump to the Er:YAG rod. A coupling optics design for a 10-stripe phased-array diode laser pump is given. Large-aperture grating surface emitters are identified as promising pumps and discussed briefly.

Appendix C contains some clarifying remarks concerning the elliptical gaussian pump beam model introduced in Appendix B.

2. BACKGROUND

2.1 Existing Techniques for Methane Detection

The first semi-quantitative CH_4 detector was the flame safety lamp, first used in mines in 1816. A flame of known height in pure air is enhanced by the presence of CH_4 and retarded by a deficiency of O_2. Besides the obvious danger of the open flame causing an explosion, the device requires an experienced operator for correct interpretation.

Catalytic combustion methanometers offer some improvement[5]. CH_4 and O_2 are combined catalytically on a heated filament. The change of resistance of the filament is measured against an identical reference to determine the temperature rise, which is related to the heat of combustion, which is related to the CH_4 concentration. While the danger of an explosion is removed, the catalyst is easily poisoned and the device requires frequent calibration. Also, the response depends on the concentration of other inflammable gases and O_2.

LIght Detection And Ranging (LIDAR) techniques offer sensitivity, specificity and safety. In a one-ended LIDAR transceiver, laser light is transmitted into the atmosphere to be tested, the constituents of which are deduced from the backscattered light detected at the receiver, contained in the same unit. The three LIDAR techniques of Raman backscattering, resonance backscattering and DIfferential Absorption Lidar (DIAL) are reviewed elsewhere[6]. Of the three, only DIAL offers sufficient sensitivity for the detec-

tion of methane, because it takes advantage of backscattering from coal dust particles or solid objects depending on the application, both of which are far more efficient than Raman or Rayleigh backscattering from gas molecules.

DIAL works by tuning the transmitter alternately on and off an absorption line characteristic of and specific to the species to be detected. It is assumed that all effects are the same for the two closely spaced frequencies except for absorption by the species of interest, so that the ratio of the signals is related to the concentration.

Potential DIAL methane detection schemes should satisfy the following criteria:

1. The absorption line should be strong enough to give adequate sensitivity.

2. A suitable laser source emitting at the absorbed wavelength must be found.

3. The source must be rapidly tunable to a nearby wavelength where methane absorption is negligible to provide the reference signal.

4. Absorption by all other species at either wavelength should be negligible. The only infrared-active species that exist in appreciable concentrations in pure air are CO_2 and H_2O vapor. Coal gas is typically ≈ 99 % methane[1], so the presence of other hydrocarbons should not be troublesome.

2.2   Methane Infrared Absorption Bands

The CH_4 molecule belongs to the tetrahedral point group[7] whose high degree of symmetry yields only four fundamental vibrational transitions[8]: $\nu_1 = 2913.0$ cm^{-1}, $\nu_2 = 1533.3$ cm^{-1}, $\nu_3 = 3018.9$ cm^{-1} and $\nu_4 = 1305.9$ cm^{-1}. Of these, only ν_3 and ν_4 are infrared-active[7], although all enter into the

absorption spectrum as harmonics or sum frequencies. A general sum frequency can be denoted $A_1\nu_1+A_2\nu_2+A_3\nu_3+A_4\nu_4$, where the A's are integers. In the gas phase, each purely vibrational transition frequency is split into numerous narrow lines due to simultaneous transitions of the rotational quantum state of the molecule. A series of lines (branch) appears on either side of the purely vibrational transition frequency with approximately equal spacing between successive lines in each branch. The R (P) branch appears on the short- (long-) wavelength side and is caused by a unit increase (decrease) in the rotational quantum number. Purely vibrational lines are clustered in the center, forming the Q branch. Lines in the R and P branches are numbered from the center outward, starting with 0.

Except for ν_4 at $\lambda=7.66$ μm (at which no room-temperature lasers emit)[9], methane has no absorption bands at wavelengths longer than 4 μm, which can therefore be taken as the long-wavelength limit of the range to be searched for potential DIAL laser sources. The short wavelength limit is taken as 1 μm, because sum frequencies and harmonics consisting of three or fewer fundamentals have wavenumbers less than 10,000 cm^{-1} and those consisting of four or more are weakly absorbing and do not need to be considered.

Table 2.2.1, adapted from Herzberg[7], lists some absorption bands of interest.

These bands can be grouped into four spectral ranges, discussed in turn below. Each falls within spectral windows of the atmosphere[9]. The spectra shown in Figures 2.2.1-3 were generated from data given in the 1986

Table 2.2.1 Combination Bands of Methane			
Assignment	Energy in cm^{-1}	Wavelength in μm	Figure
$2\nu_4$	2600	3.85	2.2.1
$\nu_2+\nu_4$	2823	3.54	2.2.1
$2\nu_2$	3072	3.26	2.2.1
$\nu_2+2\nu_4$	4123	2.43	2.2.2
$\nu_1+\nu_4$	4216	2.37	2.2.2
$\nu_3+\nu_4$	4313	2.32	2.2.2
$\nu_2+\nu_3$	4546	2.20	2.2.2
$2\nu_3$	6006	1.66	2.2.3
$\nu_2+2\nu_3$	7514	1.33	

HITRAN database[10] using a program written by R. K. DeFreez. The following standard conditions were assumed: atmospheric pressure=1013 millibars, temperature=300 K, methane concentration×path length=3.2×10^{19} molecules/cm^2 (see Page 22 of Reference 1) and source linewidth=0.2 cm^{-1}. The source linewidth was chosen to match the atmosphere-broadened linewidth of methane[11] and is well within typical solid-state laser linewidth limitations.

All statements concerning the proximity of CO_2 and H_2O lines are based on inspection of Table V of Reference 10. CO_2 has no appreciable absorption lines in any of the four bands discussed. The examples of laser transmitters from existing DIAL schemes that are given are not intended to be exhaustive.

A. 3.3-μm Methane Absorption Range (Figure 2.2.1)

The most intense absorption in the 1-4 μm range occurs in the region 3.1-3.5 μm and is due to the ν_3 transition. The weaker lines spread over the range are due to the $2\nu_2$, $2\nu_4$ and $\nu_2+\nu_4$ transitions. Unfortunately, many strong H_2O absorption lines are also in this region and could interfere with methane detection. Nevertheless, a scheme based on an on-off pair of helium-neon lines separated by 0.9 cm^{-1} near 3.39 μm has been demonstrated[12].

B. 2.3-μm Methane Absorption Range (Figure 2.2.2)

The region 2.15-2.45 μm is filled with weak to moderate strength lines from the $\nu_2+2\nu_4$, $\nu_1+\nu_4$, $\nu_3+\nu_4$ and $\nu_2+\nu_3$ transitions. H_2O has no appreciable absorption lines in the region. No existing DIAL methane detection technique in this range was discovered by the author, but a possible scheme based on the Tm:YAlO$_3$ 2.318-μm line[13] is outlined below.

A diode laser could be used to pump the $^3H_6 \rightarrow ^3F_4$ transition at ≈ 780 nm. The Tm:YAG absorption band is of comparable strength to the Er:YAG absorption band[14] and the Tm:YAlO$_3$ band is presumably similar.

The transition of interest occurs from level 2 of $^3F_4$ to level 1 of the next lower manifold $^3H_5$. The calculated lifetime and radiative efficiency of $^3F_4$ are given in Table VI of Reference 13 as 770 μs and 0.89, respectively. The level-to-level stimulated cross-section can be estimated from the value for the manifold-to-manifold cross-section given in Table III of Reference 13 by dividing by $2J'+1$, the degeneracy of the lower manifold. This gives $\sigma_0 \approx 10^{-19}$ cm^2.

Figure 2.2.1   3.3 μm Methane Absorption Range

Tm:YAlO$_3$ line

Trans-
mission

Wavelength in microns
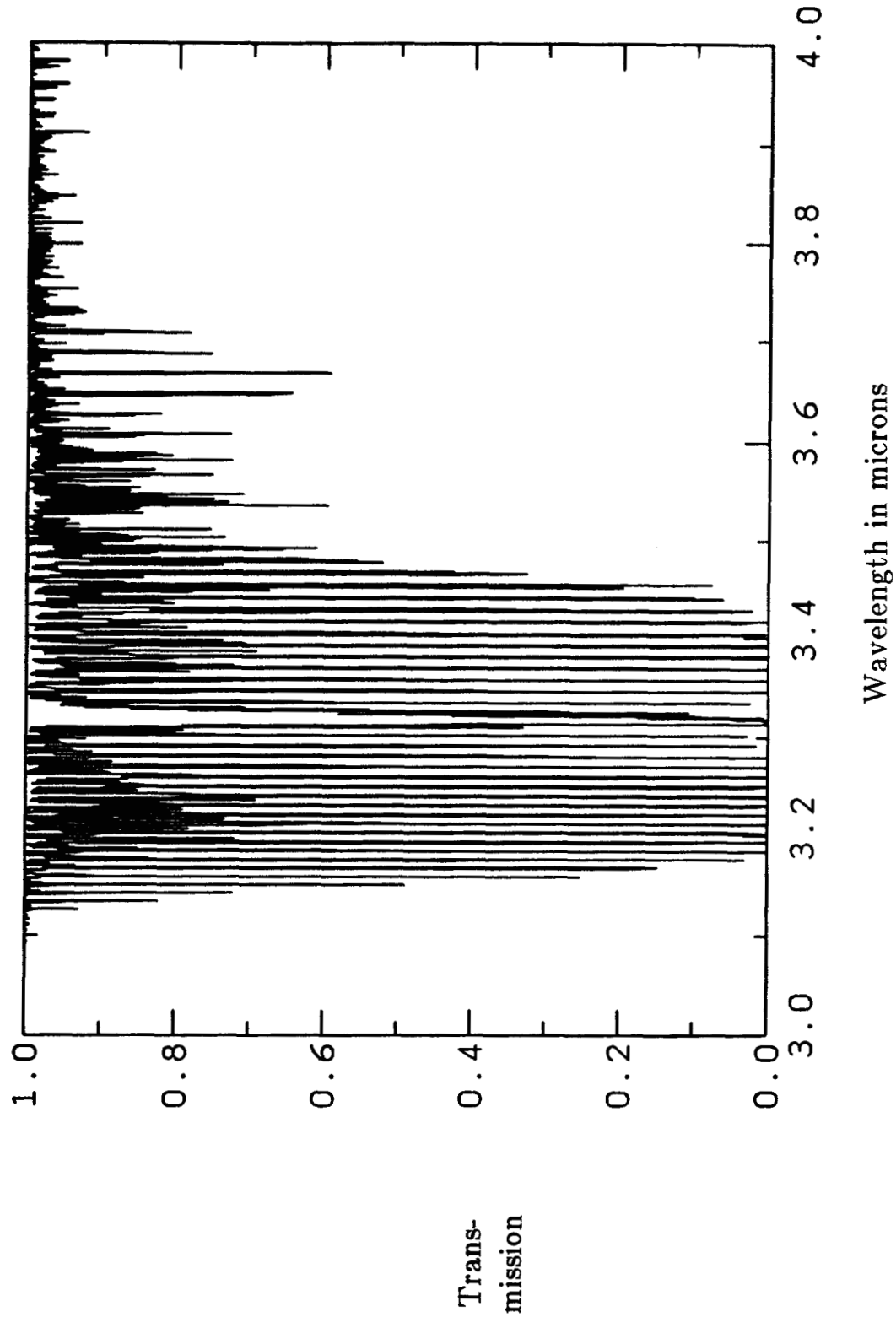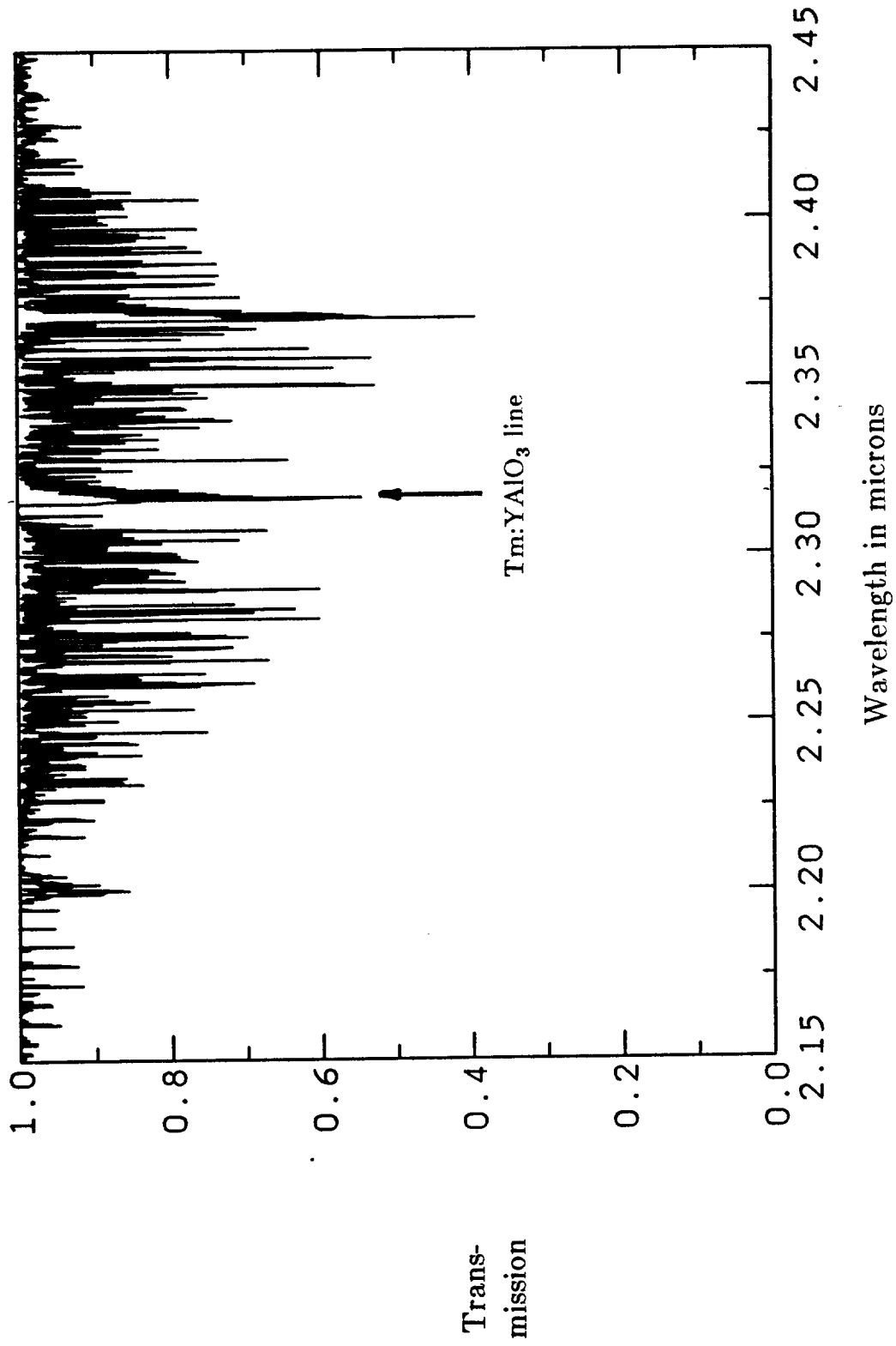
Figure 2.2.2   2.3 μm Methane Absorption Range

The real advantages are that 2.318-μm Tm:YAlO$_3$ is a four-level system, and that it appears that it would not suffer co-operative depopulation of the upper lasing level. Both of these are drawbacks to 1645-nm Er:YAG (see Section 2.4).

Potential drawbacks are the long lifetime of $^3H_4$ (4.8 ms) and and the possible lack of a methane absorption-free region within the fluorescence linewidth of Tm:YAlO$_3$, which is a DIAL technique requirement.

C. 1.66-μm Methane Absorption Range (Figure 2.2.3)

The $2\nu_3$ transition is responsible for these moderate strength lines. Several transitions in the 1.7-1.8 μm range have apparently not been studied and do not appear in the HITRAN database. H$_2$O has no appreciable absorption lines in the region.

The 1645 nm emission line of the Er:YAG laser coincides with the $2\nu_3$ R6 methane absorption line. Diode lasers with In$_{0.53}$Ga$_{0.47}$As active regions emit in the 1.62-1.66 μm region. Both have been used to detect methane and are discussed in Section 2.3.

D. 1.33-μm Methane Absorption Range

This band is due to the $\nu_2+2\nu_3$ transition. It has been recently studied[15] but does not appear in the 1986 HITRAN database. It is somewhat weaker than the $2\nu_3$ band. A remote methane monitor based on an InGaAsP LED and an optical fiber has been demonstrated[16]. Unfortunately, this scheme lacks the portability for mobile methane surveying. Another disadvantage is that 1.33 μm is not in an eye-safe region. These workers noted no interfer-
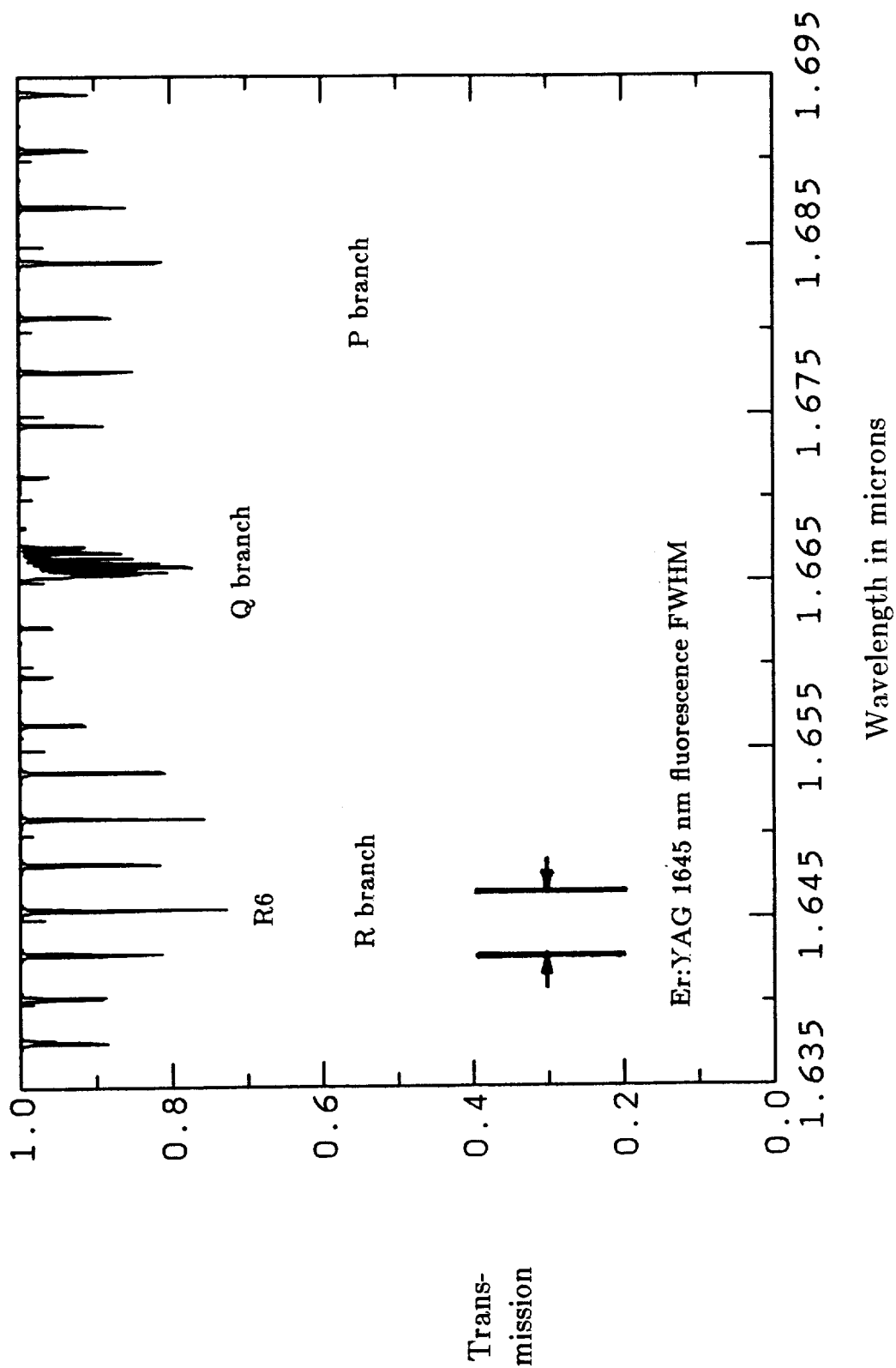
Figure 2.2.3   1.66 µm Methane Absorption Range

ence from H_2O lines.

2.3   Antecedents of this Research Project

The coincidence of the 1645-nm Er:YAG laser line and the $2\nu_3$ R6 methane absorption line was first noted in 1972[17]. In 1977 the need for remote methane detection was recognized at Bethlehem Steel Corporation. At the time, flash-lamp pumped Er:YAG DIAL was chosen as the most attractive technique[18]. Despite successful remote measurement of methane concentrations in a laboratory-simulated coal mine environment and actual coal mines[19], the transceiver was impractical as a final product because of its bulk and the danger of explosion caused by a high-voltage flash-lamp power supply.

Improvements in diode laser technology caused attention to shift to using lattice-matched $In_{0.53}Ga_{0.47}As/InP$ diode lasers as sources. These emit in the region 1.62-1.66 μm and are compact, rugged, efficient and capable of high power outputs without high voltage supplies. A study was conducted at OGI[20] which indicated that an InGaAs diode laser placed in an external diffraction grating tuned cavity might be an adequate source. This line of research[1] resulted in a device in 1985 which approximated source requirements.

A more rugged and electronically tunable source might be possible by using an InGaAs cleaved-coupled-cavity diode laser. These devices are made by cleaving a diode laser in the plane perpendicular to the optical axis and re-aligning the pieces so that they are optically coupled but electrically

isolated by a small air gap. Discrete tuning is possible by varying the injection currents to the sections to alter their mutual Fabry-Perot interference[21]. Interest at OGI soon settled on a related device, the micromachined-coupled-cavity diode laser. These are made by micromachining a small gap using a focused beam of Ga^+ ions[22], which removes the need for re-alignment and preserves the monolithicity of the device. Despite much effort by the present author, a suitable micromachined-coupled-cavity InGaAs diode laser source was not realized, due in large part to poor laser wafers.

With recent improvements in diode laser pumps for solid-state lasers[23], attention has returned to Er:YAG.

2.4 Progress Toward a Diode Laser Pumped 1645-nm Er:YAG Laser

Er:YAG laser emission at 1645 nm was first observed[24] using a rod cooled to 77 K and pumped by a helical xenon flashlamp. Pumping efficiency has since been increased by using the superior elliptical pump cavity geometry and co-doping with the sensitizer ytterbium, but remains a fundamental limitation for flashlamp-pumped devices.

Narrow-band pumps (lasers emitting at an Er:YAG absorption line) offer much greater pump quantum efficiencies. CW operation at room temperature using a Kr^+ laser pumping at 647.1 nm with a 200 mW threshold[25] and at 77 K using an F-center laser pumping at 1470 nm with a 50 mW threshold[26] have been reported. Another potential advantage is that laser pumped solid-state lasers have greater frequency stability than their flashlamp pumped

counterparts[27].

In other ways the pump lasers mentioned so far offer no advantages to flashlamps. They are at least as bulky, far more expensive, and also require high-voltage power supplies that could arc and ignite inflammable gases. It is natural to turn to diode lasers as pumps. Diodes are uniquely rugged, compact and efficient among lasers. They are relatively inexpensive and require no high-voltage power supplies or bulky cooling systems. A disadvantage is that their rapidly diffracting elliptical beams require complicated optics to couple efficiently to an end-pumped Er:YAG rod.

Diode lasers have been used to pump $\approx 1.6-\mu m$ Er:glass fiber lasers[28] with low thresholds (≈ 3 mW). This somewhat shorter wavelength results because the Stark splitting of the Er^{3+} ground manifold is not as great in glass as in YAG, and hence is of no use in methane detection.

Diode laser pumped 1064-nm Nd:YAG lasers have become commonplace[27]. Over 400 mW CW output from such a device has been reported[29]. In contrast, no diode laser pumped 1645-nm Er:YAG laser has yet been demonstrated. 1645-nm Er:YAG suffers by comparison to 1064-nm Nd:YAG in three ways:

1. Er:YAG is a three-level system: the lower lasing level is 523 cm^{-1} above the ground level[30] and has a significant thermal population at room temperature (kT$\approx$208 cm^{-1} at T=300 K). The lower lasing level of 1064-nm Nd:YAG is at 2111 cm^{-1} and has a negligible thermal population[31]. Near-room-temperature operation is unavoidable since substantial cooling of a hand-held device is impractical.

2. The stimulated-emission cross-section of 1645-nm Er:YAG is much smaller than that of 1064-nm Nd:YAG[31] (2.0×10^{-20} cm^2 vs. 6.5×10^{-19} cm^2).

3. A co-operative process between ion pairs depopulates the upper lasing level in competition with stimulated emission. No such process plagues 1064-nm Nd:YAG.

These problems cause the absorbed pump power density needed to maintain a population inversion to be quite high in erbium-based media. This favors reduction of the pumped volume. On the other hand, the pump beam absorption path cannot be made too short without sacrificing pump absorption efficiency. In bulk Er:YAG, pump beam diffraction makes these requirements just barely reconcilable at pump powers available from modern diode laser arrays. This explains the success of the Er:glass fiber lasers: transverse optical confinement allows small pumped volumes along with sufficiently long absorption paths, and excellent overlap between the pump beam and the cavity mode as well.

3. METHANOMETER DESIGN CONSIDERATIONS

The purpose of this chapter is to estimate the minimum transmitter power necessary for a coal mine methanometer to comply with performance standards. CW operation is assumed because the lifetime of the upper lasing level of 1645-nm Er:YAG is consistent with the so-called quasi-CW pulse length regime of diode lasers, in which thermal transients have equilibrated. Section 3.2 is specific to a range-resolving instrument and is included mainly to show that triangulation sufficient to fulfill the spatial resolution specification can be achieved in the dimensions of a hand-held device.

3.1 Theory of Operation

The proposed transceiver is shown in Figure 3.1.1. The diode laser pump (DL) is temperature-tuned to 788 nm by a thermo-electric cooler (TE). The pump light is focused by coupling optics (CO) onto the plano mirror (HR) of the plano-concave Er:YAG cavity, which is the 1645-nm high-reflectivity coated end of the Er:YAG rod (YR). The HR coating should be designed to have a small reflectivity at the pump wavelength.

The far end of the rod is 1645-nm anti-reflection coated (AR) to reduce cavity losses. The AR coating should be designed to have a high pump wavelength reflectivity to allow the pump beam a second pass through the rod. The rest of the cavity consists of a partially-reflecting concave output coupler (OC) and an etalon (ET) for tuning the laser wavelength.

LEGEND

DL - Diode laser pump
TE - Thermo-electric cooler
CO - Coupling optics
HR - High-reflectivity rod facet
YR - Er: YAG rod
AR - Anti-reflection rod facet
ET - Etalon
OC - Output coupler
TF - Transmitter folding mirror
TL - Transmitter lens
RI - Receiver lens
RF - Receiver folding mirror
Dp - Detector plane
D_1, D_2 - Detectors
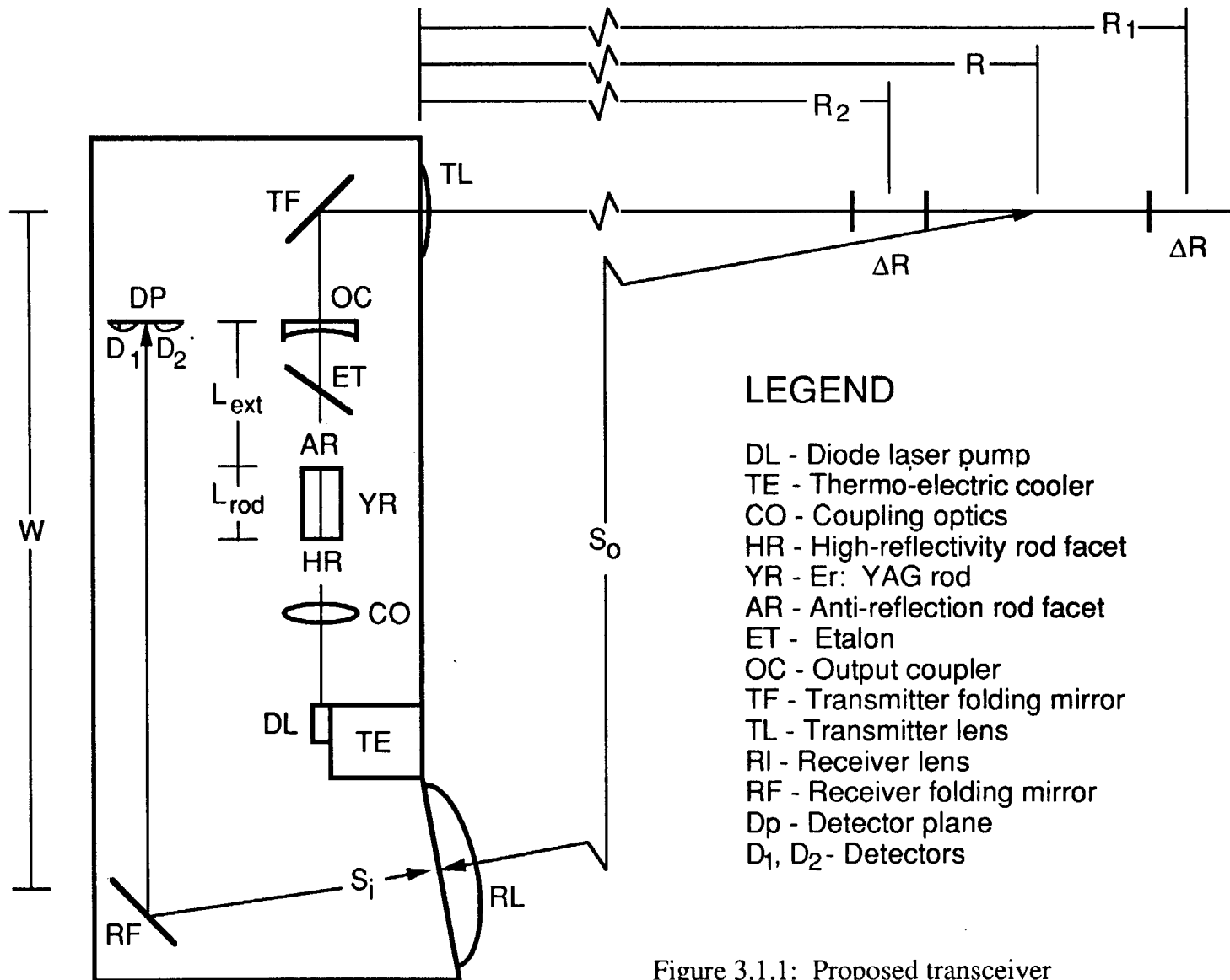
Figure 3.1.1: Proposed transceiver

The 1645-nm output is reflected by the transmitter folding mirror (TF) and collimated by the transmitter lens (TL) and leaves the unit. A portion backscattered by coal dust from the working distance R is focused by the receiver lens (RL) via the receiver folding mirror (RF) onto the detector plane (DP). DP consists of two active areas D_1 and D_2, which look at regions of length ΔR at R_1 and R_2, where R_1-R_2 is the transceiver spatial resolution. By taking the ratio of signals from the detectors, the average methane concentration over the path difference R_1-R_2 can be obtained.

The remaining sections in this chapter deal with various design issues. Table 3.1.1 summarizes the design parameter values used.

Table 3.1.1 Methanometer Design Parameters			
Parameter	Value	Reference	Comments
R	600 cm	1	20 ft. pillar spacing
R_1-R_2	30 cm	1	1 ft. resolution
ΔR	10 cm	assumed	non-overlapping regions
Φ_D	.02 cm	39	
w_0	33 μm	Section 5.5.B	
K	0.1	1 p. 60	receiver efficiency
β_{Mie}	15 km^{-1}	1 p. 59	40 mg/m^3 coal dust
Φ_{RL}	10 cm	assumed	
$\sigma_0(\lambda_{on})$	9.83x10^{-21} cm^2	Figure 2.2.3	

3.2   "Triangulation Width" and Receiver Lens Focal Length

The purpose of this section is to determine the triangulation width (W) and the receiver lens focal length (f_{RL}), to insure that they are consistent with the dimensions of a hand-held device. The apparent width of segment ΔR viewed from the receiver lens is

$$(\Delta R)_{app} = \frac{W}{R}\Delta R \qquad (3.2.1)$$

where it has been assumed that $W << R$ so that small-angle approximations can be used. This apparent width is the object that is imaged on the detector plane by the receiver lens. The image size should be equal to the detector diameter Φ_D. Geometrical optics gives

$$\frac{\Phi_D}{(\Delta R)_{app}} = \frac{S_i}{S_o} \approx \frac{f_{RL}}{R} \qquad (3.2.2)$$

since the conjugate ratio is near-infinite. Combining Equations 3.2.1 and 3.2.2 and evaluating gives

$$Wf_{RL} = \frac{R^2\Phi_D}{\Delta R} = 720 \text{ cm}^2 \qquad (3.2.3)$$

From Figure 3.1.1 it is reasonable to conclude that

$$W \approx 27 \text{ cm} \approx f_{RL} \qquad (3.2.4)$$

which is consistent with the dimensions of a hand-held methanometer.

3.3 Cavity Design and Transmitter Lens Focal Length

The standard relationship[31] exists between the radius of curvature of the output coupler (R_{OC}) and the cavity effective length (L_{cav})

$$w_0^2 = \frac{\lambda_0}{\pi}[L_{cav}(R_{OC}-L_{cav})]^{\frac{1}{2}} \quad L_{cav} \equiv \frac{L_{rod}}{n_{r,0}}+L_{ext} \qquad (3.3.1)$$

where $n_{r,0}$ is the index of refraction of YAG at 1645 nm (see Table 5.5.1).

The transmitted beam at R should be about as big as $(\Delta R)_{app}$, since then its image will fill the detectors in the dimension perpendicular to the plane of Figure 3.1.1. If f_{TL} equals the effective length from the 1645-nm high-reflectivity facet of the Er:YAG rod to the transmitter lens,

$$f_{TL} = L_{cav}+L_{OC-TL} \qquad (3.3.2)$$

the transmitted beam will be approximately collimated. The collimated waist size is given by Equation B.2.7 and can be set equal to half the object size (full width of the field of view of a detector at the working distance R)

$$w_c = \frac{\lambda_0 f_{TL}}{\pi w_0} = \frac{(\Delta R)_{app}}{2} \quad \rightarrow \quad f_{TL} = 14 \text{ cm} \qquad (3.3.3)$$

This gives plenty of room for the Er:YAG rod, the etalon, the output coupler and the transmitter folding mirror. Equation B.2.7 gives the confocal parameter of the collimated beam

$$b_c = \frac{\lambda_0 f_{TL}^2}{\pi w_0^2} = 970 \text{ cm} > R \qquad (3.3.4)$$

so that the beam stays adequately collimated over the required distance.

3.4   Etalon Requirements

The absorption linewidth of the 1645-nm Er:YAG transition was measured and found to be 4 nm (15 cm^{-1}) (see Section 4.5.B). The etalon should have a free spectral range of at least this to insure that only one longitudinal mode lases, and must be continuously tunable over at least half of a free spectral range so that the laser wavelength can be tuned to the methane $2\nu_3$ R6 line.

The etalon must have a finesse consistent with the 0.2 cm^{-1} emission linewidth assumed in this chapter and a line-center loss small compared to the round-trip extrinsic loss of $\delta_f = 0.01$ assumed for the numerical simulations of Section 5.5.

3.5   Ratio of Received Power to Transmitted Power

The RDIAL equation (Equation 5.1 of Reference 1) becomes

$$\frac{P_r(R)}{P_o} = \frac{K\beta_{Mie}\Delta R}{16} \frac{\Phi_{RL}^2}{R^2} = 2.6 \times 10^{-9} \qquad (3.5.1)$$

upon substitution of $\pi(\Phi_{RL}/2)^2$ for the receiver aperture area A.

3.6   Signal-to-Noise Ratio (SNR) Requirements

Equations C.28, C.6, C.11 and C.12 of Reference 1 combine to give the detector noise-to-signal ratio consistent with a methane concentration measurement accuracy of σ_C and spatial resolution of $R_1 - R_2$

$$\frac{\sigma_V}{V} = \sigma_{\overline{C}}(R_1 - R_2)\sigma(\lambda_{on}) \qquad (3.6.1)$$

where $\sigma(\lambda_{on})$ is the effective cross-section of the methane $2\nu_3$ R6 absorption line and is smaller than the line-center value $\sigma_0(\lambda_{on})$ because of the finite linewidth of the source.

Assuming that the absorption line and the emission line are coincident Lorentzians with line half-widths Δ_{R6} and $\Delta_{Er:YAG}$, respectively; the following can be shown

$$\sigma(\lambda_{on}) = \frac{\sigma_0(\lambda_{on})}{1 + \dfrac{\Delta_{Er:YAG}}{\Delta_{R6}}} \rightarrow \frac{\sigma_0(\lambda_{on})}{2} \qquad (3.6.2)$$

since $\Delta_{Er:YAG} = \Delta_{R6}$ has been assumed. $\sigma_0(\lambda_{on})$ can be obtained from Figure 2.2.3 with the help of Equation 4.5.2 and is given in Table 3.1.1.

Finally, $\sigma_{\overline{C}}$ must be evaluated. Table 5.1 of Reference 1 lists the required accuracy of the methanometer at several methane concentrations. The most stringent requirement is a reading of $\overline{C} = .25 \pm .15$ % in 8 out of 10 measurements when the true methane concentration is .25 %. Assuming a normal distribution, 8 out of 10 trials will fall within $\pm 1.33\sigma$ of the mean[32], so that

$$\sigma_{\overline{C}} = \frac{.0015}{1.33} \, 2.69 \times 10^{19} \text{ cm}^{-3} \qquad (3.6.3)$$

where the last factor is the concentration of gas molecules at 300 K and 1 atmosphere.

Evaluating Equation 3.6.1 gives $\sigma_V/V = .00447$ which implies that

SNR=223.

3.7 Tuning cycle, Detector NEP and SNR Improvement by Signal Averaging

Assume that D_1 and D_2 of Figure 3.1.1 are identical detectors of the type referred to on Page 62 of Reference 1. With a 5 MHz bandwidth (100 ns pulse), they have

$$NEP = \frac{10^{-(55 \text{ dBm}/10)} \text{ mW}}{11} = .29 \text{ nW} \qquad (3.7.1)$$

Assume that the etalon is capable of a tuning cycle rate of 10 KHz, and that this rate is sufficient to "freeze" atmospheric changes during a cycle. Assume that the tuning cycle consists of 10 μs in the "off" state, a 40 μs slew between the "off" and "on" states, a 10 μs "on" state and a 40 μs slew back to the "off" state. The increase by a factor of 100 in the sampling time corresponds to a factor of 10 reduction in the NEP. Multiplying the new NEP by the required SNR and dividing by the ratio given by Equation 3.5.1 gives the transmitted power required as P_o=2.5 W.

Assuming that this can be decreased by a factor of $N^{-\frac{1}{2}}$ if N cycles are averaged, 2500 cycles would be needed to reduce the transmitted power to the P_o=50 mW assumed henceforth. The entire measurement would take 1/4 second to complete, which is compatible with real-time methane surveying.

4. ER:YAG SPECTROSCOPY AND RATE EQUATIONS

4.1 Rare Earth 4f–4f Transitions

Erbium is one of the rare earth elements and as such has a partially filled 4f shell. The Er^{3+} 4f shell has 11 electrons and 3 vacancies.

The quantum state of the 4f shell electron configuration can be partially characterized by giving the term symbol

$$^{2S+1}L_J \quad \begin{bmatrix} L \\ L \end{bmatrix} = \begin{bmatrix} 0 & 1 & 2 & 3 & 4 & 5 & 6 & \cdots \\ S & P & D & F & G & H & I & \end{bmatrix} \tag{4.1.1}$$

where S (L) [J] is the spin (orbital) [total] angular momentum quantum number of the configuration. Each term symbol represents a "manifold" consisting of 2J+1 configurations.

An isolated Er^{3+} ion is spherically symmetric and so the configurations within a manifold are energy degenerate. When the Er^{3+} replaces an Y^{3+} in YAG, the static fields at the lattice site break the symmetry, lifting the intra-manifold degeneracy. In rare earth ions, the 4f electrons are partially shielded from external fields by outer electrons. This causes the energy splitting of manifolds to be less than that of the transition elements, and to have less sensitivity to the choice of host crystal and inhomogeneities within the crystal. The latter effect is manifested in the characteristically sharp lines of rare earth spectra.

Another effect of the crystal fields is to allow electric dipole transitions

among the 4f configurations. These are forbidden in the isolated ion because the 4f configurations all have the same parity. The crystal fields admix 4f wavefunctions with those of opposite parity such as 5d to obtain 4f-like eigenstates with mixed parity that have non-vanishing matrix elements with the electric dipole operator.

4.2 Er:YAG

$Y_3Al_5O_{12}$ (Yttrium Aluminum Garnet or YAG) is the most commonly used crystalline solid-state laser host. Er^{3+} can be added to the melt as a dopant, replacing Y^{3+} at some lattice sites. Because of the similar radii of the two ions, any alloy $Er_xY_{1-x}AG$ $0 \leq x \leq 1$ can be grown with good quality. This contrasts with Nd:YAG, where the concentration of Nd^{3+} cannot exceed ≈ 1 atom % because of size mismatch induced lattice strain. Heavily-doped Er:YAG has the advantage of greater pump light absorption, but is plagued by undesired co-operative energy transfer processes between Er^{3+} ions. Furthermore, because the crystal fields change with concentration x, heavily-doped Er:YAG may not have the fortuitous overlap of an emission line with a CH_4 absorption line, as does lightly-doped Er:YAG. Henceforth, "Er:YAG" will refer to material with $x \leq 0.1$.

The eight lowest-lying Er:YAG manifolds are shown in Figure 4.2.1. The lowest four are of particular interest in diode-pumping and are numbered 0,1,2,3 in order of increasing energy for brevity of subscripts. Each manifold consists of $J + \frac{1}{2}$ levels, each level containing two degenerate $(M_J, -M_J)$ states. If the levels within a manifold are numbered in order of increasing energy
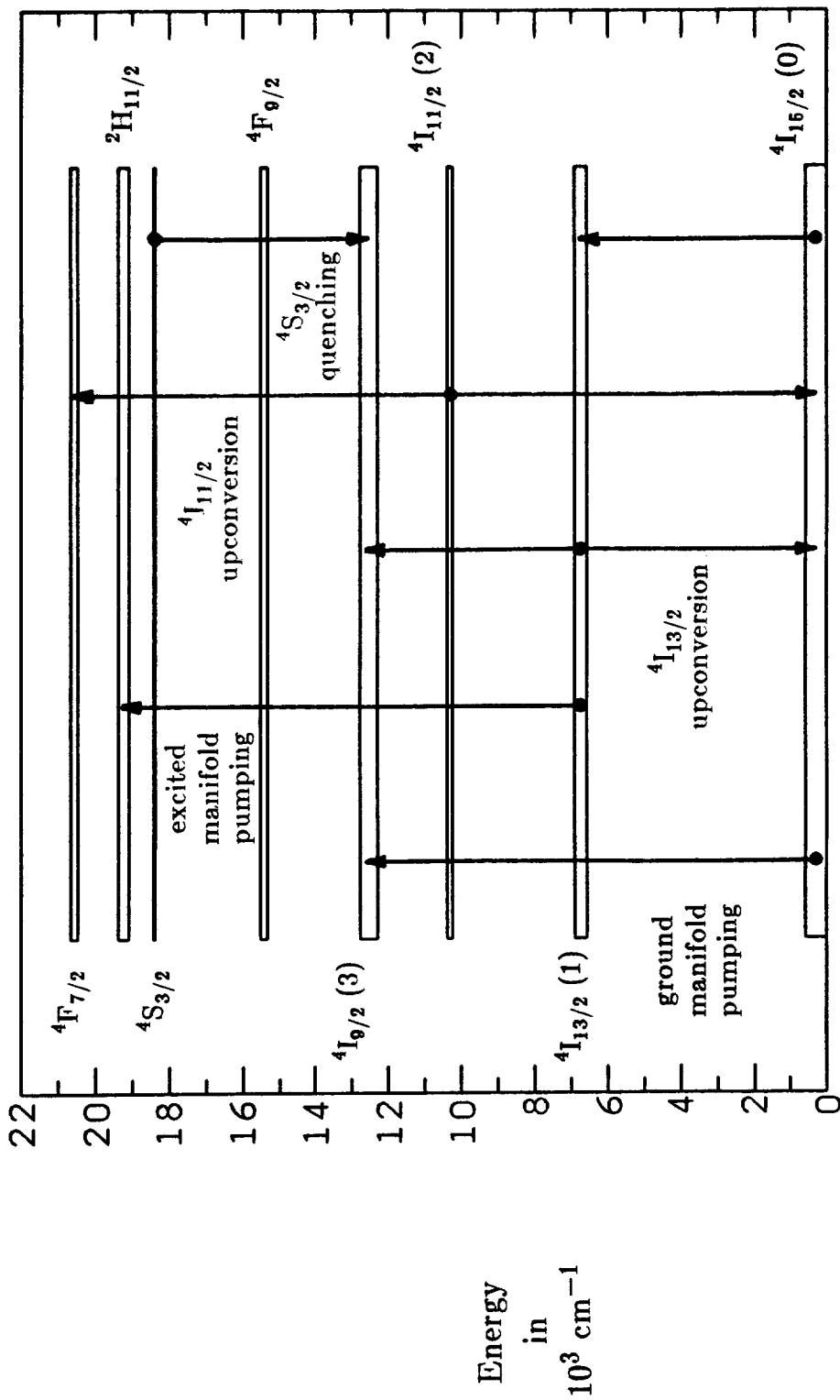
Figure 4.2.1   Low-lying Er:YAG Manifolds

starting with 1, then any level can be referred to by the ordered pair (manifold,level). The lower lasing level is (0,7) at 523 cm^{-1} and the upper lasing level is (1,3) at 6602 cm^{-1}, relative to (0,1) at 0 cm^{-1} at room-temperature[30]. The primary reason for choosing YAG as the host is the large ground manifold splitting that stretches the manifolds 0→1 transition spectrum to long enough wavelengths to overlap with the CH_4 1.66-μm absorption band. YAG has the largest ground manifold splitting of known solid-state laser hosts[33] with the exception of LuAG[30].

It is assumed throughout this work that intra-manifold relaxation is so rapid that the ratio of the population of (M,i) to the population of the entire Mth manifold is given by a Boltzmann factor[34]

$$f_i \equiv \frac{\exp(-E_i/kT)}{\sum\limits_{\text{manifold}} \exp(-E_m/kT)} \tag{4.2.1}$$

The Boltzmann factors for the lower and upper lasing levels at T=300 K are f_a=.0214 and f_b=.209, respectively. Note that the lower lasing level has a much larger thermal population than four-level systems such as 1064-nm Nd:YAG, making a population inversion difficult to achieve. YAG minimizes this problem because of its large ground manifold splitting, noted above.

The ratio of the rate at which ions in an excited manifold decay to a particular lower manifold and the rate at which they decay from the excited manifold to all the lower manifolds is called the "branching ratio" for the pair of manifolds. The lifetimes and branching ratios of the three lowest-lying excited manifolds are listed in Table 4.2.1.

Table 4.2.1 Manifold Lifetimes and Branching Ratios					
From	To	Calculated [40 Table 4]		Observed	
Manifold	Manifold	Radiative Branching Ratio	Radiative Lifetime in ms	Manifold Lifetime in ms	Effective Branching Ratio
1	0	1	7.3	6.4 [Figure 4.2.2]	1
2	0 1	.802 .198	8.8	.10 [Figure 4.2.3]	.01 .99
3	0 1 2	.769 .215 .016	4.3	$\approx$.001 [41]	.0002 .00005 $\approx$1

The discrepancy between τ_{rad}(calc) and τ(obs) is due to multiple-phonon-mediated non-radiative relaxation to the next lower-lying manifold. It is clear that at room temperature non-radiative processes dominate the relaxation of all the manifolds except manifold 1 ($^4I_{13/2}$).

The short lifetimes of manifolds 2 and 3 allow the rapid population of manifold 1 by diode-pumping Er^{3+} ions from the ground manifold 0 to manifold 3. The observed lifetime of the $^4I_{11/2}$ manifold (τ_2) is much smaller in YAG than in other garnets, e.g. τ_2(Er:YSGG)=2.25 ms, because the higher phonon cut-off frequency of aluminum-containing garnets increases the upper energy limit for multi-phonon decay[25]. This is another advantage of YAG in the present application.
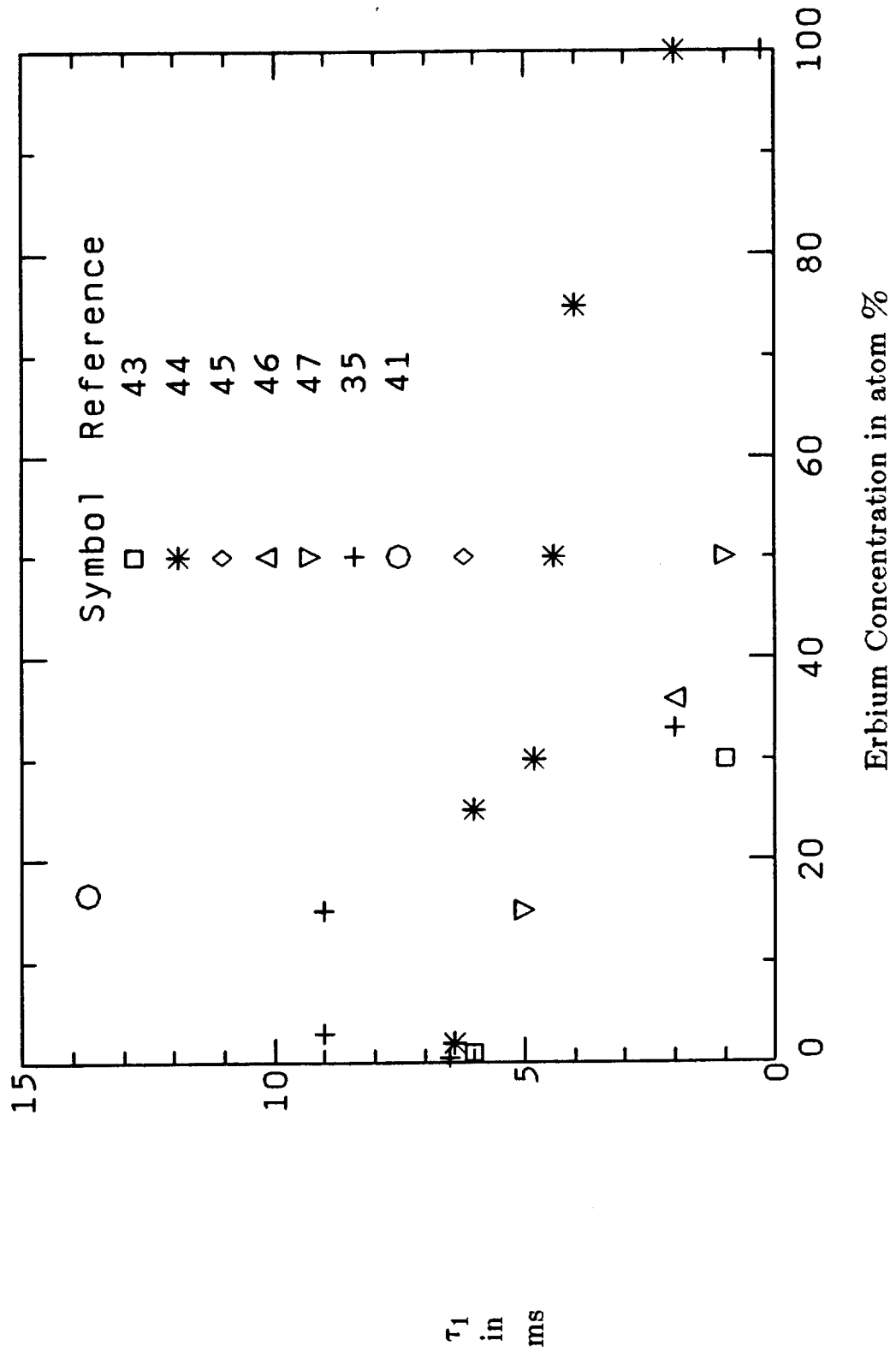
Figure 4.2.2 τ_1 Literature Values
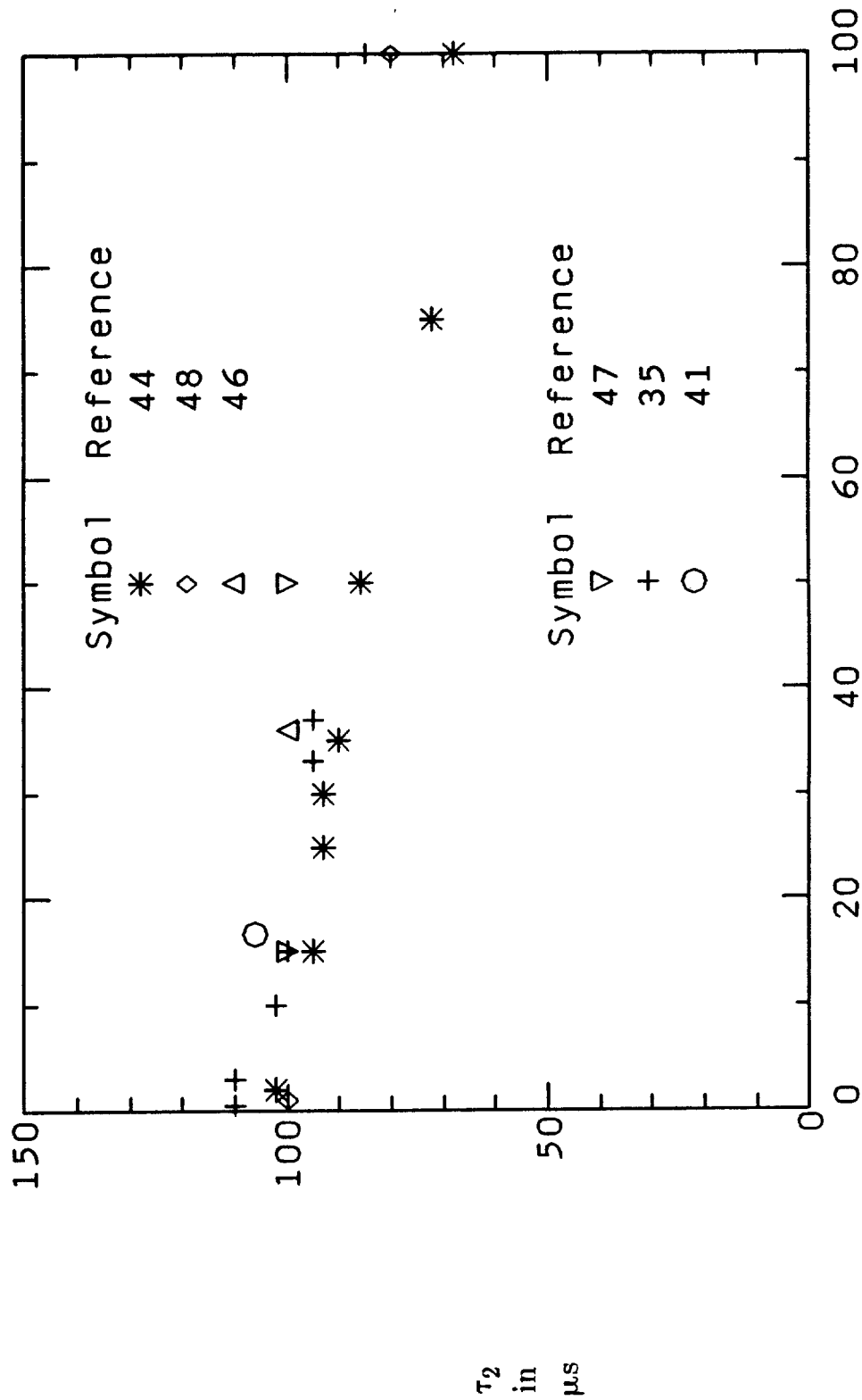
Figure 4.2.3 τ_2 Literature Values

The long lifetime of manifold 1 is a favorable factor, but unfortunately another depopulation mechanism exists. The excitation energy of one $^4I_{13/2}$ ion can be transferred non-radiatively to another similarly excited ion nearby. The energy donor drops to the ground manifold and the energy acceptor is promoted to the $^4I_{9/2}$ manifold. This process is known as "co-operative upconversion" and is common among rare earth ions wherever energy differences of the participating manifolds match to within several hundred cm^{-1}.

4.3 Rate Equations

In the following, N is the Er^{3+} concentration, N_i is the population density of the ith manifold, and τ_i is the observed relaxation lifetime of the ith manifold.

The rate equations are:

$$\frac{dN_0}{dt} = -\frac{\eta_a \rho_a}{h\nu_p} + \frac{N_1}{\tau_1} + W_1 N_1^2 + 2\frac{I_c}{h\nu_0}\sigma_0(f_b N_1 - f_a N_0) \quad (4.3.1)$$

$$\frac{dN_1}{dt} = -\frac{N_1}{\tau_1} + \frac{N_2}{\tau_2} - 2W_1 N_1^2 - 2\frac{I_c}{h\nu_0}\sigma_0(f_b N_1 - f_a N_0) \quad (4.3.2)$$

$$\frac{dN_2}{dt} = -\frac{N_2}{\tau_2} + \frac{N_3}{\tau_3} \quad (4.3.3)$$

$$\frac{dN_3}{dt} = +\frac{\eta_a \rho_a}{h\nu_p} - \frac{N_3}{\tau_3} + W_1 N_1^2 \quad (4.3.4)$$

$$N_0 + N_1 + N_2 + N_3 = N \quad (4.3.5)$$

Note that Equation 4.3.5 is redundant. The various processes included in the rate equations, as well as some that are neglected, are categorized and discussed below.

A. Diode laser pumping

The first terms on the right-hand sides of Equations 4.3.1 and 4.3.4 are the local pumping rate per unit volume. η_p is the pump quantum efficiency, ρ_a is the local absorbed pump power density, and $h\nu_p$ is the pump photon energy.

Absorption lines corresponding to transitions between the lower four levels of $^4I_{15/2}$ and $^4I_{9/2}$ lie in the range 783-819 nm. The upper four levels of $^4I_{15/2}$ are too sparsely populated at room temperature to be pumped efficiently. Several overlapping transitions form an absorption band at 788 nm with a FWHM of 1.7 nm. Measurement of the peak absorption coefficient is discussed in Section 4.5.

The pumping of $^4I_{13/2}$ ions to the $^2H_{11/2}$ manifold appears possible because of the overlap of this absorption band with the chosen pump wavelength 788 nm. The closest absorption lines on either side are expected at 785 nm and 794 nm, calculated using $^2H_{11/2}$ energy levels extrapolated from those given by Kaminskii et. al[30]. for Er:LuAG at 77 K to Er:YAG at 300 K. Since these are far from 788 nm compared to a typical diode laser emission band half-width, excited-state pumping can be neglected.

B. Ordinary relaxation decay

Terms of the form N_i/τ_i represent the ordinary relaxation of excited ions

into the next-lower manifold. For the reasons given in Section 4.2, the direct relaxations 2→0, 3→0 and 3→1 can be neglected. This greatly simplifies the rate equations.

C. Co-operative upconversion

The co-operative upconversion depopulation of manifold 1 has been incorporated into the rate equations by adding the term $W_1 N_1^2$, where W_1 is an experimentally determined coefficient. The N_1^2 dependence of the term anticipates a bi-atomic process so that W_1 is expected to be Er^{3+} concentration independent, which turns out not to be the case[35]. The determination of W_1 is discussed in Section 4.5.

The co-operative process may be microscopically reversible, the reverse reaction being included as the term $W_1 N_0 N_3$. It turns out that this term is always small compared to N_3/τ_3 in the concentration range of interest and may be neglected.

Two other co-operative processes have been noted[35] but are not included in the rate equations. One is the co-operative depopulation of the $^4I_{11/2}$ manifold ($^4I_{11/2}+{}^4I_{11/2}-{}^4I_{15/2}+{}^4F_{7/2}$). This process is thought to be responsible for the anti-Stokes fluorescence of the $^2S_{3/2}-{}^4I_{15/2}$ transition observed at 540-560 nm when Er:YAG is pumped at a longer wavelength, e.g. with a Kr^+ 647.1-nm laser[36]. The process can be written as $W_2 N_2^2$. W_2 has been found[35] to be comparable to W_1, but because of the short lifetime of the $^4I_{11/2}$ manifold, this process is negligible compared to N_2/τ_2 relaxation to the $^4I_{13/2}$ manifold for Er^{3+} concentrations less than 10 atom %.

The other co-operative process $(^2S_{3/2}+^4I_{15/2}-^4I_{9/2}+^4I_{13/2})$ is thought to be responsible for concentration quenching of the $^2S_{3/2}$ fluorescence. It can be neglected in this application because no means for populating the $^2S_{3/2}$ manifold have been allowed.

D. 1645-nm absorption and stimulated-emission

The last term on the right-hand side of Equations 4.3.1 and 4.3.2 takes absorption and stimulated-emission at the lasing wavelength into account. I_c is the local intensity of the stimulated radiation, $h\nu_0$ is the 1645-nm photon energy and σ_0 is the transition cross-section. The factor of 2 is included to take both counter-propagating waves into account, assuming that they are of equal intensity. The measurement of σ_0 is discussed in Section 4.5.

4.4   Steady-State Rate Equation Solutions

Henceforth, the steady-state $(dN_i/dt=0)$ forms of Equations 4.3.1-4 are considered. N_3 can be neglected in Equation 4.3.5, which can then be used to eliminate N_2 in Equation 4.3.2. Equations 4.3.1 and 4.3.2 can then be written

$$An_1^2 + (1+Y)n_1 = (GY+X^2)n_0 \qquad (4.4.1)$$

$$2UAn_1^2 + (1+U+UY)n_1 = 1 + (1-UGY)n_0 \qquad (4.4.2)$$

where $n_i \equiv N_i/N$, and

$$A \equiv \tau_1 N W_1 \qquad (4.4.3)$$

$$G \equiv \frac{f_a}{f_b} \qquad (4.4.4)$$

$$U \equiv \frac{\tau_2}{\tau_1} \qquad (4.4.5)$$

$$X^2 \equiv \frac{\lambda_p}{hc} \frac{\eta_a \tau_1}{N} \rho_a \qquad (4.4.6)$$

$$Y \equiv 2 \frac{\lambda_0}{hc} \sigma_0 \tau_1 f_b I_c \qquad (4.4.7)$$

where X^2 is the dimensionless pumping strength and Y is the dimensionless stimulated emission. If the inversion threshold (transparency) condition

$$n_{1,inv} = G n_{0,inv} \qquad (4.4.8)$$

is imposed, the following relationships are obtained

$$2UAG^2 n_{0,inv}^2 + [1+(1+U)G]n_{0,inv} - 1 = 0 \qquad (4.4.9)$$

$$X_{inv}^2 = G(1+An_{1,inv}) \qquad (4.4.10)$$

where X_{inv}^2 is the pumping strength needed to reach inversion threshold. For a high Q cavity, the lasing threshold is expected to be not much greater than the inversion threshold. Therefore, the inversion populations can be used as estimates for the lasing threshold populations, particularly to verify that the neglected processes were indeed negligible. The other manifold populations are then given by

$$n_{2,inv} = U n_{1,inv}[1+2An_{1,inv}] \qquad (4.4.11)$$

$$n_{3,inv} = \frac{\tau_3}{\tau_2} n_{2,inv} \qquad (4.4.12)$$

This model turns out to be limited by the validity of the assumption

$2W_2N_2^2 \ll N_2/\tau_2$. Using $W_1 = 1.8 \times 10^{-17}$ cm^3/s and $W_2 = 5.1 \times 10^{-17}$ cm^3/s for $N = 1.38 \times 10^{21}$ cm^{-3} (10 atom %)[35], it is found that the neglected process has grown to $\approx 1/3$ the rate of the relaxation process at inversion threshold. Therefore, an Er^{3+} concentration of 10 atom % constitutes the approximate upper bound of the applicability of the model.

For arbitrary pumping, n_1 is the solution of

$$A[1 + UGY + 2UX^2]n_1^2 + [1 + (1+G)Y + (1+U)X^2 + UYX^2]n_1$$

$$= GY + X^2 \tag{4.4.13}$$

with

$$n_0 = \frac{1 - [1 - U - UY]n_1}{1 + UGY + 2UX^2} \tag{4.4.14}$$

Define

$$\Delta \equiv n_1 - Gn_0 = \frac{[1 + (1-U)G + 2UX^2]n_1 - G}{1 + UGY + 2UX^2} \tag{4.4.15}$$

so that the inversion population density in cm^{-3} is $Nf_b\Delta$. The end-pumped rod model developed in Chapter 5 requires a linear approximation for Δ so that $P_i(P_o)$ can be solved for. It is found that the linear expansion of $\Delta(X, Y)$ about the point (X_{inv}, Y) gives an adequate fit in the regime of interest, 1 atom % $\leq N \leq$ 10 atom % and $X_{max} \leq 5X_{inv}$. Accordingly,

$$\Delta \approx \Delta_{inv} + \left[\frac{\partial \Delta}{\partial X}\right]_{inv}(X - X_{inv}) \equiv \chi(Y)[X - X_{inv}] \tag{4.4.16}$$

where by definition $\Delta_{inv} = 0$. Evaluating χ yields

$$X = \frac{(1+G-UG+2UX_{inv}^2)[\partial n_1/\partial X]_{inv}+4UX_{inv}n_{1,inv}}{1+UGY+2UX_{inv}^2} \qquad (4.4.17)$$

where

$$\left[\frac{\partial n_1}{\partial X}\right]_{inv} = 2X_{inv} \times \qquad (4.4.18)$$

$$\frac{[1-(1+U)n_{1,inv}-2UAn_{1,inv}^2]+[Un_{1,inv}]\ Y}{[1+(1+U)X_{inv}^2+2A(1+2UX_{inv}2)n_{1,inv}]+[1+G+UX_{inv}^2+2AUGn_{1,inv}]\ Y}$$

Δ and its linear approximation are plotted as functions of X/X_{inv} for $Y=0$ for $N=1$, 4 and 10 atom % in Figures 4.4.1-3. In the range $0 \leq X/X_{inv} \leq 5$, Δ is slightly underestimated when $N=1$ atom %, slightly overestimated when $N=4$ atom % and considerably overestimated when $N=10$ atom %. For $X/X_{inv} > 5$, the approximation is poor in all cases.

4.5   Determination of Key Er:YAG Parameters

The Er:YAG sample used in the absorption spectroscopy measurements is a 63.5 mm $\times$ 3 mm diameter rod doped with 0.4 atom % Er and 5 atom % Yb[37]. The rod was originally used in a flash-lamp pumped laser, and Yb was added to enhance pump light absorption. Since Yb:YAG has no absorption lines in the bands of interest, the presence of Yb was neglected.

A. Measurement of the Pump Wavelength Absorption Coefficient

σ_p is defined as the Er:YAG absorption coefficient at 788 nm normalized to the Er^{3+} concentration. The setup used for these measurements is shown in Figure 4.5.1. The Er:YAG rod was placed between the exit slit of the
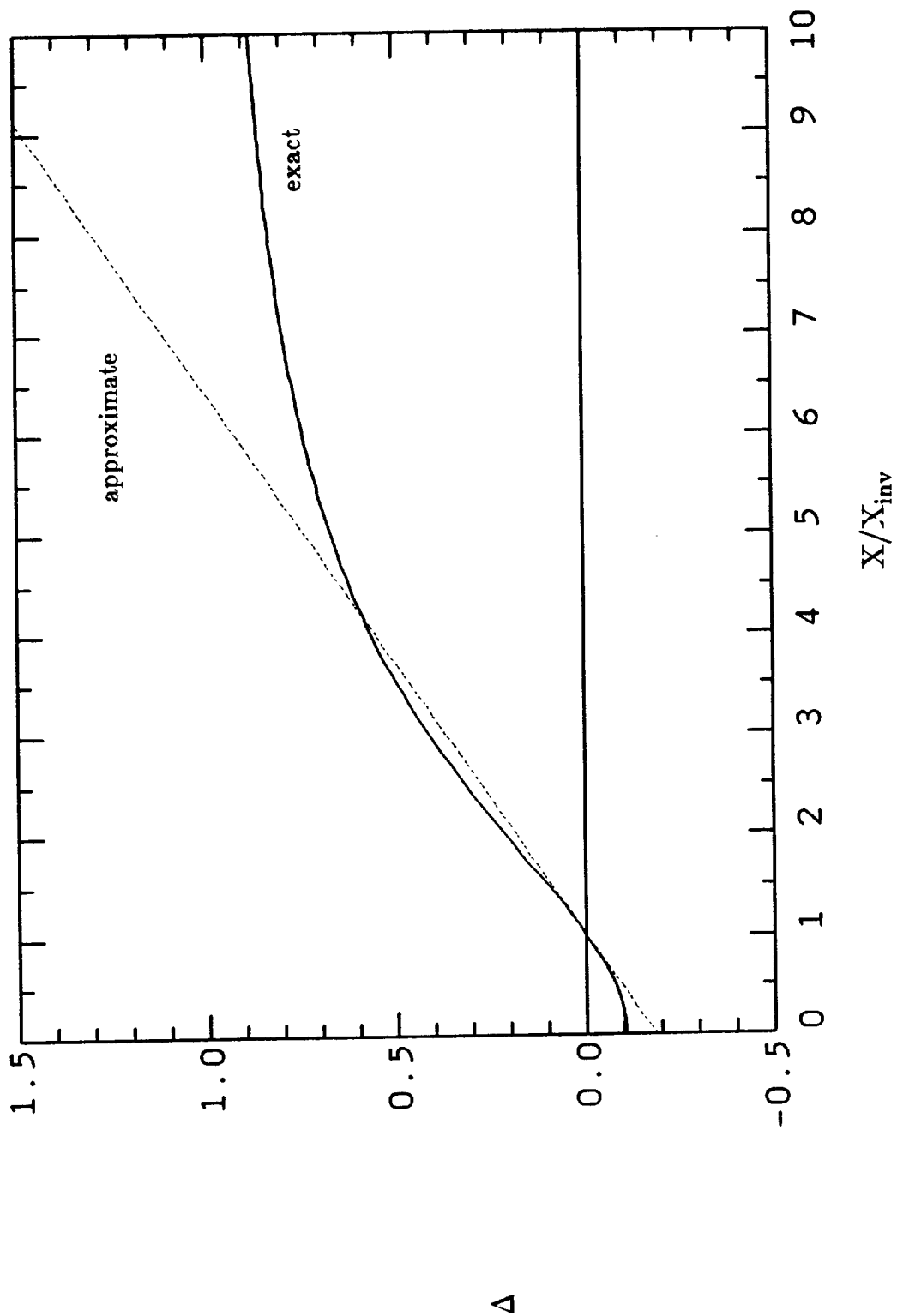
Figure 4.4.1   Exact and Approximate Inversions, N=1 atom %
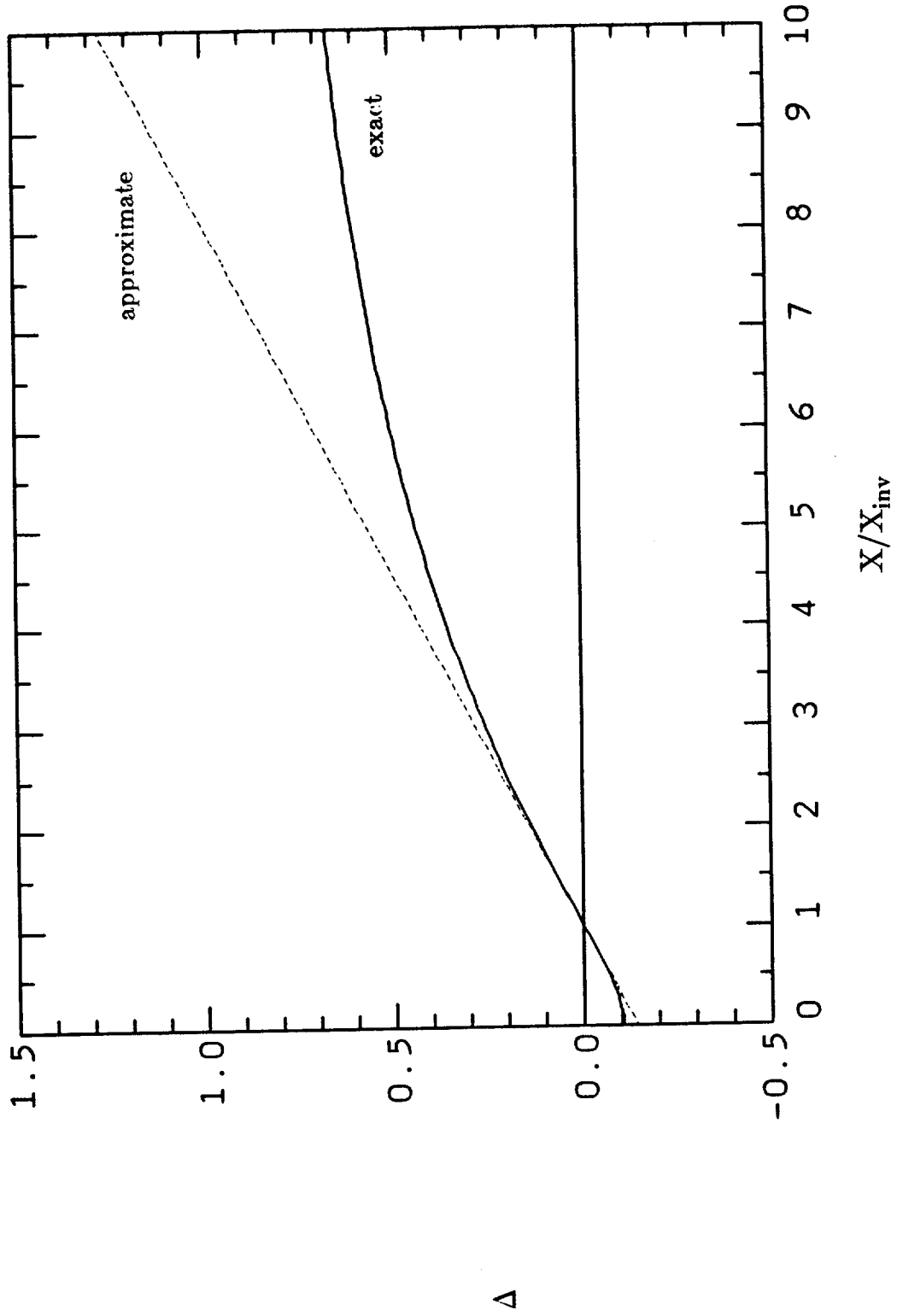
Figure 4.4.2   Exact and Approximate Inversions, N=4 atom %
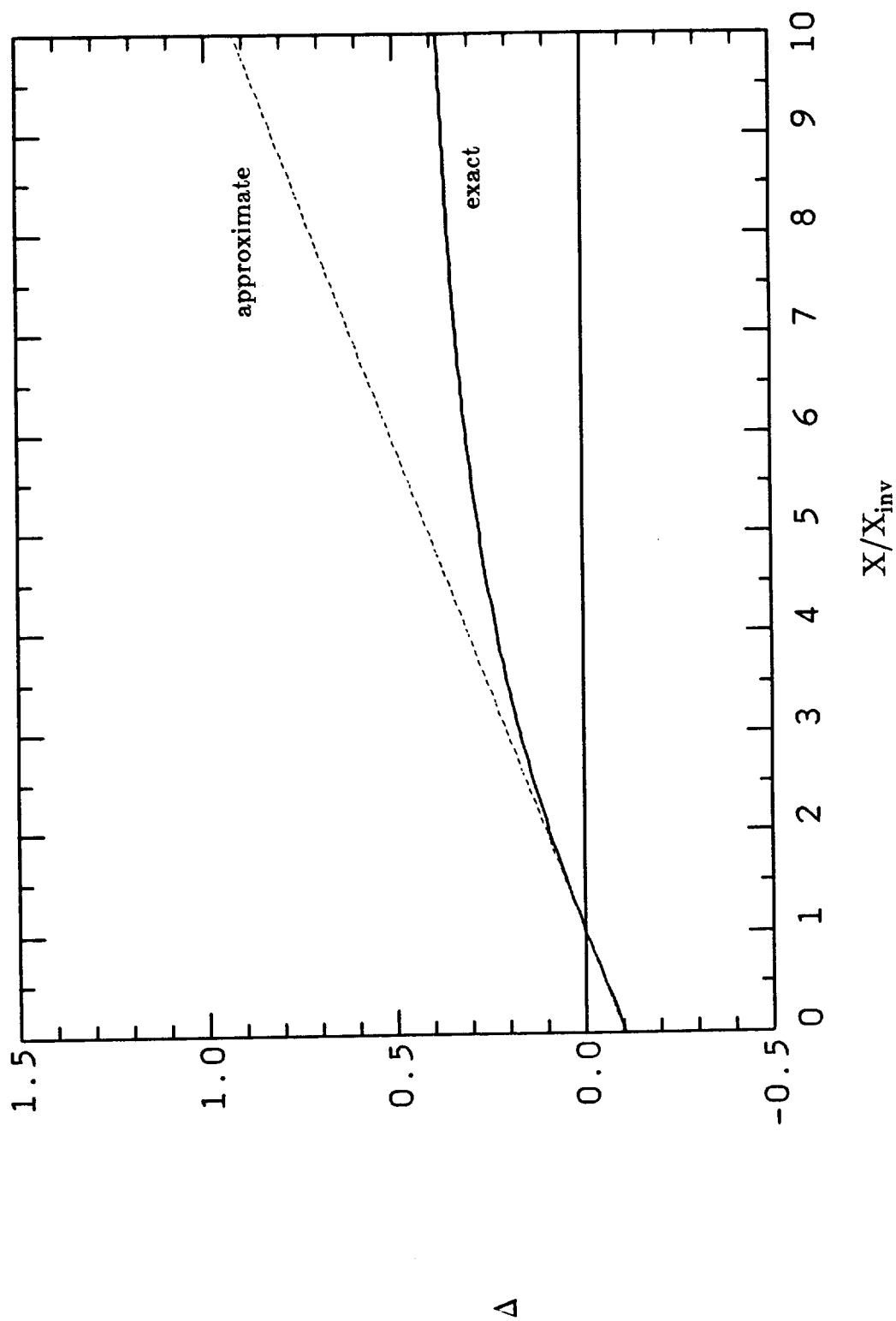
Figure 4.4.3   Exact and Approximate Inversions,   N=10 atom %
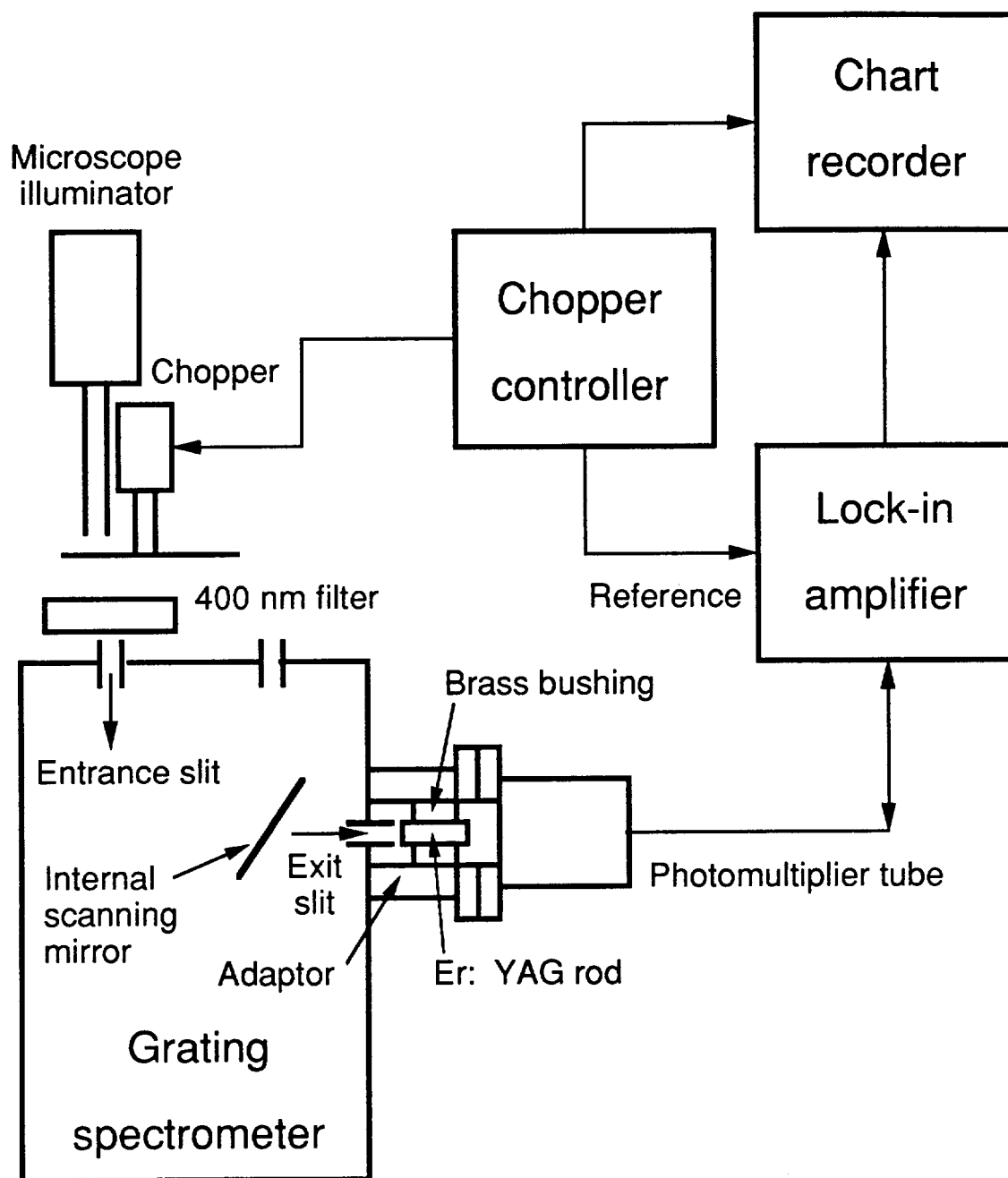
Figure 4.5.1: 783-819 nm absorption spectroscopy setup

spectrometer and the GaAs photomultiplier tube detector. The rod was held in place with a brass bushing. A microscope illuminator was used as a white-light source to illuminate the entrance slit of the spectrometer. The light was chopped and passed through a filter (optical density=10 at 488 nm) to prevent $\approx$400-nm light from coming through in second order. The internal scanning mirror deflection was adjusted to calibrate the spectrometer to the 632.8-nm HeNe line.

Figure 4.5.2 shows the absorption spectrum from 783 nm to 819 nm. The resolution is $\approx$.05 nm. The peaks are identified by the pair of levels defining the transition. Of greatest interest is the absorption peak at 788 nm.

The transmission at line center (T) was found by taking the ratio of the distance from the T=0 baseline (S) to the absorption peak to the distance between the T=0 and the T=1 baselines (B).

$$T = \frac{S}{B} \tag{4.5.1}$$

The T=0 baseline is found by closing the entrance slit, the T=1 baseline is found by drawing a line tangent to the portions of the curve where absorption due to Er^{3+} is neither expected nor apparent, e.g. 782 nm and 793 nm. The absorption coefficient normalized to the Er^{3+} concentration is

$$\sigma_p = \frac{1}{NL}\log\left(\frac{1}{T}\right) \tag{4.5.2}$$

Assuming that N and L are accurate and that noise has a normal distribution, the uncertainty is found by standard techniques to be

$$\sigma(\sigma_p) = \frac{1}{NL}\frac{\sigma(T)}{T} = \frac{2^{\frac{1}{2}}}{NL}\sigma(\text{noise})[S^{-2}+B^{-2}]^{\frac{1}{2}} \tag{4.5.3}$$
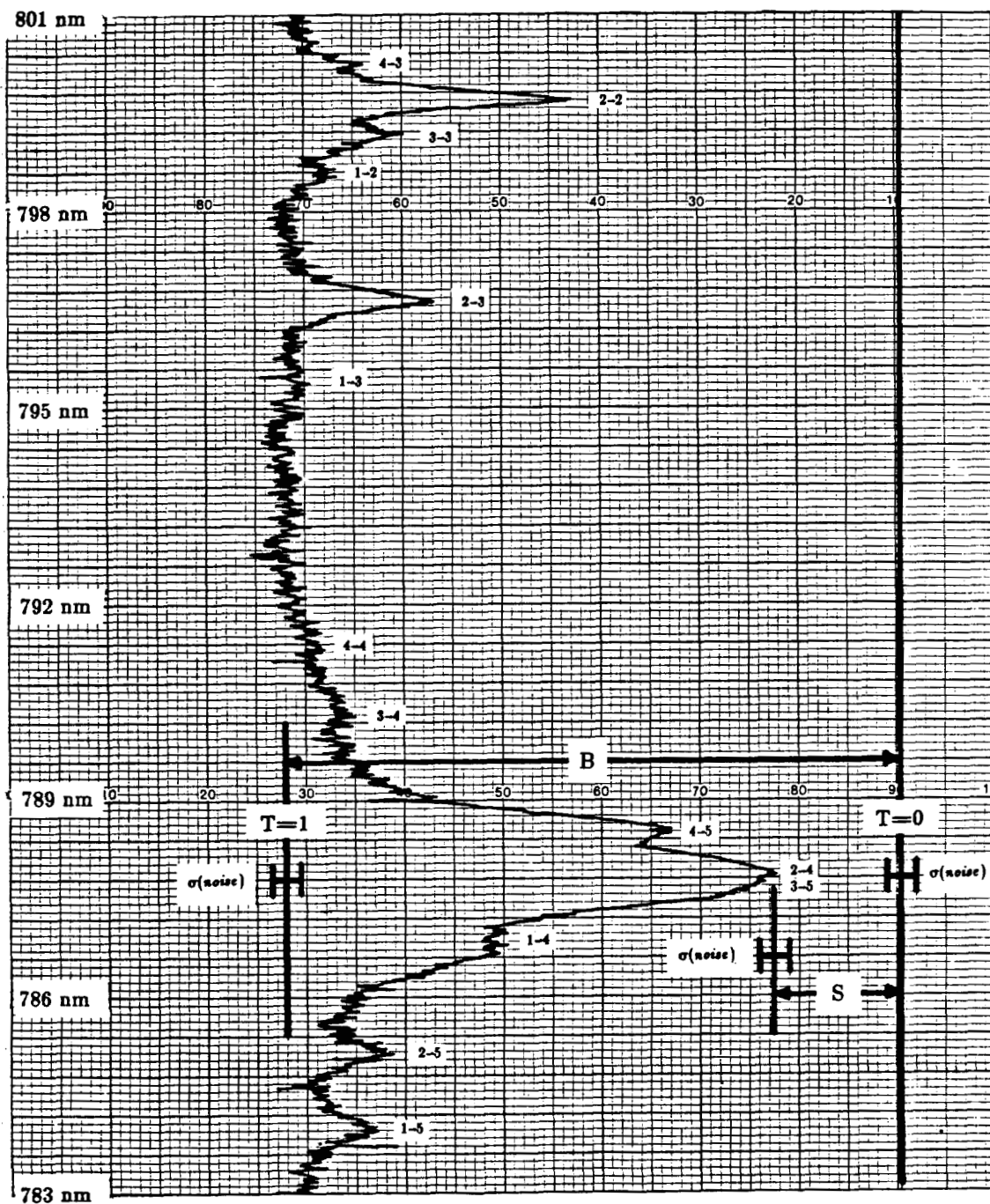
Figure 4.5.2   783-819 nm Absorption Band, Page 1 of 2
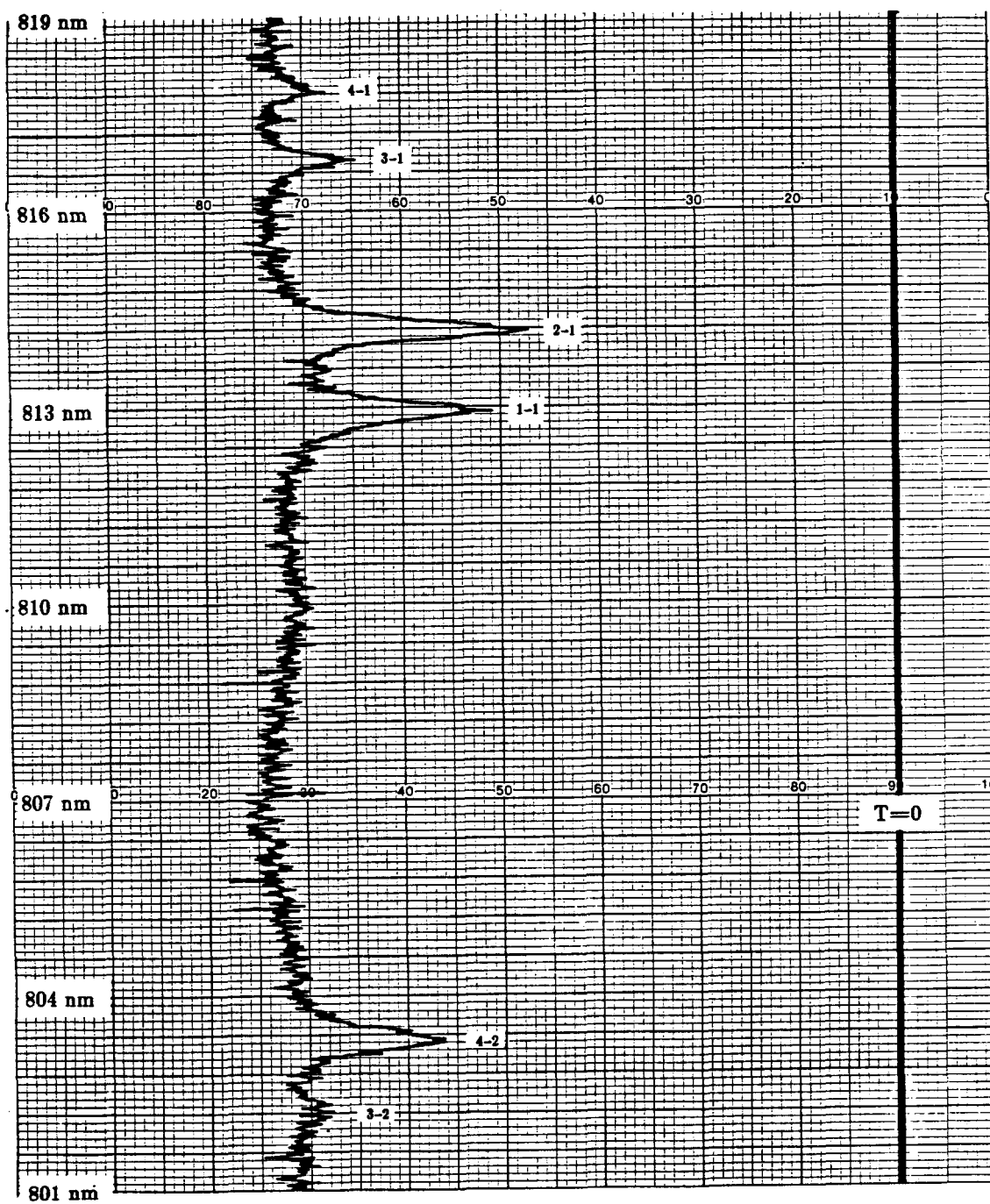
Figure 4.5.2   783-819 nm Absorption Band, Page 2 of 2

where the uncertainty in the signal and both baselines are each assumed to be equal to $\sigma(\text{noise})$, which is shown by the error bars in Figure 4.5.2. Equations 4.5.2 and 4.5.3 give $\sigma_p = 0.61 \pm .06$ cm^{-1} (atom %)$^{-1}$ in convenient units.

To obtain σ_p in the more conventional units of cm^2, this can be divided by 1.38×10^{20} cm^{-3} (atom %)$^{-1}$ for YAG. The FWHM of the 788-nm peak is 1.7 nm.

B. Measurement of the Stimulated-Emission Cross-Section

σ_0 was introduced in Equations 4.3.1-2 as the stimulated-emission cross-section of the Er:YAG $(1,3) \rightarrow (0,7)$ transition. The absorption cross-section is measured here, and equated to σ_0 because the degeneracies of $(1,3)$ and $(0,7)$ are equal $(g=2)$. The setup used for these measurements is shown in Figure 4.5.3. Because of the lower sensitivity of the InSb detector compared to the photomultiplyer tube used for the 783-819 nm measurements, a brighter light source and a wider entrance slit were required. In powering the 600 W bulb, a Variac setting of 36 VAC was found to be adequate. The filament was imaged onto the entrance slit after being passed through a silicon filter to prevent $\approx$800-nm light from being detected in second order. The light was chopped inside the spectrometer. Because a different spectrometer exit port was used, the internal scanning mirror had to be removed and a separate wavelength calibration run was necessary to correct the raw wavelength data.

Figure 4.5.4 shows the entire absorption band. Peaks are denoted as before. Absorption is much greater near the short-wavelength end because nearly all the ions are in the lower four levels of the ground manifold at room temperature thermal equilibrium. The transition of interest is centered at
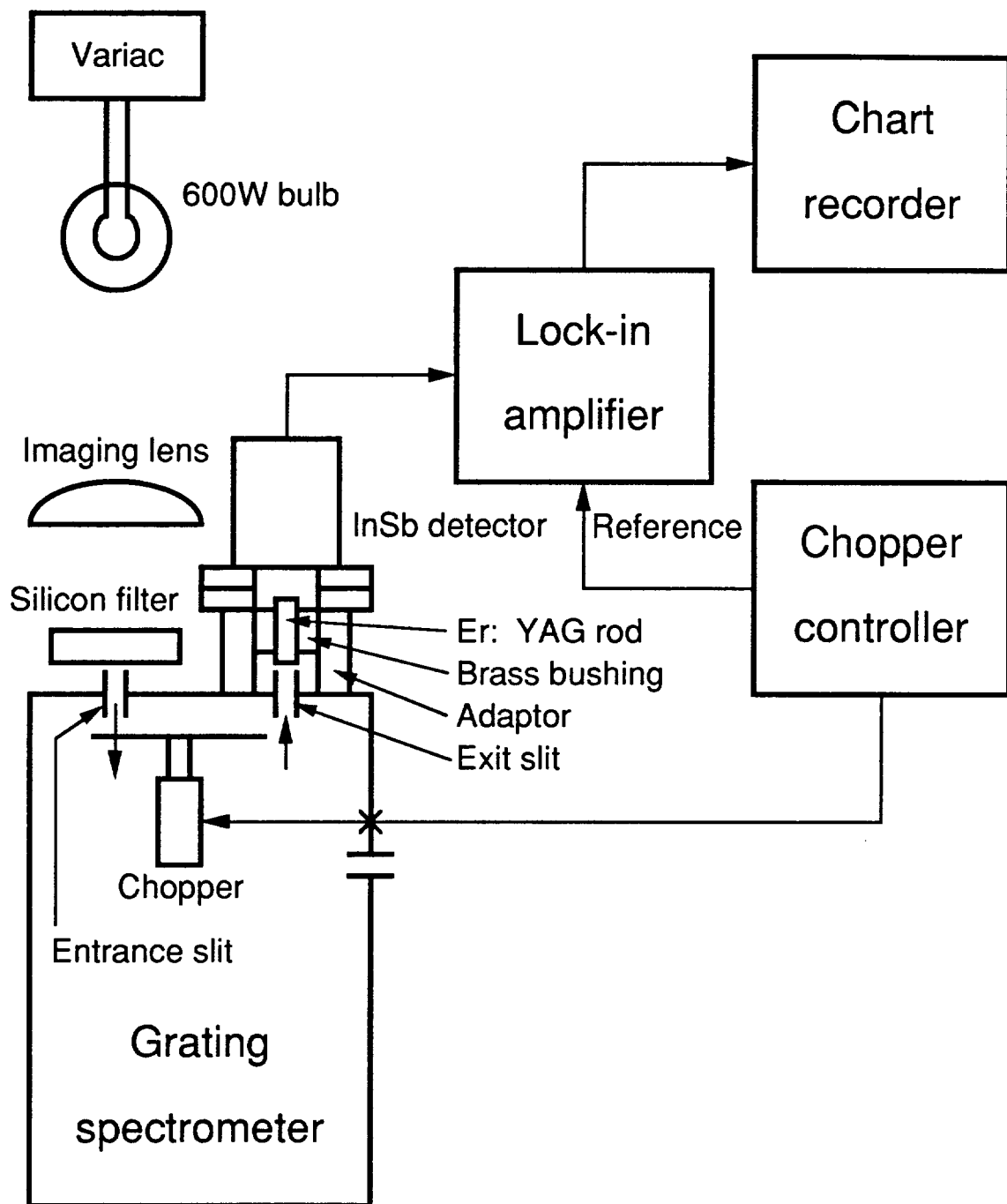
Figure 4.5.3: 1440-1680 nm absorption spectroscopy setup
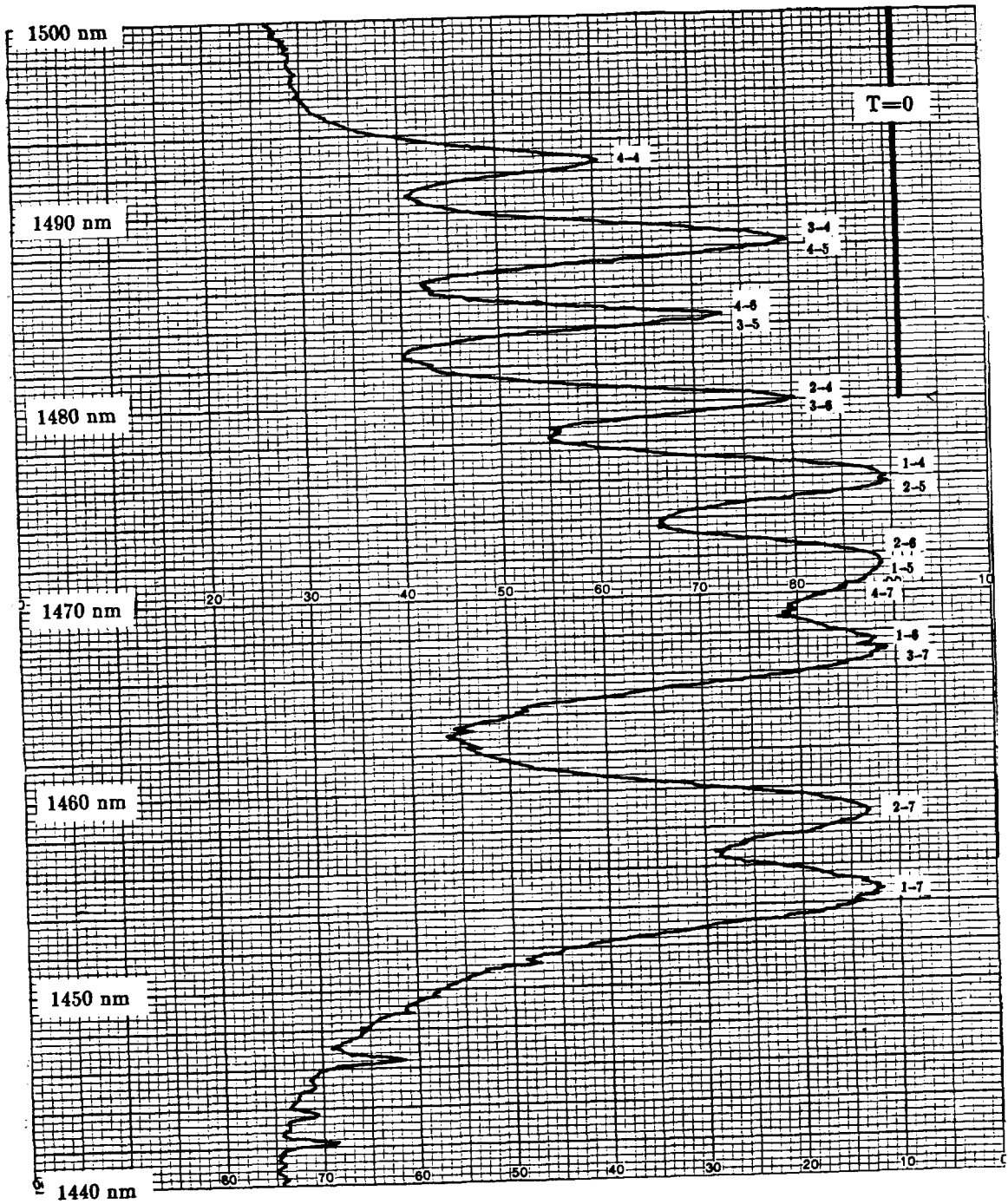
Figure 4.5.4   1440-1680 nm Absorption Band, Page 1 of 4
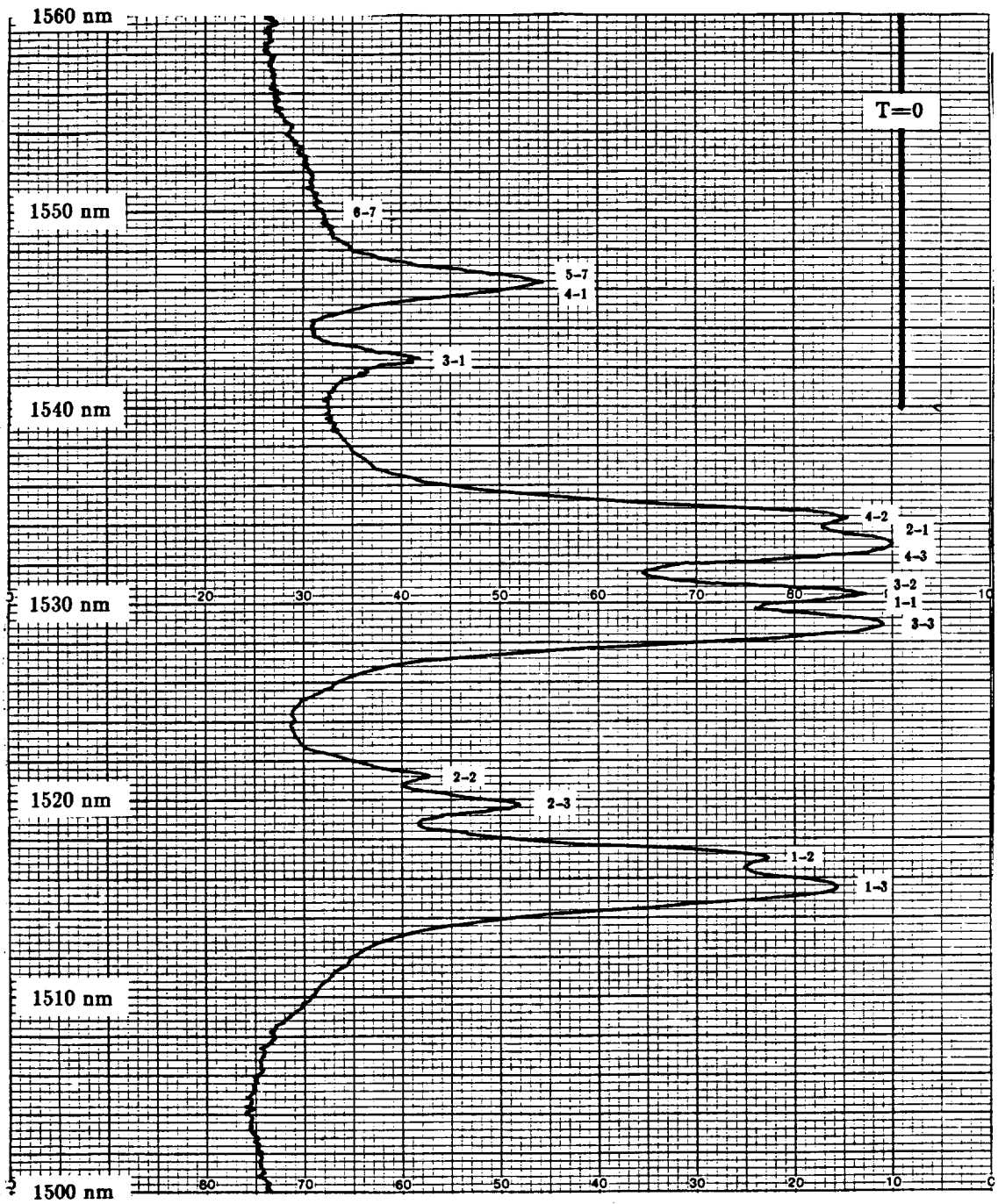
Figure 4.5.4   1440-1680 nm Absorption Band, Page 2 of 4
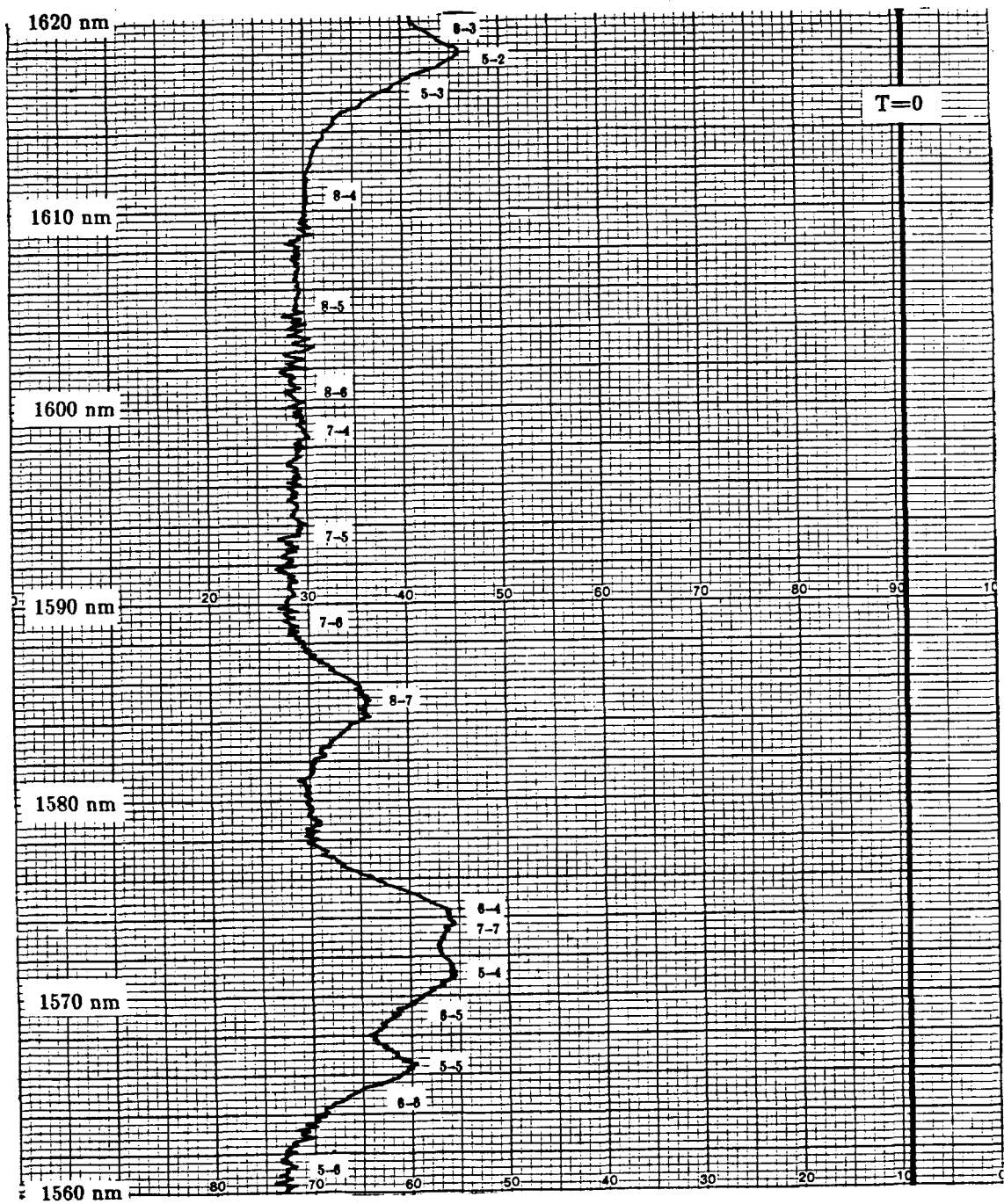
Figure 4.5.4   1440-1680 nm Absorption Band, Page 3 of 4
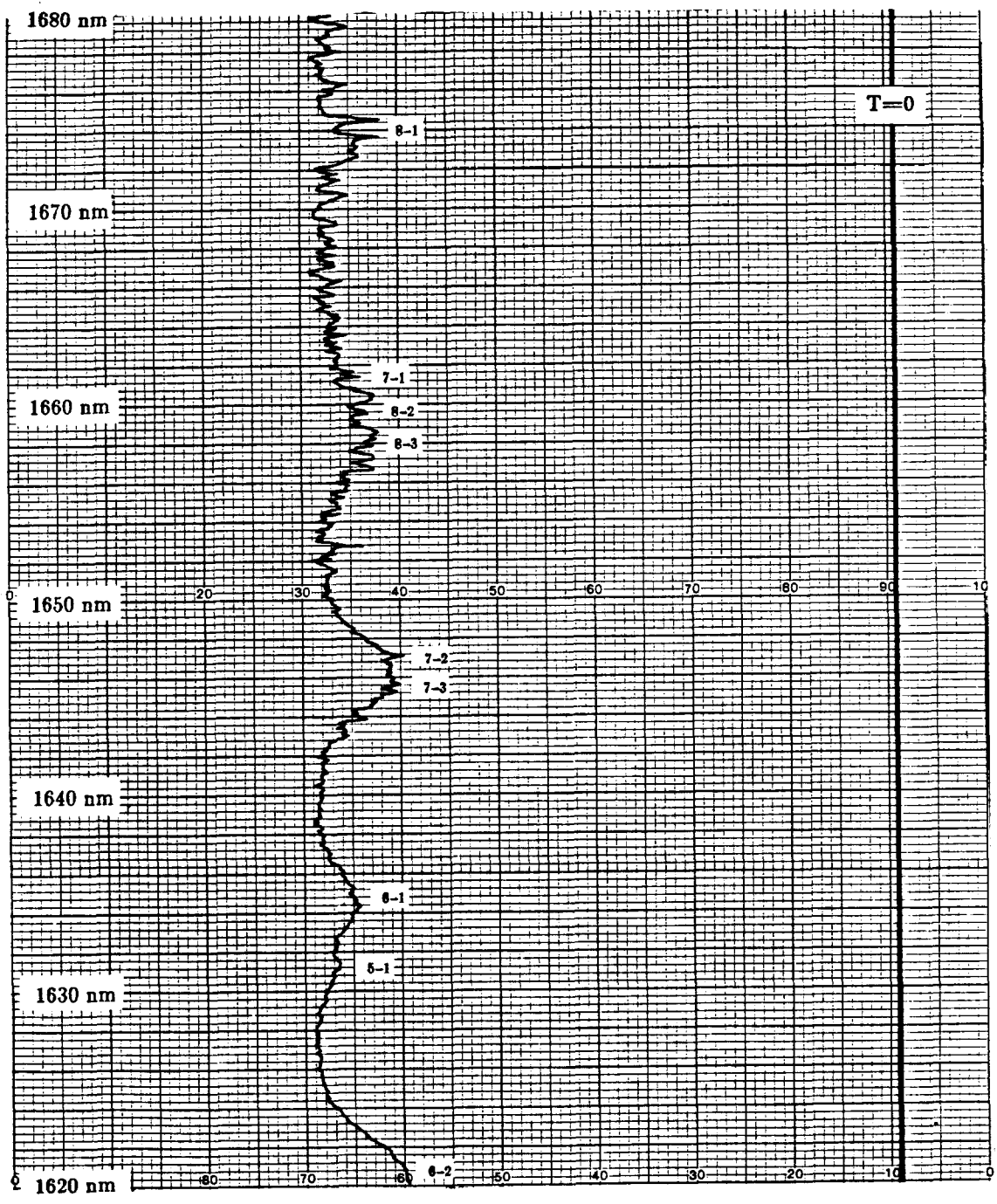
Figure 4.5.4   1440-1680 nm Absorption Band, Page 4 of 4

1644.7 nm with a FWHM of 4 nm.

Two higher-resolution scans of the peak were performed to calculate the line center cross-section. Using

$$\sigma_0 = \frac{1}{NLf_a} \log\left(\frac{1}{T}\right) \qquad (4.5.4)$$

with $f_a(T=20°C)=0.0204$, and an expression analogous to Equation 4.5.3 for the uncertainty gives $\sigma_0=2.0\pm.4\text{x}10^{-20}$ cm^2. Note that this is a true cross-section because Equation 4.5.4 incorporates f_a, in contrast to Equation 4.5.2.

C. Fitting W_1 to Zhekov's data

Zhekov et. al[35]. have noted a quadratic dependence of the co-operative upconversion coefficient W_1 on N.

$$W_1 = \Omega N^2 \qquad (4.5.5)$$

Fitting this to Zhekov's data gives $\Omega=5\text{x}10^{-60}$ cm^{9}s^{-1}, with an uncertainty of $\pm 50\%$ originating from the data. W_1 is the least well-known of the parameters used in the rate equations.

5. END-PUMPED ROD MODEL

5.1 Laser Geometry

The resonator considered in this chapter is of the plano-concave type introduced in Chapter 3. The rod is taken to extend from $z=0$ to $z=L$ in the axial direction and to infinity in the radial coordinate r, since the rod radius is much larger than the cavity mode. The pump beam and the cavity mode are assumed to be co-axial circular fundamental gaussians whose waists coincide at the resonator plano mirror at $z=0$.

Throughout this chapter, the following form is used for the normalized cavity mode intensity

$$s(r,z) = \frac{2}{\pi w_0^2(z)} \exp\left[\frac{-2r^2}{w_0^2(z)}\right] \tag{5.1.1}$$

where

$$w_0^2(z) \equiv w_0^2\left[1 + \frac{z^2}{b_0^2}\right] \tag{5.1.2}$$

$$b_0 \equiv \frac{\pi n_{r,0} w_0^2}{\lambda_0} \tag{5.1.3}$$

where $w_0(z)$ is the cavity mode spot size at z and $w_0 \equiv w_0(z=0)$ is the cavity mode waist size. The "0" subscript denotes quantities involving 1645-nm light and the "p" subscript is used with 788-nm (pump) light quantities in this work, to be consistent with the notation of Reference 27. The cavity

mode intensity is normalized so that

$$\int_0^\infty 2\pi r dr\ s(r,z) = 1 \qquad (5.1.4)$$

Note that the assumption of such a form forces the neglect of amplification of the stimulated wave as it propagates, since Equation 5.1.4 conserves power. This is permissible if the round-trip gain is small.

5.2 Cavity Mode Volume Pumped-to-Transparency Model

Because of the problems enumerated in Section 2.4, the absorbed power density needed to reach threshold is much larger with 1645-nm Er:YAG than 1064-nm Nd:YAG, and the pumped volume must be made small to keep the threshold within the range of existing diode laser pumps. To this end, assume that the pump beam and the cavity mode are well-matched, and define the "cavity mode volume" as the hyperbolic cylinder of revolution formed by rotating the cavity mode spot size $w_0(z)$ about the z axis. Then

$$V_0 = \pi \int_0^L dz\ w_0^2(z) = \pi L w_0^2 + \frac{\lambda_0^2 L^3}{3\pi n_{r,0}^2 w_0^2} \qquad (5.2.1)$$

This is minimized when

$$w_0^2 = w_{0,min}^2 \equiv \frac{1}{\sqrt{3}} \frac{\lambda_0 L}{\pi n_{r,0}} \qquad (5.2.2)$$

The minimum volume is

$$V_{0,min} \equiv \frac{2}{\sqrt{3}} \frac{\lambda_0 L^2}{\pi n_{r,0}} \qquad (5.2.3)$$

and the corresponding confocal parameter is given by

$$b_{0,min} \equiv \sqrt{1/3L} \qquad (5.2.4)$$

Assume that the cavity has been designed to support this diffraction-limited mode. A rough measure of the expected threshold is the incident pump power necessary to sustain transparency of the cavity mode volume. This is given by

$$P_{i,inv} = \frac{V_{0,min}\rho_{a,inv}}{1-\exp(-\alpha_{p,inv}L)} \qquad (5.2.5)$$

where $\rho_{a,inv}$ is the absorbed pump power density necessary to sustain transparency (inversion threshold), obtained from Equations 4.4.10 and 4.4.6, and $\alpha_{p,inv}$ is the pump absorption coefficient at transparency, given by

$$\alpha_{p,inv} = \sigma_p N n_{0,inv} \qquad (5.2.6)$$

where σ_p is the pump "cross-section" measured in Chapter 4.

Assume that $\alpha_{p,inv}L=1$ gives the optimal rod length, and that $n_{0,inv} \approx 1/(1+G)$. Inserting these and using Equation 4.4.3 and the material parameter values given in Chapter 4, the following is obtained

$$P_{i,inv} = \frac{2}{3^{\frac{1}{2}}\pi(1-e^{-1})n_{r,0}\eta_a} \frac{\lambda_0}{\lambda_p} \frac{hc}{\sigma_p^2\tau_1} G(1+G)^2 \left[\frac{1}{N} + \frac{G}{1+G}\tau_1\Omega N^2 \right]$$

$$= 71 \text{ mW} \cdot [(N \text{ in atom } \%)^{-1} + 0.0082(N \text{ in atom } \%)^2] \qquad (5.2.7)$$

This is minimized for N=3.9 atom % (L=.46 cm), with $P_{i,inv}(min)$=37 mW. An optimum value for N can be understood using the following argument: for N<N_{opt}, the rod must be longer for sufficient pump

absorption, and $V_{0,min}$ is larger than necessary, driving threshold up. When $N > N_{opt}$, upconversion depopulation of the upper lasing state becomes important and threshold increases.

There are several reasons to expect estimates made using Equation 5.2.7 to be low. First, the assumption of perfect mode-matching and confinement within $r \leq w_0(z)$ is unrealistic, the pump beam and the cavity mode cannot be perfectly matched and both spread beyond the cavity mode volume boundary. Mode-matching is discussed in Section 5.3. Second, cavity losses have been neglected. These are taken into account in the model developed in Section 5.4. Finally, some of the pump beam will be lost to the optical system that images the diode laser pump beam on the rod. Diode-laser pumps and coupling optics are discussed in Appendix B. Therefore, considering the results of Equation 5.2.7 to be low but not by more than an order of magnitude, it seems that a diode laser pumped 1645-nm Er:YAG laser is feasible, but will require careful design.

5.3   Cavity Mode and Pump Beam Overlap

The goal of this section is to develop an expression for the mode overlap and to optimize the trade-off between mode-matching and pumped-volume minimization.

Let the normalized pump beam intensity be

$$p(r,z) = \frac{2}{\pi w_p^2(z)} \exp\left[\frac{-2r^2}{w_p^2(z)} \right] \tag{5.3.1}$$

with definitions and normalization analogous to Equations 5.1.1-3. Note that

this ignores attenuation due to absorption as the beam propagates along the z axis, which is somewhat of an oversimplification.

An overlap factor can be defined as

$$\zeta \equiv \frac{\int dV \, ps}{[\int dV \, p^2]^{\frac{1}{2}} [\int dV \, s^2]^{\frac{1}{2}}} \qquad (5.3.2)$$

Substituting the assumed forms and integrating gives

$$\zeta = 2 \left[\frac{\kappa}{(1+\gamma)(1+\kappa^2/\gamma)} \right]^{\frac{1}{2}} \frac{\tan^{-1}\left[\left(\frac{1+\kappa^2/\gamma}{1+\gamma} \right)^{\frac{1}{2}} \frac{L}{b_p} \right]}{\left[\tan^{-1}\left(\frac{L}{b_p} \right) \right]^{\frac{1}{2}} \left[\tan^{-1}\left(\frac{\kappa}{\gamma} \frac{L}{b_p} \right) \right]^{\frac{1}{2}}} \qquad (5.3.3)$$

where

$$\kappa \equiv \frac{n_{r,p}}{n_{r,0}} \frac{\lambda_0}{\lambda_p} = 2.1 \text{ for } 1645-\text{nm Er:YAG} \qquad (5.3.4)$$

and

$$\gamma \equiv \frac{w_0^2}{w_p^2} \qquad (5.3.5)$$

$\zeta(\gamma)$ for various values of b_p/L is plotted in Figure 5.3.1. Several regimes exist:

1. For $b_p/L > 10$ (diffractionless regime) mode-matching is nearly perfect for $w_p = w_0$. Unfortunately, large pumped volumes make diode pumping infeasible.

2. For $b_p/L < 0.1$ (rapidly diffracting regime), mode overlap is maximum near $\gamma = \kappa$ and is $\zeta_{max} = 2\kappa^{\frac{1}{2}}/(1+\kappa) = .93$. Pumped volumes are too large in this
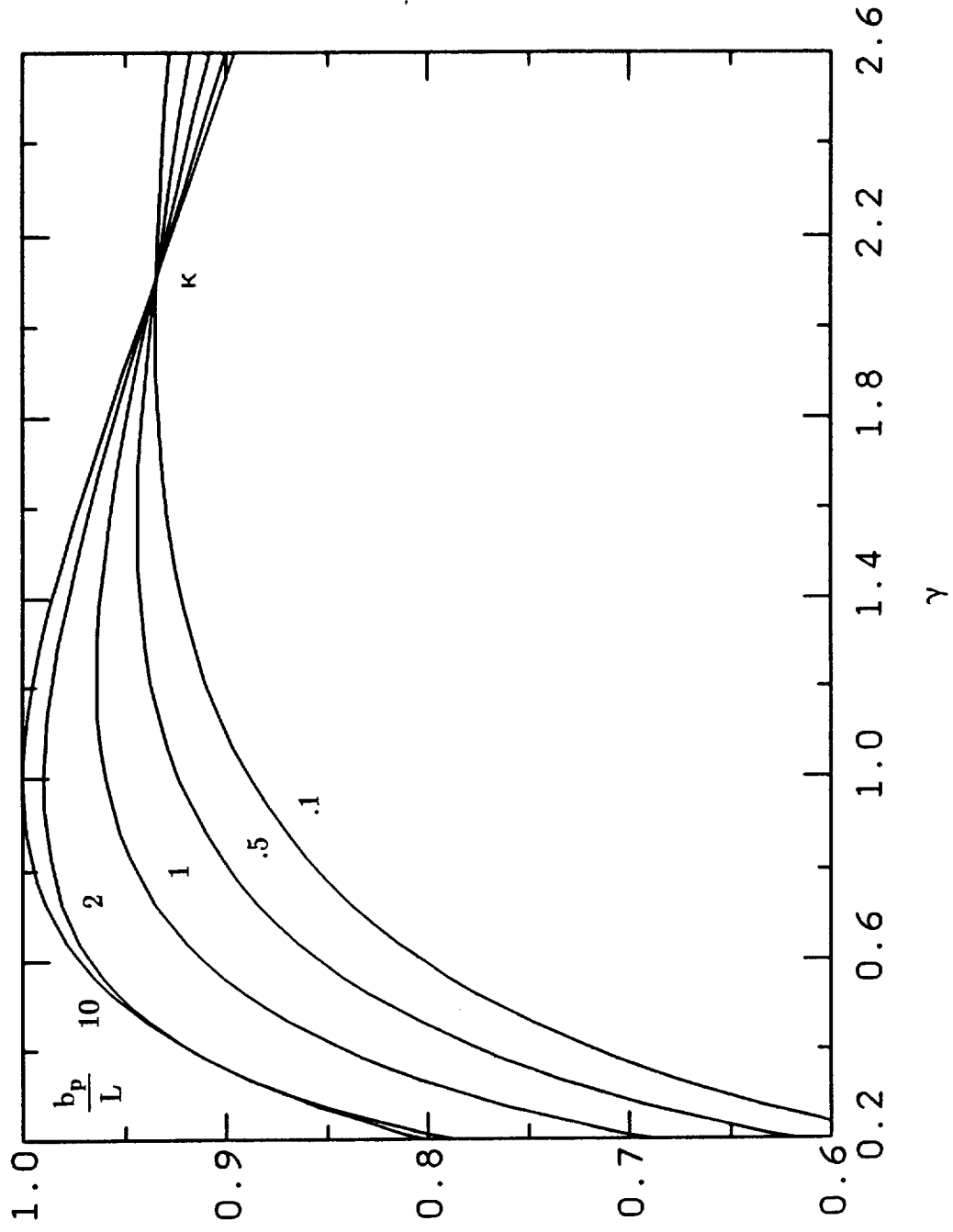
Figure 5.3.1   Overlap of the Pump Beam and the Cavity Mode

regime as well.

3. For $b_p = \sqrt{1/3}L$ (diffraction-limited minimum volume regime), mode matching is adequate ($\zeta_{max} = .95$ for $\gamma = 1.49$) and pumped volume is minimized. Any workable design is expected to fall within this regime.

The modeling presented so far has ignored cavity losses and therefore cannot accurately predict the relationship between pump power in (P_i) and stimulated power out (P_o). A quantitative model that takes cavity losses, pump beam attenuation, and saturation of the gain due to stimulated emission is formulated in the following section.

5.4   Quantitative Diode-Pumped 1645-nm Er:YAG Laser Model

The model described in this chapter is similar to approaches found in the literature[27,38]. Forms are assumed for the cavity mode intensity and pump beam absorption density. The former contains the output stimulated power P_o and the latter contains the input pump power P_i. Both forms are inserted into Equations 4.4.16-18 to obtain an approximation to the population inversion density $\Delta(r,z)$.

Δ is converted to the local gain per unit length by multiplying by $Nf_b\sigma_0$, where σ_0 is the cross-section for stimulated emission. The local gain per unit length is weighted by $s(r,z)$ and integrated over the z=constant plane to get the average gain per unit length as a function of z. This is integrated over z and multiplied by 2 to get the round-trip gain.

Steady-state is assumed, and the round-trip gain is equated to the round-trip loss δ. Both are assumed small so that distributed loss and z-

independent circulating stimulated power (P_c) assumptions are justified. Finally, $P_i(P_o)$ is solved for.

The cavity mode intensity is assumed to be

$$I_c(r,z) = P_c s(r,z) \qquad (5.4.1)$$

where P_c is the circulating stimulated power, which is related to the output stimulated power P_o by

$$P_c = \frac{P_o}{T} \qquad (5.4.2)$$

where T is the output coupler transmission.

The local pump beam absorption per unit length is

$$\alpha_p(r,z) = \sigma_p N n_0(r,z) \qquad (5.4.3)$$

In similar four-level models[27], ground manifold depletion is neglected so that $n_0(r,z)=1$ and α_p is independent of position. The pump beam absorbed-power density can then be written as

$$\rho_a(r,z) = P_i p(r,z) = P_i \frac{2\alpha_p}{\pi w_p^2(z)} \exp\left[\frac{-2r^2}{w_p^2(z)}\right] \exp(-\alpha_p z) \qquad (5.4.4)$$

In a three-level laser such as 1645-nm Er:YAG, there is necessarily ground manifold depletion, and there is a non-linear interdependence among the pump absorbed power density, stimulated intensities and the population inversion density. To avoid these difficulties, some error is risked by using Equation 5.4.4 with $\alpha_p=\alpha_{p,inv}$ given by Equation 5.2.6.

The round-trip gain/loss balance condition is

$$2\int_0^L dz \int_0^\infty 2\pi r dr \; s(r,z)Nf_b\sigma_0\Delta(r,z) = \delta = T+\delta_f+2\alpha_l L \qquad (5.4.5)$$

where δ_f is the residual extrinsic round-trip loss (loss at the rod facets, the output coupler and the etalon) and $2\alpha_l L$ is the length-dependent scattering round-trip loss intrinsic to the YAG host. The latter is negligible for good quality rods in the lengths of interest. Substituting Equations 5.1.1 and 4.4.16 into Equation 5.4.5 and solving for P_1 gives

$$P_1 = \frac{\pi}{2}\frac{1}{\eta_a}\frac{hc}{\lambda_p\tau_1}\frac{w_p^2}{\sigma_p}\left[\frac{\dfrac{\delta}{2\sigma_0 Nf_b}+X_{inv}\int_0^L dz\int_0^1 dv \; \chi(v,z)}{\int_0^L dz\left[\dfrac{\exp(-\alpha_p L)}{1+z^2/b_p^2}\right]^{\frac12}\int_0^1 dv \; v^{\frac12\gamma(z)}\chi(v,z)}\right]^2 \qquad (5.4.6)$$

where the change of variable

$$v(r,z) \equiv \exp\left[\frac{-2r^2}{w_0^2(z)}\right] \qquad (5.4.7)$$

has been made and

$$\gamma(z) \equiv \frac{w_0^2(z)}{w_p^2(z)} \qquad (5.4.8)$$

As noted in Section 4.4, the approximation Equation 4.4.16 becomes progressively worse as X grows large compared to X_{inv}. The largest value for X occurs at $r=0$, $z=0$; and is given by

$$X_{max} = X(r=0,z=0) = \left[\frac{2}{\pi}\eta_a\frac{\lambda_p\tau_1}{hc}\frac{\sigma_p}{w_p^2}P_1\right]^{\frac12} \qquad (5.4.9)$$

Substituting Equation 5.4.7 into Equation 5.4.9 gives

$$\frac{X_{max}}{X_{inv}} = \frac{\dfrac{\delta}{2\sigma_0 N f_b X_{inv}} + \int_0^L dz \int_0^1 dv\ \chi(v,z)}{\int_0^L dz \left[\dfrac{\exp(-\alpha_p L)}{1+z^2/b_p^2}\right]^{\frac{1}{2}} \int_0^1 dv\ v^{\frac{1}{2}\gamma(z)}\chi(v,z)} \qquad (5.4.10)$$

X_{max}/X_{inv} should remain ≤ 5 for accurate results.

5.5 Numerical Results

The results given in this section were obtained using the FORTRAN program "eryaglaser", which is listed and documented in Appendix A. The program reads a set of material parameters from the file "eryaglaser.prm" (given in Table 5.5.1) and the operating parameters δ_f and P_0 from the terminal.

Table 5.5.1 Er:YAG Material Parameters		
Parameter	Value	Reference
λ_p	788 nm	Section 4.5.A
λ_0	1645 nm	Section 4.5.B
$n_{r,p}$	1.824	42
$n_{r,0}$	1.809	42
η_a	1	assumed
σ_p	.61 cm^{-1}(atom%)$^{-1}$	Section 4.5.A
σ_0	2.0×10^{-20} cm^2	Section 4.5.B
τ_1	6.4 ms	Figure 4.2.2
τ_2	100 μs	Figure 4.2.3
Ω	5×10^{-60} cm^{9}s^{-1}	Section 4.5.C
α_i	0 cm^{-1}	assumed

The program calculates P_i as a function of N, temperature, L, w_p, w_0 and T. Exactly one of the independent variables is scanned over a user-specified range, the rest are either adjusted to minimize P_i (optimized) or fixed by the user. Any subset of L, w_p, w_0 and T can be simultaneously optimized, N and temperature must be scanned or fixed.

The program writes six output files of the form zzzz.suffix, where zzzz is a four-character string specified by the user. The files consist of ordered pairs, the first number of each pair being the scanned variable, the second number is P_i, X_{max}/X_{inv}, L, w_p, w_0 or T when suffix=pin, xmax, long, wp, w0 or trns, respectively.

A. Optimized 50 mW output room-temperature lasers

The goal of this section is to find the design that minimizes P_i for P_o=50 mW, the target output power. An operating temperature of 300 K, a round-trip extrinsic loss δ_f=.01 and a YAG scattering loss α_i=0 cm^{-1} are assumed throughout. The Er^{3+} concentration is scanned over the range N=1, 2.5, 4, 5.5, 7, 8.5 and 10 atom %. The variables L, w_p, w_0 and T were simultaneously optimized for each value of N.

Figure 5.5.1 shows that the optimum design occurs near N=4 atom %, as predicted in Section 5.2. The minimum is quite broad, so that errors in N during crystal growth should not be troublesome.

Figure 5.5.2 shows that X_{max}/X_{inv} approaches the limit of the validity of Equation 4.4.16, as can be seen in Figures 4.4.1-3. In the case N=1 atom %, Δ is underestimated over the range $0 \leq X \leq X_{max}$. This tends to overestimate P_i, but there is another effect: the spatial average of n_0 is smaller than $n_{0,inv}$,
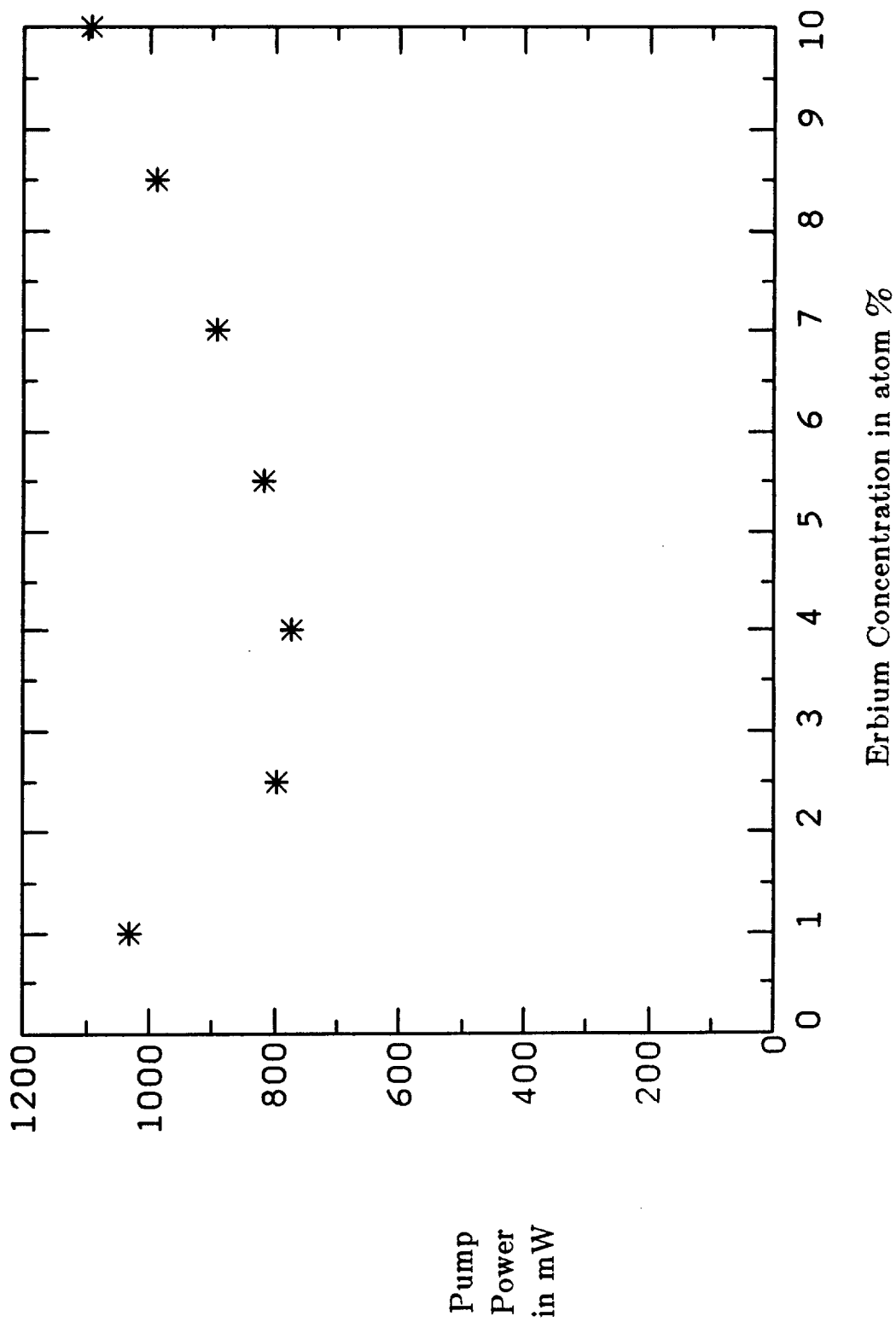
Figure 5.5.1   Fully Optimized Performances
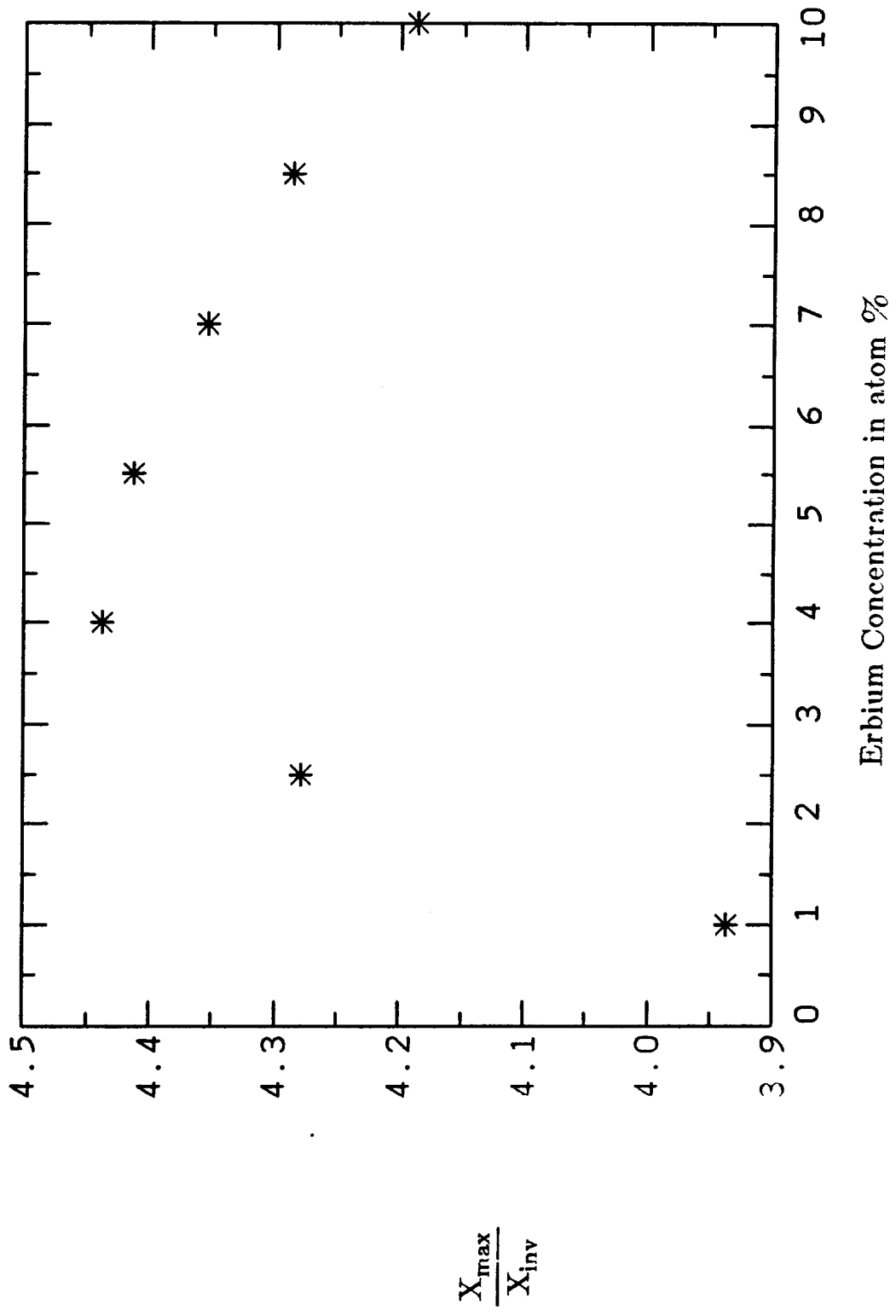
Figure 5.5.2   Fully Optimized Maximum Pump Intensities

hence $\alpha_p < \alpha_{p,inv}$ and P_1 must be made larger to compensate. Which effect dominates and to what extent is unknown. In the cases $N=4$ atom % and $N=10$ atom %, Δ is overestimated over the range $0 \leq X \leq X_{max}$, and both effects work together to underestimate P_1.

Figure 5.5.3 is a plot of $\alpha_{p,inv}L$, which is a measure of the extinction of the pump beam upon emergence from the rod at $z=L$. Note that $(\alpha_{p,inv}L)_{opt} \approx 1$ as assumed in Section 5.2. A maximum is noted near the optimum $N \approx 4$ atom %. The decrease on the $N<4$ atom % side can be understood as a trade-off between reducing mode volume (reducing L) and maintaining optimum pump beam extinction ($NL \approx$ constant). Apparently the former effect dominates for small N.

The reason for the decrease of $\alpha_{p,inv}L$ with increasing N on the $N>4$ atom % side is more obscure. For $N>4$ atom %, co-operative upconversion depopulation of the upper lasing level becomes important and the absorbed pump power density ρ_a needed to produce a given local gain rises rapidly with N. The pump beam intensity can be increased by reducing w_p, which causes $b_p \propto w_p^2$ to be drastically reduced. Apparently to avoid excessive pump beam diffraction and low gain at the far end of the rod, L must be reduced more rapidly than $1/\alpha_{p,inv} \propto 1/N$.

Figures 5.5.4-5 also show extrema near $N=4$ atom %. Note that the optimum design values $b_p/L \approx 2.3$ and $\gamma \approx .68$ are quite different than those predicted in Section 5.3. The maximum in Figure 5.5.4 can be explained as follows: As N decreases on the $N<4$ atom % side, L increases but w_p and thus b_p remains nearly constant, since an increase would needlessly increase
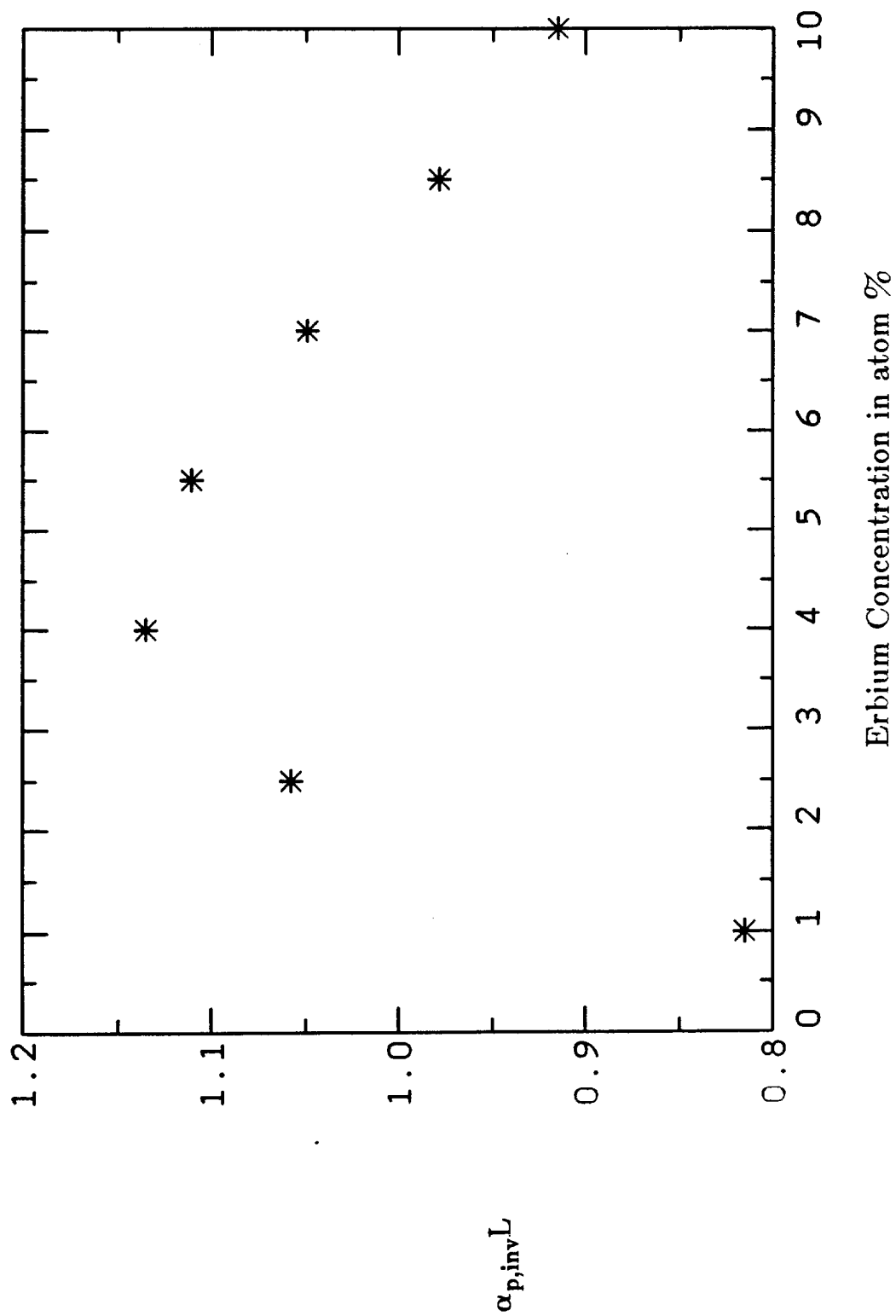
Figure 5.5.3   Fully Optimized Pump Extinction Products
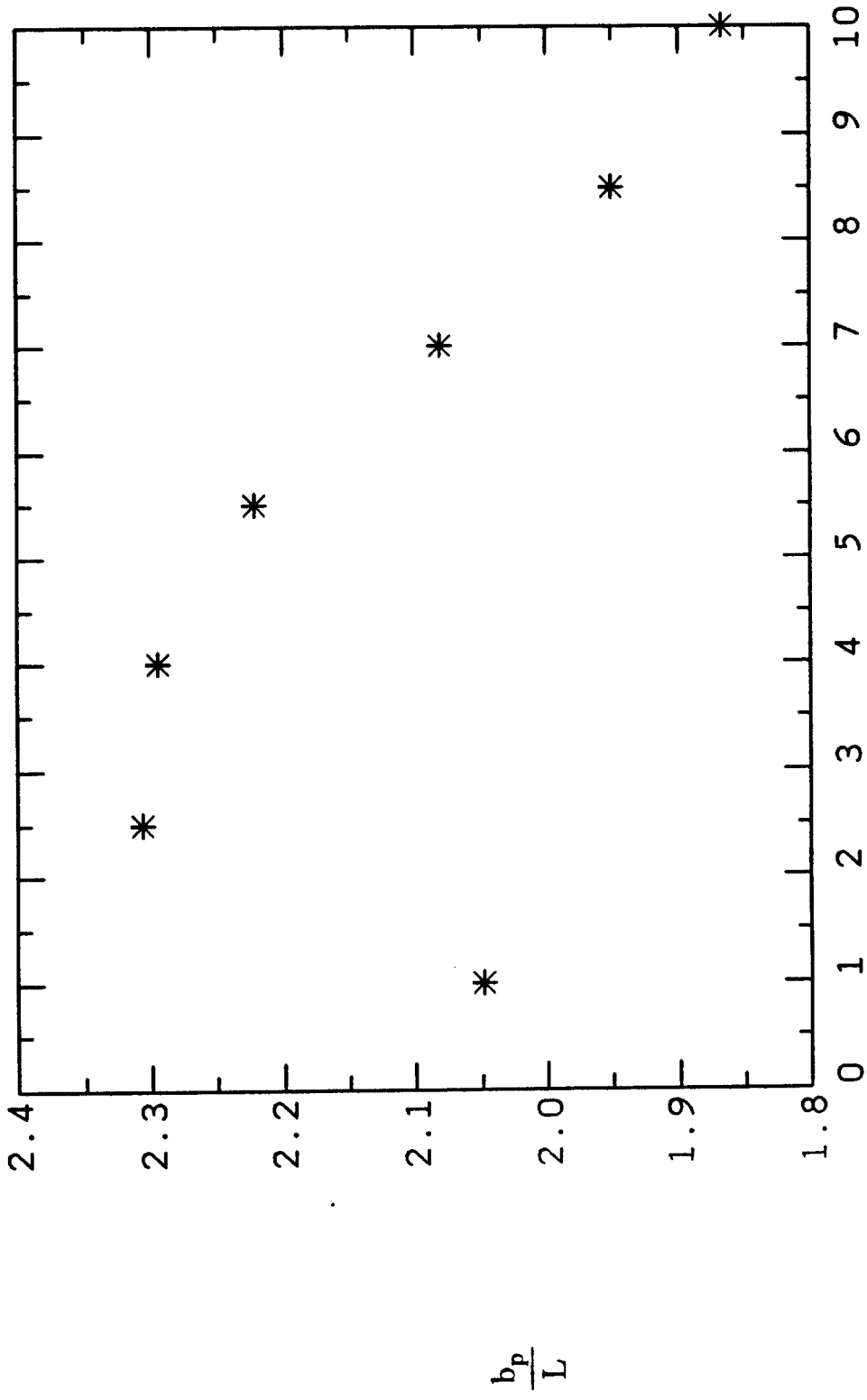
Figure 5.5.4   Fully Optimized Pump Confocal Parameters
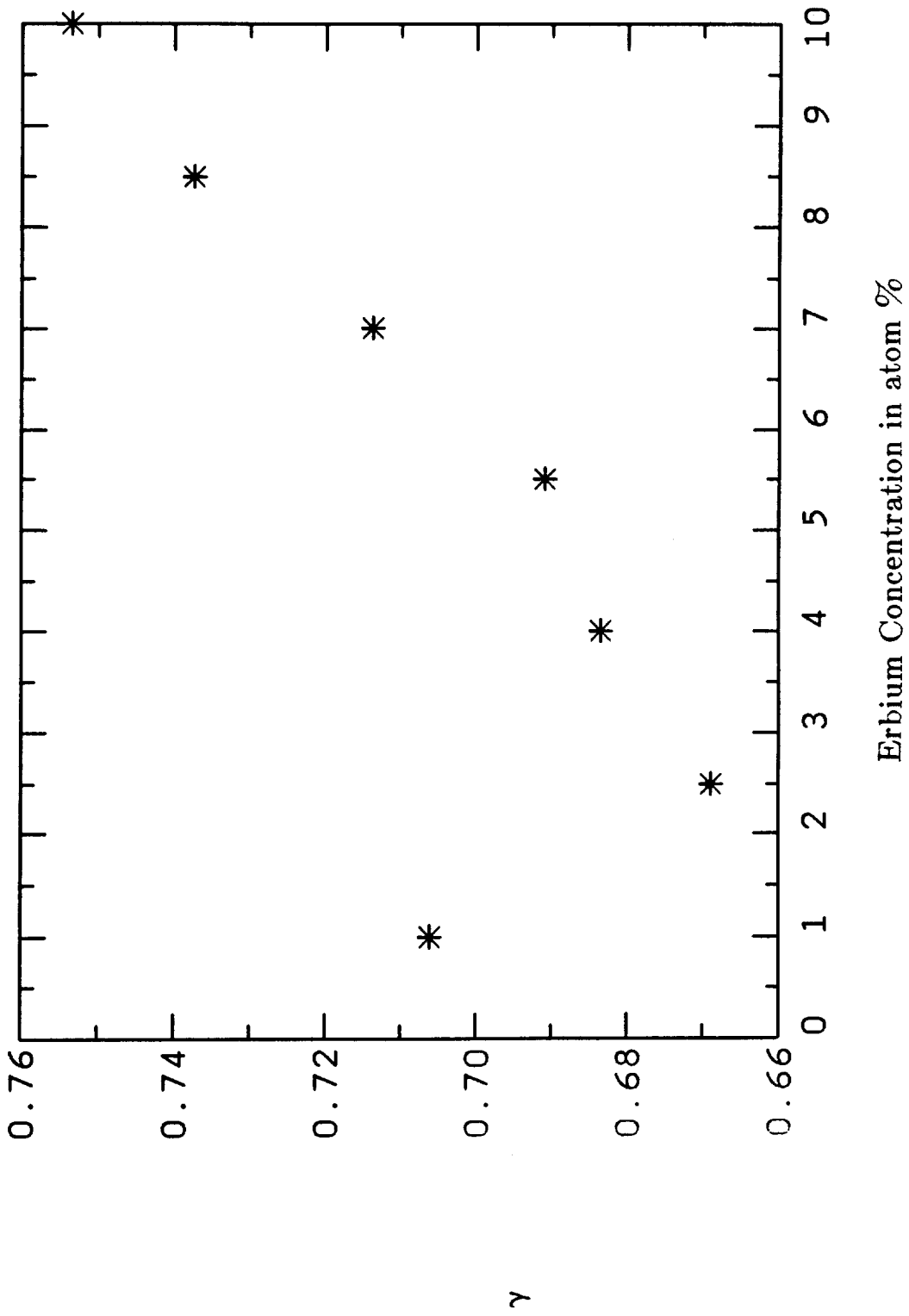
Figure 5.5.5   Fully Optimized Cavity Mode Waist Area

the mode volume. As N increases on the N>4 atom % side, b_p/L decreases because of the rapid decrease of w_p to compensate for co-operative upconversion depopulation, as discussed above.

Figure 5.5.6 shows that the minimum output coupler reflectivity R occurs near the optimum design. This indicates that the circulating stimulated power is smaller for the optimum design than for the extreme concentration designs.

B. N=4 atom % laser optimized for P_o=50 mW

The N=4 atom % laser that has been optimized to minimize P_i for P_o=50 mW has the following design parameters:

L = .51 cm

w_p = 40 μm

w_0 = 33 μm

R = .94

Figure 5.5.7 plots P_o as a function of P_i for this laser. The threshold is found to be 223 mW and the differential efficiency dP_o/dP_i=.092, which corresponds to a differential quantum efficiency of 19 %.

Figures 5.5.8-12 plot P_i as a function of one of the design parameters, with the others fixed. Figure 5.5.8 shows a moderate reduction in P_i with cooling in the range of a thermo-electric cooler. This is expected because the Boltzmann factor f_a of the lower lasing level 0,7 (523 cm^{-1} above 0,1) is a sensitive function of temperature near room-temperature ($\approx$200 cm^{-1}), while the Boltzmann factor f_b of the upper lasing level 1,3 (58 cm^{-1} above 1,1) is
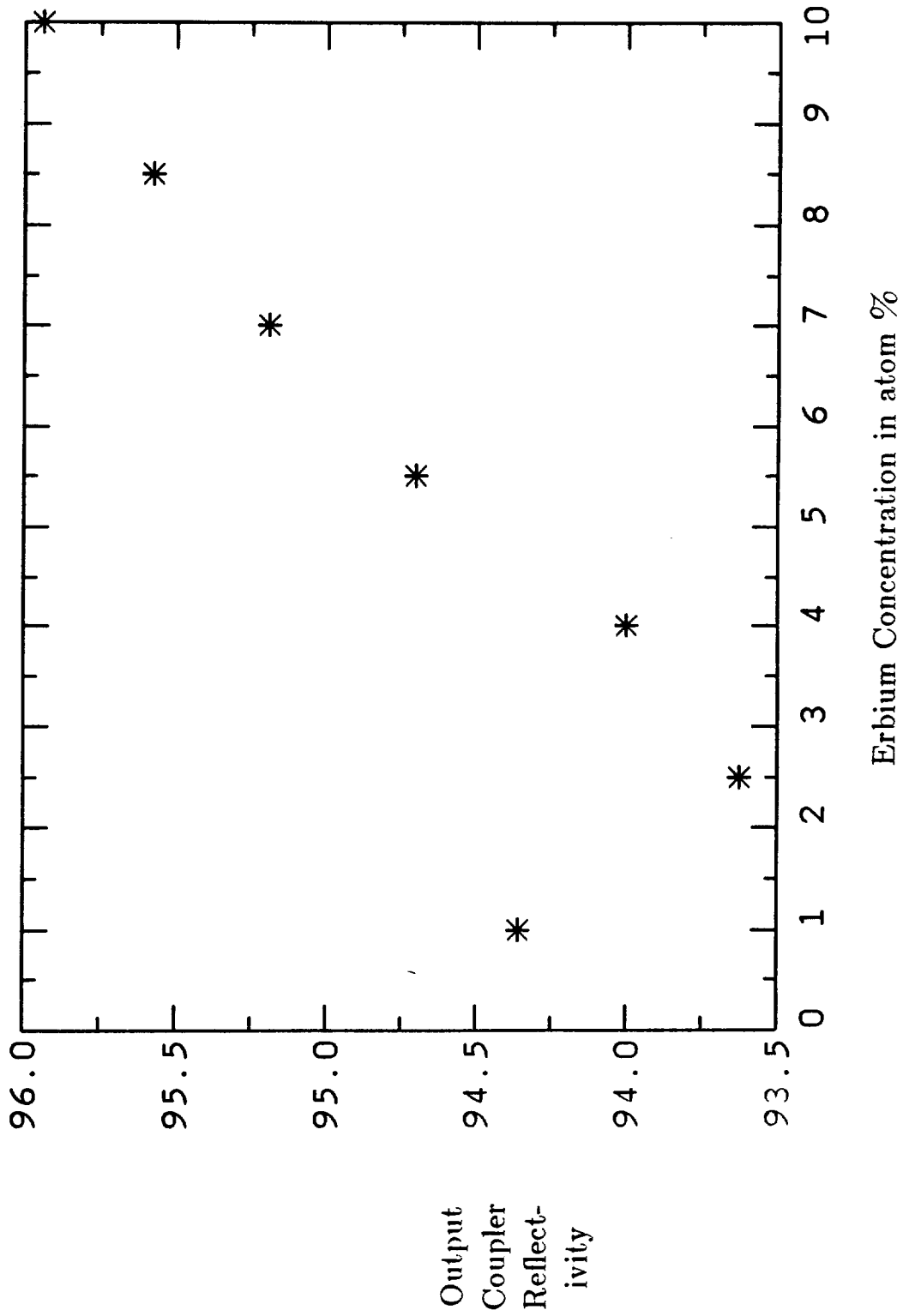
Figure 5.5.6   Fully Optimized Output Coupler Reflectivities
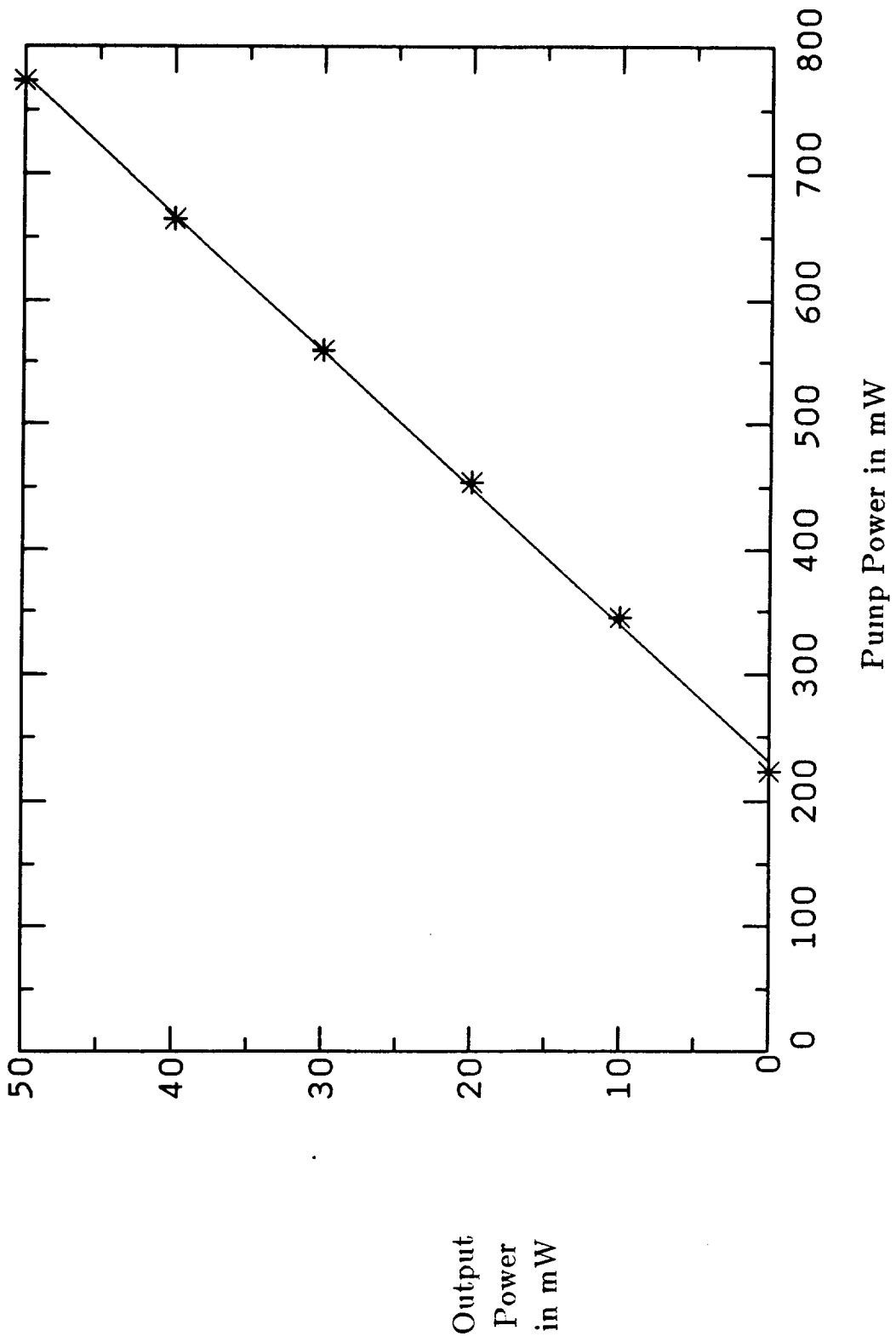
Figure 5.5.7   N=4 atom % Performance
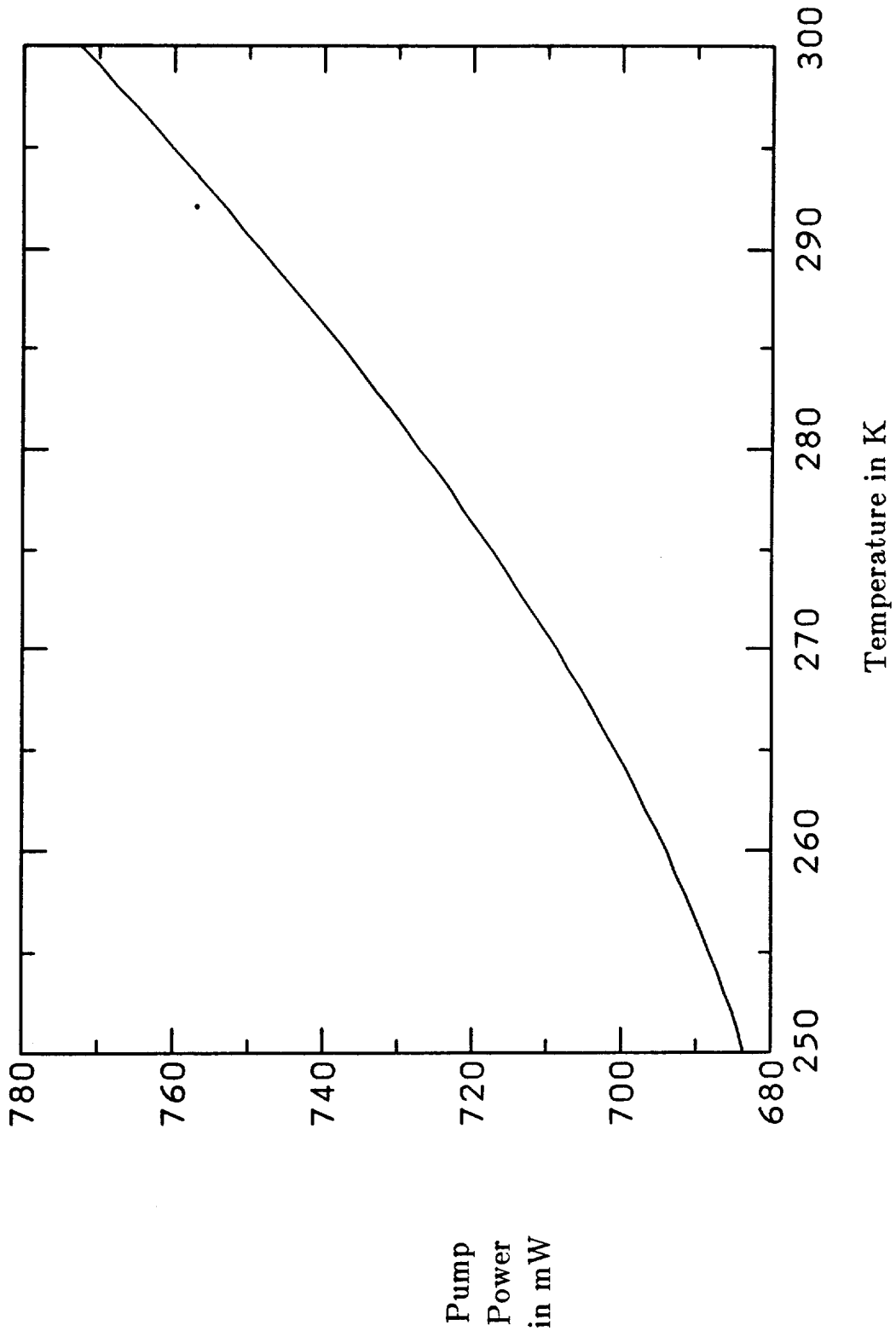
Figure 5.5.8   N=4 atom % Temperature Dependence
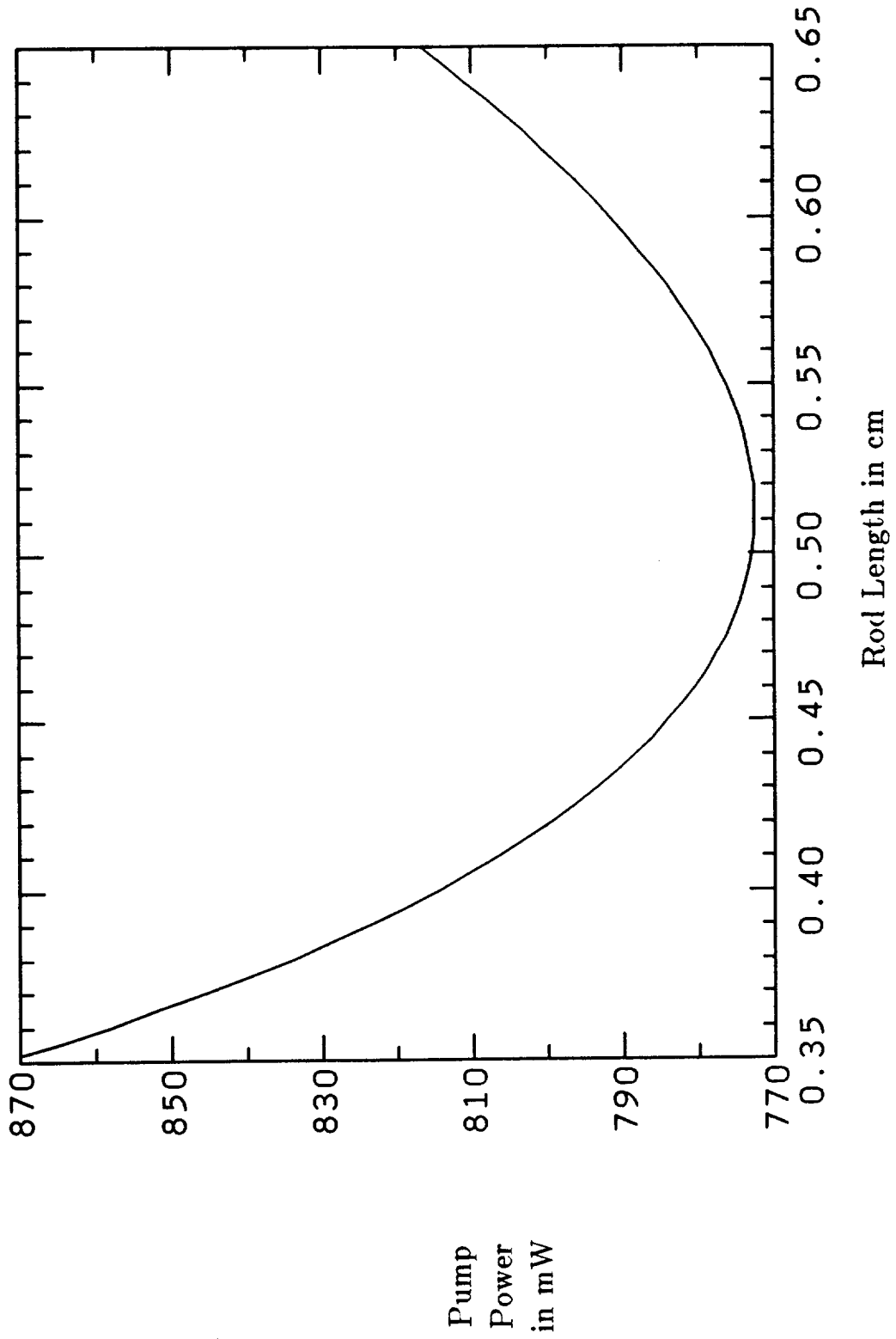
Figure 5.5.9   N=4 atom % Rod Length Dependence
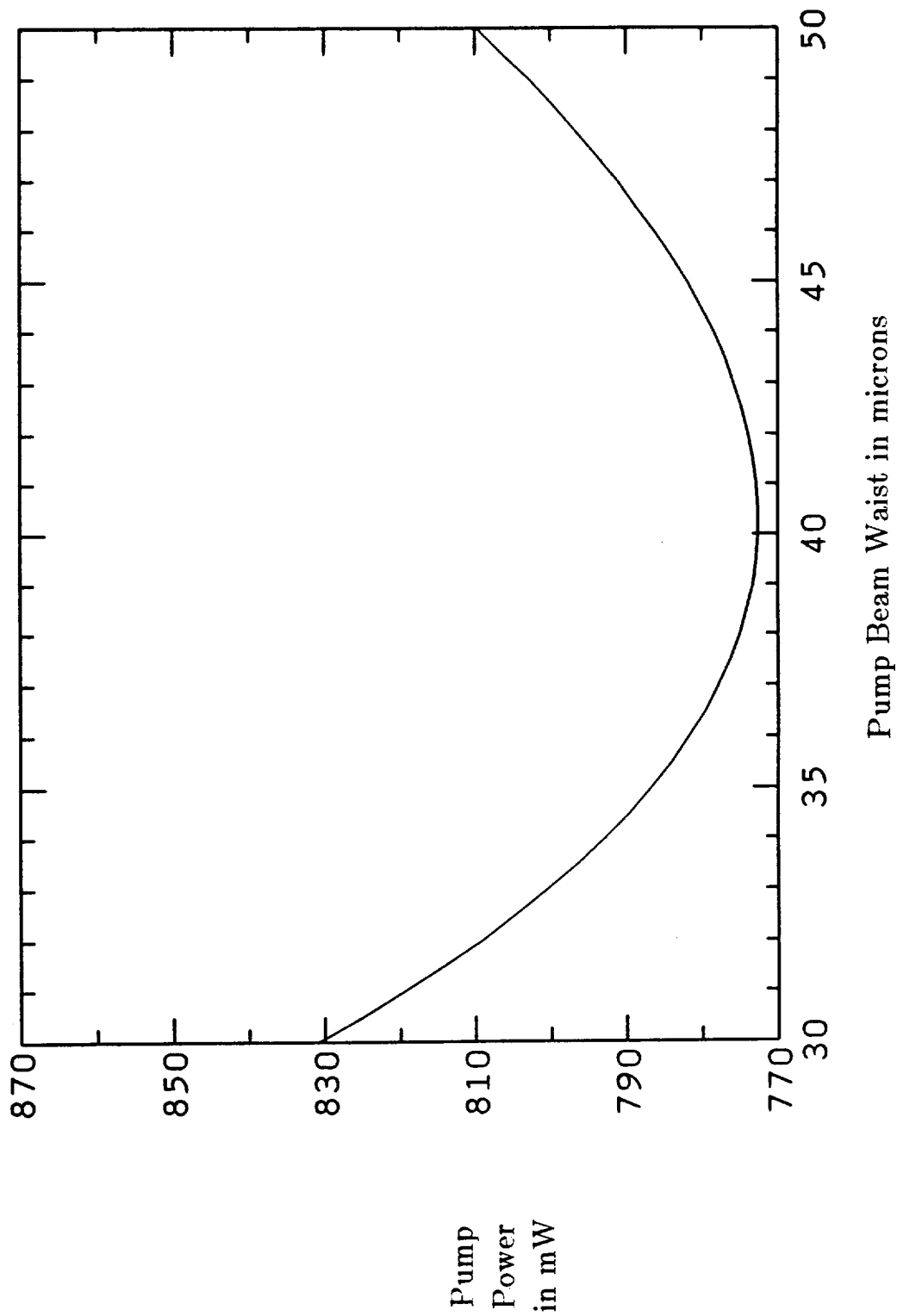
Figure 5.5.10   N=4 atom % Pump Beam Waist Size Dependence
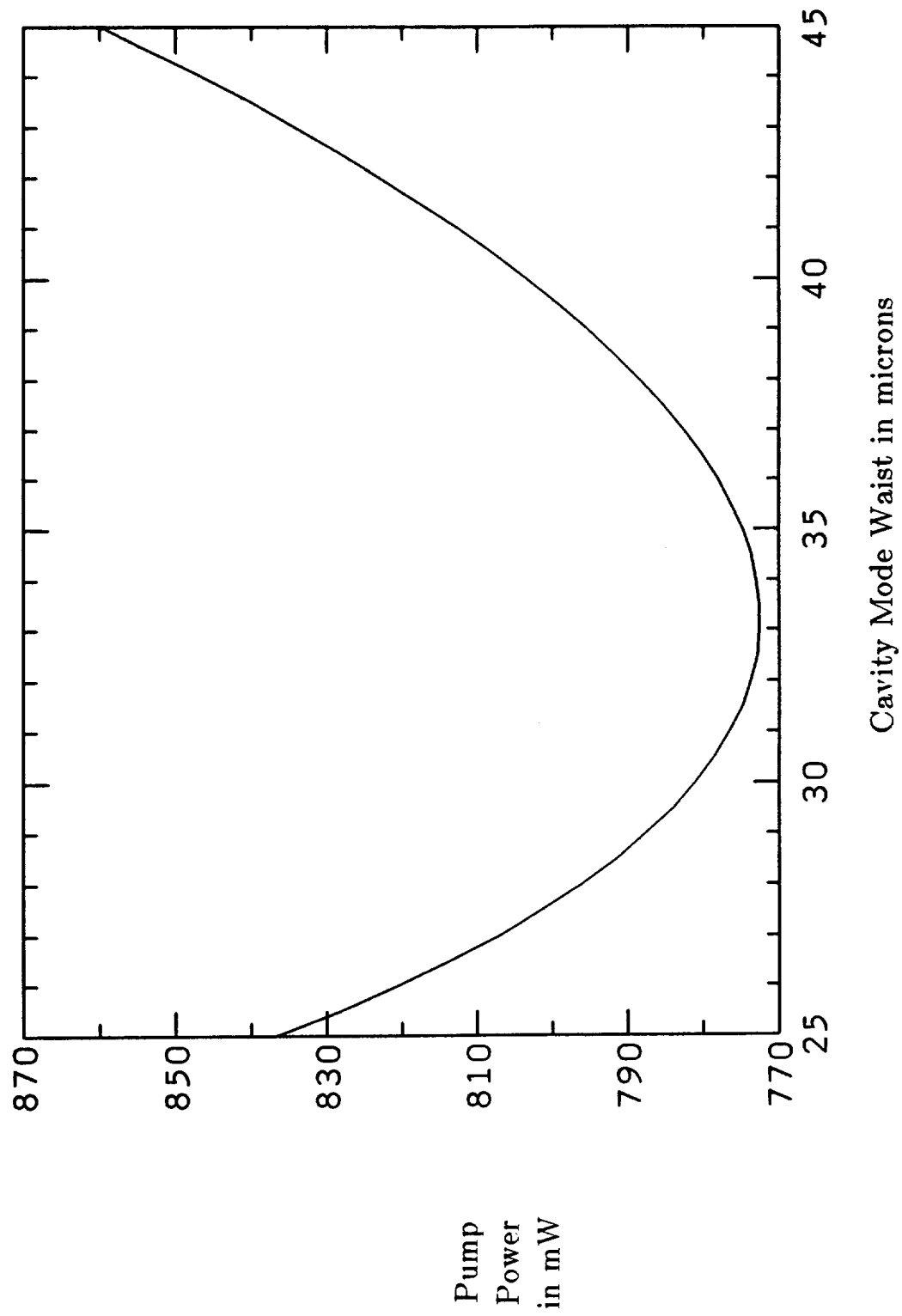
Figure 5.5.11   N=4 atom % Cavity Mode Waist Size Dependence
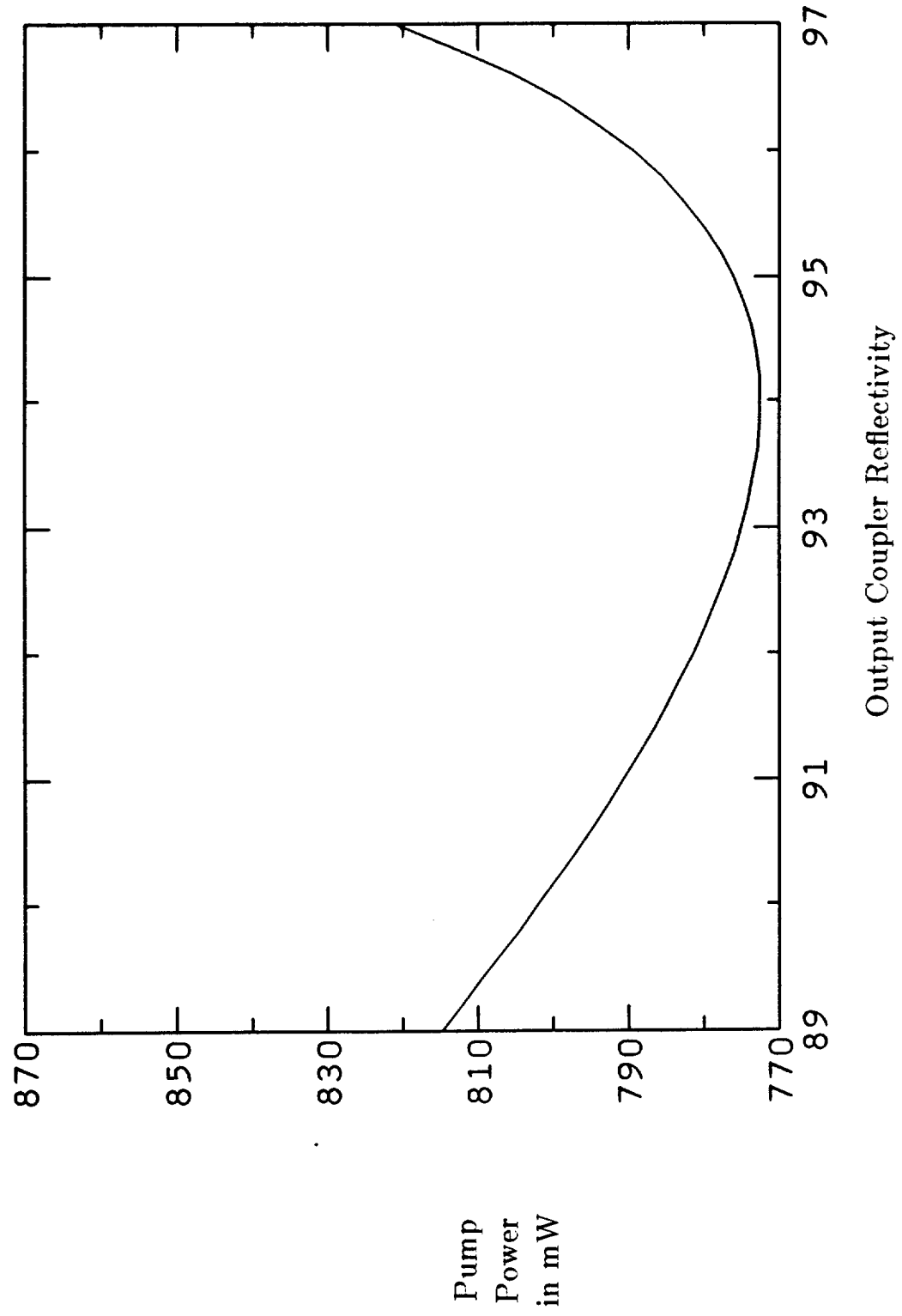
Figure 5.5.12 · N=4 atom % Output Coupler Reflectivity Dependence

not, and cooling tends to increase the inversion, favoring lasing. At much lower temperatures, the Boltzmann factor of the lower lasing level is virtually zero while that of the upper lasing level becomes sensitive to temperature, and further cooling decreases the inversion and hinders lasing.

Figures 5.5.8-12 show P_l as the different design parameters are each varied about the optimum design. Each shows a broad, symmetric minimum except for 5.5.12, which is rather steep on the high-reflectivity side. These broad minima indicate that design tolerances are forgiving.

5.6   End-Pumped Rod Model Applied to Nd:YAG

Diode laser end-pumped Nd:YAG lasers have been reported by many workers. In this section, the rate equations of Chapter 4 and the model developed in Section 5.4 are adapted for Nd:YAG and data reported by Berger et. al[29]. is used to test the adapted model.

Nd:YAG can be treated using the Er:YAG rate equations (Equations 4.3.1-5) if the Nd:YAG manifolds are numbered as shown in Figure 5.6.1. In this scheme, the $^4I_{9/2}$ and the $^4I_{11/2}$ manifolds are combined and designated "manifold 0". This is permissible because relaxation from $^4I_{11/2}$ to $^4I_{9/2}$ is very rapid ($\tau \approx 30$ ns)[31]. The lower lasing level is 0,8 and is at 2111 cm^{-1} relative to 0,1, and $f_a = 1.82 \times 10^{-5}$ at T=300 K.

The upper lasing level is 1,2; the upper level of the $^4F_{3/2}$ manifold. It lies 88 cm^{-1} above 1,1 and thus $f_b = .396$ and $G \equiv f_a/f_b = 4.59 \times 10^{-5}$.

The $^4F_{5/2}$ manifold plays the role of both manifold 3 and manifold 2, since it is pumped directly from manifold 0 and decays directly to manifold 1.
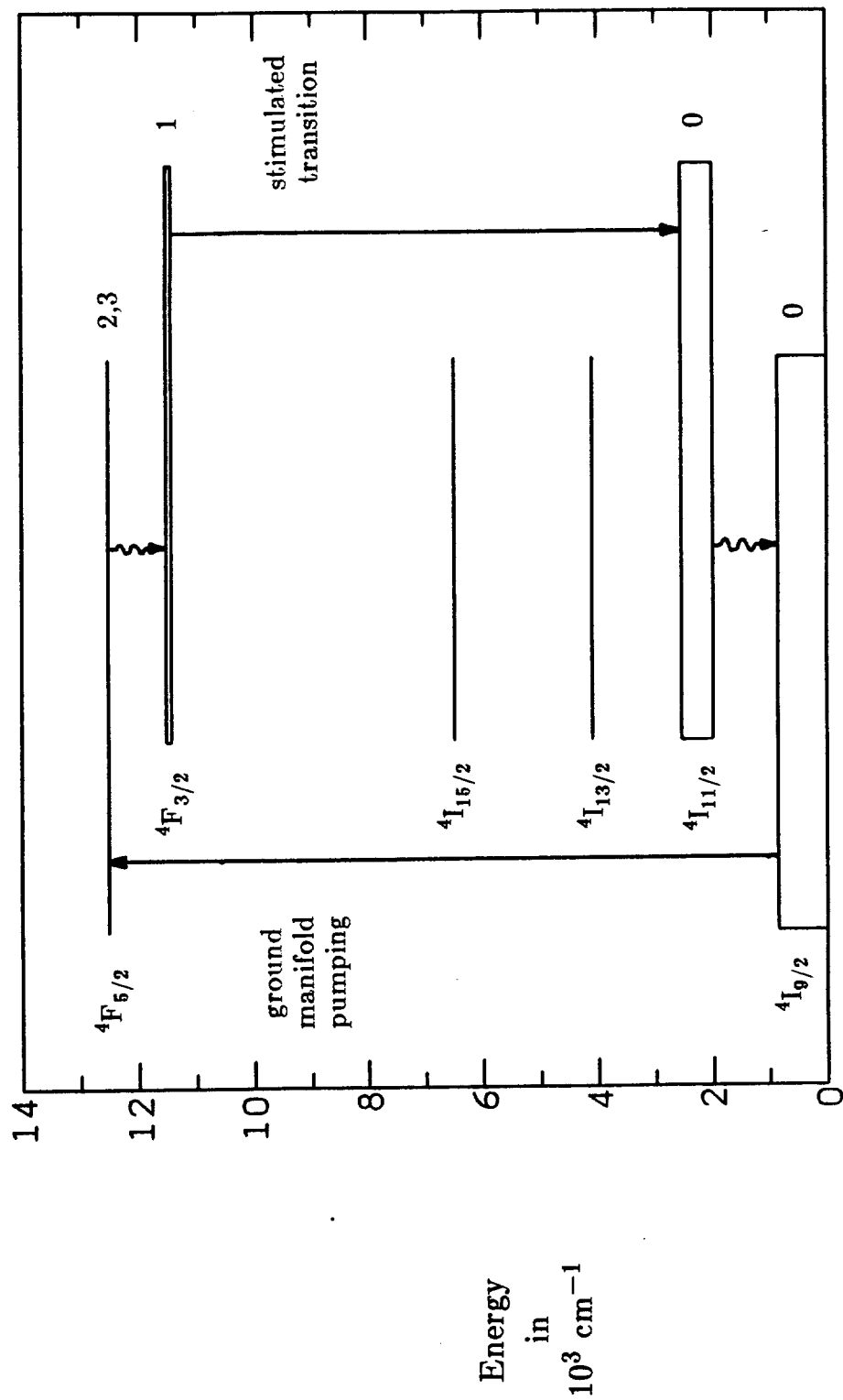
Figure 5.6.1   Nd:YAG Manifolds and Transitions

This is consistent with dropping Equations 4.3.3-4 and neglecting N_3 in Equation 4.3.5, as was done in deriving Equations 4.4.1-2.

Since $^4F_{5/2}$ lies less than 1000 cm^{-1} above $^4F_{3/2}$, relaxation is expected to be very rapid and $U \equiv \tau_2/\tau_1 \to 0$. Since there is no co-operative upconversion depopulation of the upper lasing level, $A \equiv \tau_1 N W_1 = 0$. Equation 4.4.15 simplifies to

$$\Delta = \frac{X^2 - G}{1 + (1+G)Y + X^2} \qquad (5.6.1)$$

Note that the approximation Equation 4.4.16 is no longer necessary or appropriate, since upconversion is absent. This approximation is not validated by the check presented in this section.

A plano-concave cavity like that described in Chapter 3 was used by Berger et. al[29]. but the pump beam, rather than being focused at the plano mirror, was focused near the center of the rod. Therefore, Y is still given by Equations 4.4.7, 5.4.1-2 and 5.1.1; but $w_p^2(z)$ must be replaced by

$$w_p^2(z) \equiv w_p^2 \left[1 + \frac{(z - \frac{1}{2}L)^2}{b_0^2} \right] \qquad (5.6.2)$$

in Equation 5.4.4 so that X^2 is given by Equations 4.4.6 and 5.4.4. Because ground manifold depletion is negligible,

$$\alpha_p = \sigma_p N \qquad (5.6.3)$$

Substituting these into Equation 5.4.5, the following is obtained for the gain-loss balance

$$\delta = 2\sigma_0 N f_b \int_0^L dz \int_0^1 dv \frac{C_1 v^\gamma \exp(-\alpha_p z) - G}{1 + (1+G)C_2 v + C_1 v^\gamma \exp(-\alpha_p z)} \qquad (5.6.4)$$

where

$$C_1 \equiv \frac{2}{\pi} \frac{\lambda_p}{hc} \tau_1 \eta_a \frac{\sigma_p}{w_p^2(z)} P_1 \qquad (5.6.5)$$

and

$$C_2 \equiv \frac{4}{\pi} \frac{\lambda_0}{hc} \tau_1 f_b \frac{\sigma_0}{w_0^2(z)} \frac{P_o}{T} \qquad (5.6.6)$$

Note that P_i and P_o are inseparable on the right-hand-side of Equation 5.6.4. The approach taken is to plot δ as a function of data pairs obtained from Figure 3 of Reference 29.

The FORTRAN program "berger", listed and documented in Appendix A, calculates $\delta(P_i, P_o)$ given the material and design parameters of the laser. These parameters are listed in Table 5.6.1.

The following method was used to obtain w_p: the angle that the asymptote of $w_p(z)$ makes with the z axis is given by

$$\tan(\phi) = \frac{w_p}{b_p} = \frac{\lambda_p}{\pi n_{r,p} w_p} \qquad (5.6.7)$$

This can be related to the HWHM divergence angle by

$$\tan(\theta) = \left[\frac{\ln(2)}{2} \right]^{\frac{1}{2}} \tan(\phi) \qquad (5.6.8)$$

which can in turn be related to $\alpha \approx 4°$ by

$$n_{r,p} \sin(\theta) = \sin(\tfrac{1}{2}\alpha) \qquad (5.6.9)$$

Table 5.6.1 Nd:YAG Laser of Berger et. al.		
Parameter	Value	Reference
λ_p	807 nm	
λ_0	1064 nm	
$n_{r,p}$	1.824	42
$n_{r,0}$	1.819	42
η_a	1	assumed
σ_p	$7.3 \ cm^{-1}(atom\%)^{-1}$	27 fig. 4
σ_0	$6.5 \times 10^{-19} \ cm^2$	31 p. 49
τ_1	230 μs	31 p. 49
N	1 atom %	assumed
temp	300 K	assumed
L	1 cm	29
w_p	4.3 μm	Section 5.6
w_0	130 μm	29
T	.05	29
coupling optics efficiency	80 %	assumed

Using the small-angle approximation,

$$w_p = \sqrt{2\ln(2)}\frac{\lambda_p}{\pi\alpha} \qquad (5.6.10)$$

Ideally, $\delta(P_i)$ should be constant if the adapted model and parameters listed in Table 5.6.1 are accurate (assuming the experimental data to be correct). Regardless of systematic error, $\delta(P_i)$ should approach an asymptotic limit with increasing $\dot{P}_i$. If this slope of the asymptote is positive (negative), the model/parameters underestimate (overestimate) the differential efficiency. If δ is anomalously large (small) near threshold, the model/parameters underestimate (overestimate) the threshold.

Figure 5.6.2 shows δ for four operating points scaled from Figure 3 of Reference 29. A coupling optics efficiency of 80 % is assumed in obtaining P_i from the reported diode laser output. Although it is fairly constant, $\delta_f = \delta - T \approx .04$ seems rather large, but considering all the assumed parameter values does not appear an unreasonable result.

The Er:YAG model still suffers the approximations of Equation 4.4.16 and $\alpha_p = \alpha_{p,inv}$, as well as the large uncertainty in Zhekov's upconversion data, and may be considerably less accurate.
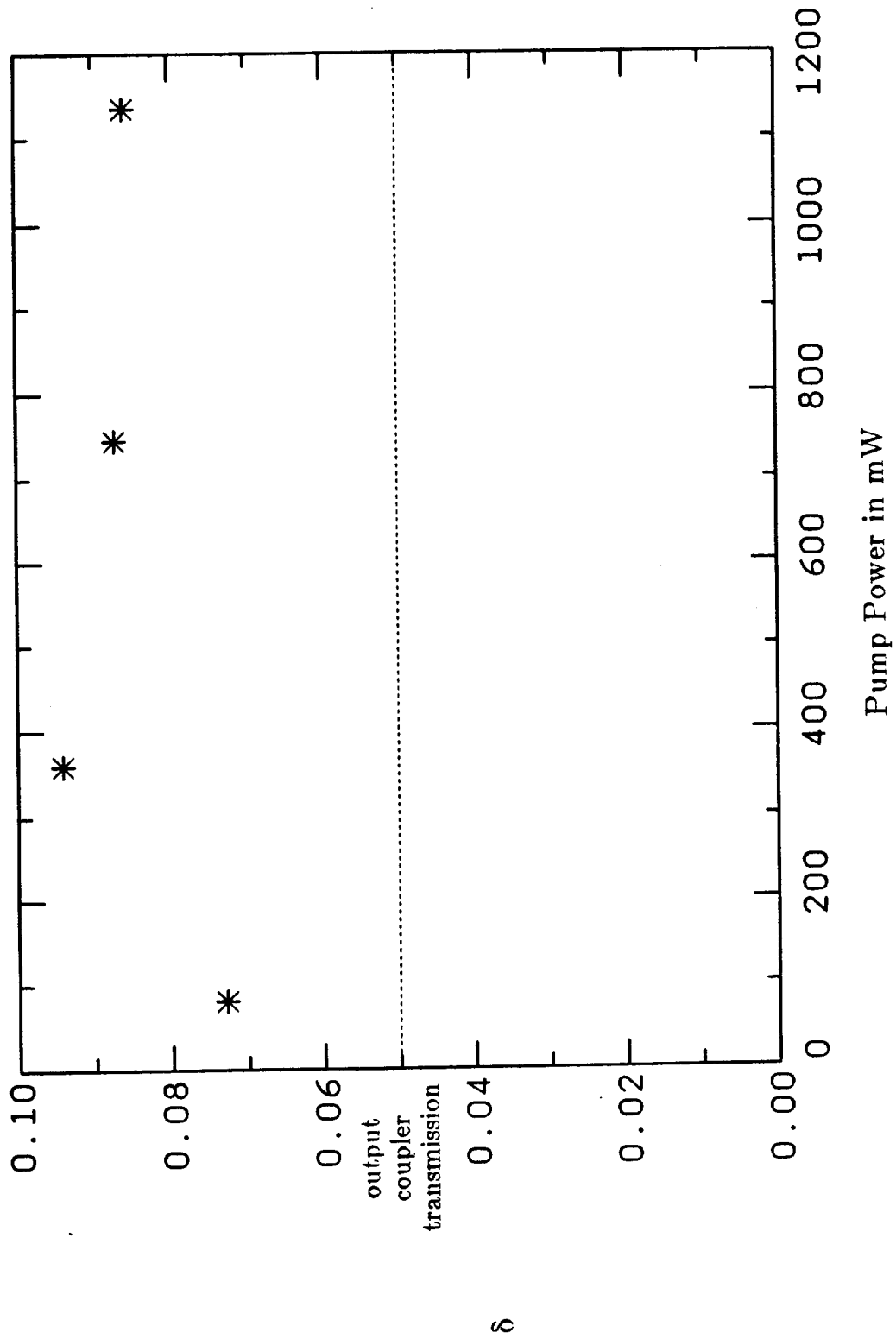
Figure 5.6.2   End-Pumped Nd:YAG Laser Model Test

6. SUMMARY AND CONCLUSIONS

The need for an improved methanometer was identified in Chapter 2. The DIAL technique using a diode laser pumped 1645-nm Er:YAG laser source was identified as an attractive possibility. Diode laser pumped 2.318-μm Tm:YAlO$_3$ was proposed as an alternate source.

The design of a methanometer for use in coal mines was discussed in Chapter 3, and it was shown that a hand-held real-time Er:YAG methanometer could meet performance requirements if the source was able to supply 50 mW of tunable CW power with a linewidth of 0.2 cm^{-1}.

The spectroscopy of Er:YAG was discussed in Chapter 4, and a rate equation model appropriate to diode pumping was introduced. The population inversion's dependence on pumping was linearized for use in the end-pumped rod model developed in Section 5.4. The measurement of the pump absorption cross-section and stimulated-emission cross-section was described.

In Chapter 5, the end-pumped geometry was shown to be crucial because of the large pump power densities needed to overcome the inherent inefficiencies of Er:YAG. A computer model was developed and used to optimize the design. It was found that a laser with an erbium concentration of 4 atom %, a rod length of 0.51 cm, a pump beam waist size of 40 μm, a cavity mode waist size of 33 μm and an output coupler reflectivity of 94 % was optimum to supply 50 mW output power, and that such a laser would have a threshold of 223 mW and a differential efficiency of .092. Finally, the model was adapted to Nd:YAG and compared with published data with good

agreement.

In summary, it is my opinion that a diode pumped 1645-nm Er:YAG laser could serve as a source for a hand-held real-time methanometer when diode laser pumps capable of supplying 1 W of CW power with good beam quality become available. Some possible pumping schemes are discussed in Appendix B. In the interim, a smaller ($\approx$1 mW output) Er:YAG laser with a single stripe diode laser or dye laser pump could be built and used to verify the end-pumped rod model of Chapter 5 and to demonstrate detection of methane[39, 53].

References

1. R. K. DeFreez, *A Diode Laser Source for DIAL Methane Measurements in Coal Mines*, Oregon Graduate Institute of Science and Technology, Beaverton, Oregon, May 1985. Ph.D. Thesis

2. D. Sliney and M. Wolbarsht, *Safety with Lasers and Other Optical Sources*, Plenum Press, New York, 1980.

3. A. M. Prokhorov, "A new generation of solid-state lasers," *Sov. Phys. Usp.*, vol. 29, pp. 3-19, January 1986.

4. "Portable Methane Detectors," *Title 30, Sub-Chapter D, Part 22*, U.S. Dept. of Commerce, Mine and Safety Administration, July 1980.

5. G. Schnakenberg, "Gas detection instrumentation... what's new and what's to come," *Coal Age*, pp. 84-92, March 1975.

6. H. Kildal and R. L. Byer, "Comparison of laser methods for the remote detection of atmospheric pollutants," *IEEE Proc.*, vol. 59, pp. 1644-1663, December 1971.

7. G. Herzberg, *Molecular Spectra and Molecular Structure: II. Infrared and Raman Spectra of Polyatomic Molecules*, D. Van Nostrand Co., Inc., Princeton, N.J., 1968.

8. R. A. McClatchey, W. S. Benedict, S. A. Clough, D. E. Burch, R. F. Calfee, K. Fox, L. S. Rothman, and J. S. Garing, *AFCRL Atmospheric Absorption Line Parameters Compilation*, Air Force Cambridge Research Laboratories, Bedford, Mass., 1973.

9. W. B. Grant and R. T. Menzies, "A survey of laser and selected optical systems for remote measurement of pollutant gas concentrations," *J. Air Poll. Control Assoc.*, vol. 33, pp. 187-194, March 1983.

10. L. S. Rothman, R. R. Gamache, A. Goldman, L. R. Brown, R. A. Toth, H. M. Pickett, R. L. Poynter, J. -M. Flaud, C. Camy-Peret, A. Barbe, N. Husson, C. P. Rinsland, and M. A. H. Smith, "The HITRAN database: 1986 edition," *Appl. Opt.*, vol. 26, pp. 4058-4097, 1 October 1987.

11. E. J. McCartney, *Absorption and Emission by Atmospheric Gases: The Physical Processes*, John Wiley and Sons, New York, N.Y., 1983.

12. W. B. Grant, "Helium-Neon Laser Remote Measurement of Methane at Landfill Sites," *Proceedings of the Conference on Resource Recovery from Solid Wastes*, p. 265, Pergamon Press, 1982.

13. J. A. Caird, L. G. DeShazer, and J. Nella, "Characteristics of Room-Temperature $2.3-\mu m$ Laser Emission from Tm^{3+} in YAG and $YAlO_3$," *IEEE J. Quantum Electron.*, vol. QE-11, pp. 874-881, November 1975.

14. *CRC Handbook of Laser Science and Technology, Volume I*, CRC Press, 1982.

15. K. Chan, H. Ito, and H. Inaba, "Absorption measurement of $\nu_2+2\nu_3$ Band of CH_4 at 1.33 μm using an InGaAsP light emitting diode," *Appl. Opt.*, vol. 22, pp. 3802-3804, 1 December 1983.

16. K. Chan, H. Ito, and H. Inaba, "Optical remote monitoring of CH_4 gas using low-loss optical fiber link and InGaAsP light-emitting diode in

1.33-µm region," *Appl. Phys. Lett.*, vol. 43, pp. 634-636, 1 October 1983.

17. K. O. White and S. A. Schleusener, "Coincidence of Er:YAG laser emission with methane absorption at 1645.1 nm," *Appl. Phys. Lett.*, vol. 21, pp. 419-420, 1 November 1972.

18. R. L. Byer, "Remote measurement of methane in a coal mine environment," Report from Stanford University Edward L. Ginzton Laboratory of Physics to Bethlehem Steel Corporation Homer Research Laboratories, August 1978.

19. W. D. Egan, "Remote measurement of methane in coal mines," Report BX-41-78010 IR, December 10 1979. Bethlehem Steel Corporation Homer Research Laboratories Internal Report, File #10066-3a

20. J. S. Blakemore and R. K. DeFreez, "Methane detection research," , October 1981. Report to Bethlehem Steel Corporation Homer Research Laboratories from Oregon Graduate Center

21. T. L. Koch and L. A. Coldren, "Optimum coupling junction and cavity lengths for coupled-cavity semiconductor lasers," *J. Appl. Phys.*, vol. 57, pp. 740-754, 1 February 1985.

22. R. K. DeFreez, J. Puretz, R. A. Elliott, J. Orloff, and L. W. Swanson, "CW operation of widely and continuously tunable micromachined-coupled-cavity diode lasers," *Electron. Lett.*, vol. 22, pp. 919-921, 14 August 1986.

23. W. Streifer, D. R. Scifres, G. L. Harnagel, D. F. Welch, J. Berger, and M. Sakamoto, "Advances in diode laser pumps," *IEEE J. Quantum Electron.*, vol. 24, pp. 883-894, June 1988.

24. L. F. Johnson, J. E. Geusic, and L. G. Van Uitert, "Coherent Oscillations from Tm^{3+}, Ho^{3+}, Yb^{3+} and Er^{3+} Ions in Yttrium Aluminum Garnet," *Appl. Phys. Lett.*, vol. 7, pp. 127-129, 1 September 1965.

25. G. Huber, E. W. Duczynski, and K. Petermann, "Laser pumping of Ho-, Tm-, Er-doped garnet lasers at room temperature," *IEEE J. Quantum Electron.*, vol. 24, pp. 920-923, June 1988.

26. D. K. Killinger, "Phonon-assisted upconversion in 1.64 µm Er:YAG lasers," *Technical Digest of CLEO '87*, p. 240, Baltimore, 26 April - 1 May 1987. Paper THJ4

27. T. Y. Fan and R. L. Byer, "Diode Laser-Pumped Solid-State Lasers," *IEEE J. Quantum Electron.*, vol. 24, pp. 895-912, June 1988.

28. L. Reekie, I. M. Jauncey, S. B. Poole, and D. N. Payne, "Diode-laser pumped operation of an Er^{3+}-doped single-mode fibre laser," *Electron. Lett.*, vol. 23, pp. 1076-1078, 24 September 1987.

29. J. Berger, D. F. Welch, D. R. Scifres, W. Streifer, and P. S. Cross, "High power, high efficient neodymium:yttrium aluminum garnet laser end pumped by a laser diode array," *Appl. Phys. Lett.*, vol. 51, pp. 1212-1214, 19 October 1987.

30. A. A. Kaminskii, T. I. Butaeva, V. A. Fedorov, Kh. S. Bagdasarov, and A. G. Petrosyan, "Absorption, Luminescence, and Stimulated Emission Investigations in $Lu_3Al_5O_{12}-Er^{3+}$ Crystals," *Phys. Stat. Sol. (a)*, vol. 39,

pp. 541-548, 1977.

31. W. Koechner, *Solid-State Laser Engineering* 2nd Edition, Springer-Verlag, New York, 1988.

32. R. Khazanie, *Elementary Statistics in a World of Applications*, Goodyear Publishing Company, Inc., 1979.

33. W. Koechner, in *Solid-State Laser Engineering* 1st Edition, Springer-Verlag, New York, 1976.

34. M. J. Weber, "Probabilities for Radiative and Nonradiative Decay of Er^{3+} in LaF_3," *Phys. Rev.*, vol. 157, pp. 262-272, 10 May 1967.

35. V. I. Zhekov, T. M. Murina, A. M. Prokhorov, M. I. Studenikin, S. Georgescu, V. Lupei, and I. Ursu, "Cooperative process in $Y_3Al_5O_{12}:Er^{3+}$ crystals," *Sov. J. Quantum Electron.*, vol. 16, pp. 274-276, February 1986.

36. Kh. S. Bagdasarov, V. I. Zhekov, V. A. Lobachev, A. A. Manenkov, T. M. Murina, and A. M. Prokhorov, "Cross relaxation of a laser based on yttrium-aluminum garnet with Er^{3+}," *Bull. Acad. Sci. USSR, Phys. Ser.*, vol. 48, pp. 114-119, 1984.

37. W. D. Egan, *Private Communication.*

38. J. T. Lin, "Materials Selection and Optimization of Diode-Pumped Lasers," *Proceedings of the International Conference on Lasers, 1987*, pp. 404-411, STS Press, Arlington, VA, 1987.

39. T. P. Pearsall, M. Piskorski, A. Brochet, and J. Chevrier, "A $Ga_{0.47}In_{0.53}As/InP$ heterophotodiode with reduced dark current," *IEEE J. Quantum Electron.*, vol. QE-17, pp. 255-259, February 1981.

40. A. A. Kaminskii, A. G. Petrosyan, G. A. Denisenko, T. I. Butaeva, V. A. Fedorov, and S. E. Sarkisov, "Spectroscopic Properties and 3 μm Stimulated Emission of Er^{3+} Ions in the $(Y_{1-x}Er_x)_3Al_5O_{12}$ and $(Lu_{1-x}Er_x)_3Al_5O_{12}$ Garnet Crystal Systems," *phys. stat. sol. (a)*, vol. 71, pp. 291-312, 1982.

41. W. Q. Shi, M. Bass, and M. Birnbaum, "Investigation of the interactions between dissimilar ions in (Er,Nd): $Y_3Al_5O_{12}$," *J. Opt. Soc. Am. B*, vol. 6, pp. 23-29, January 1989.

42. *CRC Handbook of Laser Science and Technology, Volume V*, CRC Press, 1982.

43. E. V. Zharikov, V. I. Zhekov, L. A. Kulevskii, T. M. Murina, V. V. Osiko, A. M. Prokhorov, A. D. Savel'ev, V. V. Smirnov, B. P. Starikov, and M. I. Timoshechkin, "Stimulated emission from Er^{3+} ions in yttrium aluminum garnet crystals at $\lambda = 2.94$ μ," *Sov. J. Quantum Electron.*, vol. 4, pp. 1039-1040, February 1975.

44. T. T. Basiev, E. V. Kharikov, V. I. Zhekov, T. M. Murina, V. V. Osiko, A. M. Prokhorov, B. P. Starikov, M. I. Timoshechkin, and I. A. Shcherbakov, "Radiative and nonradiative transitions exhibited by Er^{3+} ions in mixed yttrium-erbium aluminum garnets," *Sov. J. Quantum Electron.*, vol. 6, pp. 796-799, July 1976.

45. Kh. S. Bagdasarov, V. I. Zhekov, V. A. Lobachev, A. A. Manenkov, T. M. Murina, A. M. Prokhorov, and E. A. Fedorov, "Yttrium-Erbium-Aluminum Garnet: a promising new crystal for IR lasers," *Bull. Acad. Sci. USSR, Phys. Ser.*, vol. 46, pp. 49-55, 1982.

46. Kh. S. Bagdasarov, V. I. Zhekov, V. A. Lobachev, T. M. Murina, and A. M. Prokhorov, "Steady-state emission from a $Y_3Al_5O_{12}:Er^{3+}$ laser $(\lambda=2.94 \mu$, T=300°K)," *Sov. J. Quantum Electron.*, vol. 13, pp. 262-263, February 1983.

47. V. I. Zhekov, V. A. Lobachev, T. M. Murina, and A. M. Prokorov, "Cooperative phenomena in yttrium aluminum garnet crystals," *Sov. J. Quantum Electron.*, vol. 14, pp. 128-130, January 1984.

48. Kh. S. Bagdasarov, V. P. Danilov, V. I. Zhekov, T. M. Murina, A. A. Manenkov, M. I. Timoshechkin, and A. M. Prokhorov, "Pulse-periodic $Y_3Al_5O_{12}:Er^{3+}$ laser with high activator concentration," *Sov. J. Quantum Electron.*, vol. 8, pp. 83-85, January 1978.

49. H. A. Haus, *Waves and Fields in Opto-electronics*, Prentice-Hall, Inc., Englewood Cliffs, New Jersey, 1984.

50. D. R. Scifres, R. A. Sprague, W. Streifer, and R. D. Burnham, "Focusing of a 7700-A high power phased array semiconductor laser," *Appl. Phys. Lett.*, vol. 41, pp. 1121-1123, 15 December 1982.

51. G. A. Evans, N. W. Carlson, J. M. Hammer, M. Lurie, J. K. Butler, S. L. Palfrey, R. Amantea, L. A. Carr, F. Z. Hawrylo, E. A. James, C. J. Kaiser, J. B. Kirk, and W. F. Reichert, "Two-Dimensional Coherent Laser Arrays Using Grating Surface Emission," *IEEE J. of Quantum Electron.*, vol. 25, pp. 1525-1535, June 1989.

52. J. W. Goodman, *Introduction to Fourier Optics*, McGraw-Hill, San Francisco, 1968.

53. R. K. DeFreez, *Private Communication*.

APPENDIX A

ERYAGLASER calculates the incident diode laser pump power needed to produce a specified coherent output power from an end-pumped 1645 nm Er:YAG laser using the model developed in Section 5.4. It was used to generate the numerical simulations given in Section 5.5.

BERGER calculates the round-trip cavity loss as a function of incident pump power and coherent output power of the end-pumped 1064 nm Nd:YAG laser described by Berger et. al. (Reference 29) and is developed and used in Section 5.6.

INVERSION calculates the exact (Equation 4.4.15) and approximate (Equation 4.4.16) inversion populations as a function of pumping, with no stimulated emission present. It was used to generate Figures 4.4.1-3.

OVERLAP calculates the pump beam and cavity mode overlap integral given by Equation 5.3.3 and was used to generate Figure 5.3.1.

```
C ERYAGLASER by Geoffrey Wilson 16 August 1989
C
C Calculates the incident diode laser pump power needed to produce
C a specified coherent output from an end-pumped Er:YAG laser
C using the model developed in section 5.4.
C
C Reads the following material parameters from file "eryaglaser.prm":
C   lamp  = pump wavelength in cm
C   lam0  = lasing wavelength in cm
C   nrp   = YAG index of refraction at lamp
C   nr0   = YAG index of refraction at lam0
C   eta   = pump-to-upper lasing level manifold quantum efficiency
C   sigp  = pump absorption "cross-section" in 1/cm/atom %
C   sig0  = stimulated cross-section in 1/cm/atom %
C   tau1  = lifetime of manifold 1 in s
C   tau2  = lifetime of manifold 2 in s
C   omega = co-operative process coefficient in 1/s/(atom %)**3
C   alfi  = YAG scattering loss coefficient at lam0 in 1/cm
C
C and gets the remainder of the necessary data from the terminal:
C   delf  = round-trip cavity loss
C   pout  = output power in W
C   c     = Er concentration in atom %
C   t     = temperature in K
C   l     = Er:YAG rod length in cm
C   wp    = pump beam waist size in cm
C   w0    = cavity mode waist size in cm
C   x     = output coupler transmission
C
C One of the six final variables can be scanned over a range while the
C other five are held constant or optimized. Any or all of the final
C four may be simultaneously optimized to minimize the pump power.
C
C Program output consists of six output files of the form "zzzz.suffix"
C where "zzzz" is a four-character string specified by the user. The
C files consist of ordered pairs; the first of each pair is the vari-
C able being scanned over, the second number is the information implied
C by the file suffix = pin, xmax, long, wp, w0 or trns.
C
        integer opt,ic,it,il,iwp,iw0,ix
        integer cstp,tstp,lstp,wpstp,w0stp,xstp,zstp,vstp,scan
        real tol,rt3,hc,pi
        real lamp,lam0,nrp,nr0,eta,sigp,sig0,fa,fb,tau1,tau2,omega
        real delf,pout,pin,a,g,u,qa,qb,n0inv,n1inv,x2inv,xinv
        real alfp,hfalfp,q5,xx,alfi,xmax
        real t,tlo,thi,tinc,c,clo,chi,cinc,l,llo,lhi,linc
        real wp,wplo,wphi,wpinc,w0,w0lo,w0hi,w0inc,x,xlo,xhi,xinc
        real ll,lm,lh,wpl,wpm,wph,w0l,w0m,w0h,hl,hm,hh
        real lmold,wpmold,w0mold,hmold,ycap0,pin0
        character*45 txt
        character*4 fn
        logical lflg,wpflg,w0flg,xflg
        common/tranya/pi,lamp,lam0,nrp,nr0,zstp,vstp,hfalfp,a,g,u
        common/quaatlu/ycap0,q5,delf,alfi,pin0,xinv,x2inv,n1inv
C Constants.
        rt3=sqrt(3.)
        pi=3.14159
C Fractional tolerance to which variables are optimized.
        tol=1.e-02
C Steps used in integration over the rod in the axial dimension.
        zstp=20
C Steps used in integration over the rod in the radial dimension.
        vstp=20
C Planck's constant x speed of light in J/cm**2/atom % (1 atom % =
C 1.38x10**20 1/cm**3 in YAG).
        hc=2.74e-03
```

```
C Open and read or write to parameter file 'eryaglaser.prm'.
      print*,'Read old parameter file (0) or write new one (<>0)?'
      read*,opt
      open(unit=1,file='eryaglaser.prm')
      if (opt.eq.0) then
        read(1,50)txt,lamp
        read(1,50)txt,lam0
        read(1,50)txt,nrp
        read(1,50)txt,nr0
        read(1,50)txt,eta
        read(1,50)txt,sigp
        read(1,50)txt,sig0
        read(1,50)txt,tau1
        read(1,50)txt,tau2
        read(1,50)txt,omega
        read(1,50)txt,alfi
      else
        print*,'Pump wavelength (cm)'
        read*,lamp
        txt='Pump wavelength (cm)                       ='
        write(1,50)txt,lamp
        print*,'Lasing wavelength (cm)'
        read*,lam0
        txt='Lasing wavelength (cm)                     ='
        write(1,50)txt,lam0
        print*,'Pump wavelength YAG index of refraction'
        read*,nrp
        txt='Pump wavelength YAG index of refraction    ='
        write(1,50)txt,nrp
        print*,'Lasing wavelength YAG index of refraction'
        read*,nr0
        txt='Lasing wavelength YAG index of refraction  ='
        write(1,50)txt,nr0
        print*,'Pump quantum efficiency'
        read*,eta
        txt='Pump quantum efficiency                    ='
        write(1,50)txt,eta
        print*,'Pump absorption "cross-section" (1/cm/%)'
        read*,sigp
        txt='Pump absorption "cross-section" (1/cm/%)   ='
        write(1,50)txt,sigp
        print*,'Lasing transition cross-section (1/cm/%)'
        read*,sig0
        txt='Lasing transition cross-section (1/cm/%)   ='
        write(1,50)txt,sig0
        print*,'Manifold 1 lifetime (s)'
        read*,tau1
        txt='Manifold 1 lifetime (s)                    ='
        write(1,50)txt,tau1
        print*,'Manifold 2 lifetime (s)'
        read*,tau2
        txt='Manifold 2 lifetime (s)                    ='
        write(1,50)txt,tau2
        print*,'Co-operative process coefficient (1/%3/s)'
        read*,omega
        txt='Co-operative process coefficient (1/%3/s)  ='
        write(1,50)txt,omega
        print*,'YAG scattering loss coefficient (1/cm)'
        read*,alfi
        txt='YAG scattering loss coefficient (1/cm)     ='
        write(1,50)txt,alfi
      end if
      close(unit=1)
C Done with 'threshold.prm'.
C See (4.4.5).
      u=tau2/tau1
```

```
C Get additional information from the terminal.
      print*,'Round-trip length-independent cavity loss'
      read*,delf
      print*,'Output power (W)'
      read*,pout
C Establish scan mode.
      print*,'Specify scan mode'
      print*,'      (1) to scan Er concentration range'
      print*,'      (2) to scan temperature range'
      print*,'      (3) to scan rod length range'
      print*,'      (4) to scan pump beam waist size range'
      print*,'      (5) to scan cavity mode waist size range'
      print*,'      (6) to scan output coupling range'
      read*,scan
C Get scan ranges from the terminal.
      if (scan.eq.1) then
        print*,'Concentrations in %; lo, hi, steps :'
        read*,clo,chi,cstp
        call range(clo,chi,cstp,cinc)
      else
        print*,'Concentration in % :'
        read*,clo
      end if
      if (scan.eq.2) then
        print*,'Temperature in K; lo, hi, steps :'
        read*,tlo,thi,tstp
        call range(tlo,thi,tstp,tinc)
      else
        print*,'Temperature in K :'
        read*,tlo
      end if
      if (scan.eq.3) then
        print*,'Rod length in cm; lo, hi, steps :'
        read*,llo,lhi,lstp
        call range(llo,lhi,lstp,linc)
      else
        print*,'Optimize (0) or specify (<>0) rod length?'
        read*,opt
        if (opt.eq.0) then
          lflg=.true.
        else
          lflg=.false.
          print*,'Rod length in cm :'
          read*,llo
        end if
      end if
      if (scan.eq.4) then
        print*,'Pump beam waist size; lo, hi, steps :'
        read*,wplo,wphi,wpstp
        call range(wplo,wphi,wpstp,wpinc)
      else
        print*,'Optimize (0) or specify (<>0) pump beam waist size?'
        read*,opt
        if (opt.eq.0) then
          wpflg=.true.
        else
          wpflg=.false.
          print*,'Pump beam waist size :'
          read*,wplo
        end if
      end if
      if (scan.eq.5) then
        print*,'Cavity mode waist size; lo, hi, steps :'
        read*,w0lo,w0hi,w0stp
        call range(w0lo,w0hi,w0stp,w0inc)
      else
```

```
            print*,'Optimize (0) or specify (<>0) cavity mode waist size?'
            read*,opt
            if (opt.eq.0) then
              w0flg=.true.
            else
              w0flg=.false.
              print*,'Cavity mode waist size :'
              read*,w0lo
            end if
          end if
          if (scan.eq.6) then
            print*,'Output coupling; lo, hi, steps :'
            read*,xlo,xhi,xstp
            call range(xlo,xhi,xstp,xinc)
          else
            print*,'Optimize (0) or specify (<>0) output coupling?'
            read*,opt
            if (opt.eq.0) then
              xflg=.true.
            else
              xflg=.false.
              print*,'Output coupling :'
              read*,xlo
            end if
          end if
          print*,'Supply 4 character name for output files'
          read*,fn
C Done getting information from the terminal.
C Open output files.
          open(unit=1,file=fn//'.pin')
          open(unit=2,file=fn//'.xmax')
          open(unit=3,file=fn//'.long')
          open(unit=4,file=fn//'.wp')
          open(unit=7,file=fn//'.w0')
          open(unit=8,file=fn//'.trns')
C Begin scan loops. Outer loop scans over temperature.
          do 100 it=0,tstp
          t=tlo+it*tinc
C Calculate the boltzmann factors of the upper and lower lasing levels.
          call boltzmann(t,fa,fb)
C See (4.4.4).
          g=fa/fb
C Scan over Er concentration.
          do 100 ic=0,cstp
          c=clo+ic*cinc
C See (4.4.3) and (4.5.4).
          a=tau1*omega*c**3.
C Calculate inversion threshold populations and pumping (4.4.8-10).
          qa=2.*a*g*g*u
          qb=1.+(1.+u)*g
          qc=1.
          if (2.*qa*qc.lt.qb/100.) then
            n0inv=qc/qb
          else
            n0inv=.5*(sqrt(qb*qb+4.*qa*qc)-qb)/qa
          end if
          n1inv=g*n0inv
          x2inv=g*(1.+a*n1inv)
          xinv=sqrt(x2inv)
C See (5.2.6).
          alfp=c*n0inv*sigp
          hfalfp=.5*alfp
C See (4.4.7), (5.4.1-2) and (5.1.1).
          ycap0=4./pi*sig0*lam0/hc*tau1*fb*pout
C See (5.4.6).
          pin0=.5*pi*hc/lamp/eta/tau1/n0inv/sigp
```

```
         q5=.5/sig0/c/fb
C Scan over rod length, pump beam waist size, cavity mode waist size
C and output coupler transmission.
         do 100 il=0,lstp
         l=llo+il*linc
         do 100 iwp=0,wpstp
         wp=wplo+iwp*wpinc
         do 100 iw0=0,w0stp
         w0=w0lo+iw0*w0inc
         do 100 ix=0,xstp
         x=xlo+ix*xinc
C Begin optimization procedure.
C Initialize intermediate values.
         if (lflg) then
C Assumes optimum length x pump absorption coefficient = 1.
           lm=1./alfp
         else
           lm=l
         end if
         if (wpflg) then
C See (5.2.4).
           wpm=sqrt(lamp*lm/pi/nrp/rt3)
         else
           wpm=wp
         end if
         if (w0flg) then
C See section 5.3, diffraction-limited minimum volume regime.
           w0m=1.221*wpm
         else
           w0m=w0
         end if
         if (xflg) then
C Assumes transmission should be comparable to other losses.
           hm=-log(delf+alfi*lm)
         else
           hm=-log(x)
         end if
C
C Begin optimization cycle. Optimization works by calculating the
C pump power at three values of the optimized variable: an inter-
C mediate value, a lesser value and a greater value. If "pin" is
C smaller for the intermediate value than for either of the extreme
C values, the range is narrowed. If "pin" is smallest for an extreme
C value, the range is shifted that way. This continues until the
C preset tolerance is met.
C
C Record old values.
10       lmold=lm
         wpmold=wpm
         w0mold=w0m
         hmold=hm
C Begin rod length optimization section.
         if (lflg) then
           ll=.5*lm
           lh=2.*lm
20         call pwr(ll,wpm,w0m,exp(-hm),pl,xmax)
           call pwr(lm,wpm,w0m,exp(-hm),pm,xmax)
           call pwr(lh,wpm,w0m,exp(-hm),ph,xmax)
           call reshuffle(pl,pm,ph,ll,lm,lh)
           if ((lh/ll-1.).gt.tol) go to 20
         end if
C Begin pump beam waist size optimization section.
         if (wpflg) then
           wpl=.5*wpm
           wph=2.*wpm
30         call pwr(lm,wpl,w0m,exp(-hm),pl,xmax)
```

```
            call pwr(lm,wpm,w0m,exp(-hm),pm,xmax)
            call pwr(lm,wph,w0m,exp(-hm),ph,xmax)
            call reshuffle(pl,pm,ph,wpl,wpm,wph)
            if ((wph/wpl-1.).gt.tol) go to 30
        end if
C Begin cavity mode waist size optimization section.
        if (w0flg) then
            w0l=.5*w0m
            w0h=2.*w0m
40          call pwr(lm,wpm,w0l,exp(-hm),pl,xmax)
            call pwr(lm,wpm,w0m,exp(-hm),pm,xmax)
            call pwr(lm,wpm,w0h,exp(-hm),ph,xmax)
            call reshuffle(pl,pm,ph,w0l,w0m,w0h)
            if ((w0h/w0l-1.).gt.tol) go to 40
        end if
C Begin output coupling optimization section.
        if (xflg) then
            hl=.5*hm
            hh=2.*hm
45          call pwr(lm,wpm,w0m,exp(-hl),pl,xmax)
            call pwr(lm,wpm,w0m,exp(-hm),pm,xmax)
            call pwr(lm,wpm,w0m,exp(-hh),ph,xmax)
            call reshuffle(pl,pm,ph,hl,hm,hh)
            if ((hh/hl-1.).gt.tol) go to 45
        end if
C Compare new values with old values, continue if no convergence.
        if (abs(lm/lmold-1.).gt.tol) go to 10
        if (abs(wpm/wpmold-1.).gt.tol) go to 10
        if (abs(w0m/w0mold-1.).gt.tol) go to 10
        if (abs(hm/hmold-1.).gt.tol) go to 10
C Finished optimizing.
C Establish scan variable to be written to output files.
        if (scan.eq.1) then
            xx=c
        end if
        if (scan.eq.2) then
            xx=t
        end if
        if (scan.eq.3) then
            xx=l
        end if
        if (scan.eq.4) then
            xx=wp
        end if
        if (scan.eq.5) then
            xx=w0
        end if
        if (scan.eq.6) then
            xx=x
        end if
C Begin writing output files.
        print*,it,ic,il,iwp,iw0,ix
        call pwr(lm,wpm,w0m,exp(-hm),pin,xmax)
C Record pump power in fn//'.pin'.
        write(1,*)xx,pin
C Record fn//'.xmax' to monitor validity of inversion linearization.
        write(2,*)xx,xmax
C Record rod length in fn//'.long'.
        write(3,*)xx,lm
C Record pump beam waist size in fn//'.wp'.
        write(4,*)xx,wpm
C Record cavity mode waist size in fn//'.w0'.
        write(7,*)xx,w0m
C Record output coupling in fn//'.trns'.
        write(8,*)xx,exp(-hm)
100     continue
```

```fortran
      close(unit=1)
      close(unit=2)
      close(unit=3)
      close(unit=4)
      close(unit=7)
      close(unit=8)
C     close(unit=9)
      stop
50    format(A45,T50,E12.6)
      end
C************************************************************************
      subroutine pwr(l,wp,w0,trns,pin,xmax)
C Calculates "pin" and "xmax" according to (5.4.6) and (5.4.10).
C Note: xmax(program) = xmax/xinv(5.4.10).
      integer iz,iv,zstp,vstp
      real pi,lamp,lam0,nrp,nr0,hfalfp,a,g,u,ycap0,q5,delf,alfi
      real pin0,xinv,x2inv,nlinv,l,wp,w0,trns,pin,xmax
      real wp2,w02,bp,b0,bp2,b02,dz,loss,ycap,sum1,sum2,sum3,sum4
      real z,z2,wpz2,w0z2,hfgam,v,h1,h2,dn1dx,chi,ycap1,ycap2
      common/tranya/pi,lamp,lam0,nrp,nr0,zstp,vstp,hfalfp,a,g,u
      common/quaatlu/ycap0,q5,delf,alfi,pin0,xinv,x2inv,nlinv
      wp2=wp*wp
      w02=w0*w0
C See (5.1.3).
      bp=pi*nrp*wp2/lamp
      b0=pi*nr0*w02/lam0
      bp2=bp*bp
      b02=b0*b0
C Axial mesh size.
      dz=1/zstp
C See (5.4.6).
      loss=q5*(trns+delf+alfi*l)
C See (5.4.2).
      ycap1=ycap0/trns
C Initialize outer integral in numerator of (5.4.6).
      sum1=0.
C Initialize outer integral in denominator of (5.4.6).
      sum2=0.
C Enter z integration loop.
      do 7000 iz=1,zstp
      z=(iz-.5)*dz
      z2=z*z
C See (5.1.2).
      wpz2=wp2*(1.+z2/bp2)
      w0z2=w02*(1.+z2/b02)
C See (5.4.8).
      hfgam=.5*w0z2/wpz2
C See (5.1.1).
      ycap2=ycap1/w0z2
C Initialize inner integral in numerator of (5.4.6).
      sum3=0.
C Initialize inner integral in denominator of (5.4.6).
      sum4=0.
C Enter v [see (5.4.7)] integration loop.
      do 6000 iv=1,vstp
      v=(iv-.5)/vstp
C See (5.1.1).
      ycap=ycap2*v
C See (4.4.18).
      h1=1.+u*g*ycap+2.*u*x2inv
      h2=1.+u+u*ycap
      dn1dx=2.*xinv*(1.-h2*nlinv-2.*u*a*nlinv*nlinv)/
     &(2.*a*h1*nlinv+(1.+(1.+g)*ycap+h2*x2inv))
      chi=((1.+g*(1.-u)+2.*u*x2inv)*dn1dx+4.*u*xinv*nlinv)/h1
      sum3=sum3+chi
      sum4=sum4+chi*v**hfgam
```

```
6000  continue
      sum3=sum3/vstp
      sum4=sum4/vstp
      sum1=sum1+sum3
      sum2=sum2+sum4*sqrt(wp2/wpz2)*exp(-hfalfp*z)
7000  continue
      sum1=sum1*dz
      sum2=sum2*dz
C See (5.4.9).
      xmax=(loss+xinv*sum1)/sum2
C See (5.4.6).
      pin=pin0*wp2*xmax*xmax
C See (5.4.10).
      xmax=xmax/xinv
      return
      end
C****************************************************************
      subroutine boltzmann(t,fa,fb)
C Calculates the boltzmann factors of the upper and lower lasing levels.
      integer i
      real t,tb,fa,fb,ea(2:8),eb(2:7)
C Er:YAG manifold 0 energy levels in 1/cm.
      data ea/19.,57.,76.,411.,424.,523.,568./
C Er:YAG manifold 1 energy levels in 1/cm.
      data eb/52.,58.,235.,256.,274.,335./
C Convert temperature from Kelvin to inverse centimeters.
      tb=.6947*t
C Calculate the Boltzmann factors for lower and upper lasing levels.
      fa=1.
      do 8000 i=2,8
      fa=fa+exp(-ea(i)/tb)
8000  continue
      fa=exp(-ea(7)/tb)/fa
      fb=1.
      do 9000 i=2,7
      fb=fb+exp(-eb(i)/tb)
9000  continue
      fb=exp(-eb(3)/tb)/fb
      return
      end
C****************************************************************
      subroutine range(xlo,xhi,xstp,xinc)
C Calculates the increment of a variable given the start and stop
C points and number of steps.
      integer xstp
      real xlo,xhi,xinc
      if (xstp.eq.0) then
        xinc=0.
      else
        xinc=(xhi-xlo)/xstp
      end if
      return
      end
C****************************************************************
      subroutine reshuffle(yl,ym,yh,xl,xm,xh)
C Adjusts optimization ranges as explained in main body comment.
      real yl,ym,yh,xl,xm,xh
      if ((ym.le.yl).and.(ym.le.yh)) then
C Narrow range by taking geometric means.
        xl=sqrt(xl*xm)
        xh=sqrt(xh*xm)
      else
        if (yl.gt.yh) then
C Shift range downscale.
          xl=xm
          xm=xh
```

```
            xh=xm*xm/xl
          else
C Shift range upscale.
            xh=xm
            xm=xl
            xl=xm*xm/xh
        end if
      end if
      return
      end
```

```
C BERGER by Geoffrey Wilson 8 September 1989
C
C Calculates the round-trip cavity loss as a function of incident
C pump power and coherent output power of an end-pumped Nd:YAG
C laser (see section 5.6).
C
C Reads the following parameters from file "berger.prm":
C    lamp  = pump wavelength in cm
C    lam0  = lasing wavelength in cm
C    nrp   = YAG index of refraction at lamp
C    nr0   = YAG index of refraction at lam0
C    eta   = pump-to-upper lasing level manifold quantum efficiency
C    sigp  = pump absorption "cross-section" in 1/cm/atom %
C    sig0  = stimulated cross-section in 1/cm/atom %
C    taul  = lifetime of manifold 1 in s
C    conc  = Nd concentration in atom %
C    temp  = temperature in K
C    long  = Er:YAG rod length in cm
C    wp    = pump beam waist size in cm
C    w0    = cavity mode waist size in cm
C    trns  = output coupler transmission
C
C and reads the experimental data points (pin,pout) from "berger.popi".
C    pin   = pump power in W
C    pout  = output power in W
C
C Program output consists of "berger.delta" which contains ordered
C pairs of the form (pin,delta=delf+trns), where "delf" is cavity
C loss other than output.
C
      integer opt,npnt,iz,zstp,iv,vstp
      real hc,pi,lamp,lam0,nrp,nr0,eta,sigp,sig0,fa,fb,taul
      real conc,temp,long,wp,w0,trns,alfp,pout,pin,g,gl
      real ycap0,ycap1,ycap2,ycap,x2cap0,x2cap1,x2cap2,x2cap
      real coeff,wp2,w02,bp,b0,bp2,b02,dz,sum,z,z2,zshft,zshft2
      real wpz2,w0z2,gamma,v
      character*45 txt
C Constants.
      pi=3.14159
C Steps used in integration over the rod in the axial dimension.
      zstp=20
C Steps used in integration over the rod in the radial dimension.
      vstp=20
C Planck's constant x speed of light in J/cm**2/atom % (1 atom % =
C 1.38x10**20 1/cm**3 in YAG).
      hc=2.74e-03
C Open and read or write to parameter file 'berger.prm'.
      print*,'Read old parameter file (0) or write new one (<>0)?'
      read*,opt
      open(unit=1,file='berger.prm')
      if (opt.eq.0) then
        read(1,50)txt,lamp
        read(1,50)txt,lam0
        read(1,50)txt,nrp
        read(1,50)txt,nr0
        read(1,50)txt,eta
        read(1,50)txt,sigp
        read(1,50)txt,sig0
        read(1,50)txt,taul
        read(1,50)txt,conc
        read(1,50)txt,temp
        read(1,50)txt,long
        read(1,50)txt,wp
        read(1,50)txt,w0
        read(1,50)txt,trns
      else
```

```
      print*,'Pump wavelength (cm)'
      read*,lamp
      txt='Pump wavelength (cm)                    ='
      write(1,50)txt,lamp
      print*,'Lasing wavelength (cm)'
      read*,lam0
      txt='Lasing wavelength (cm)                  ='
      write(1,50)txt,lam0
      print*,'Pump wavelength YAG index of refraction'
      read*,nrp
      txt='Pump wavelength YAG index of refraction    ='
      write(1,50)txt,nrp
      print*,'Lasing wavelength YAG index of refraction'
      read*,nr0
      txt='Lasing wavelength YAG index of refraction   ='
      write(1,50)txt,nr0
      print*,'Pump quantum efficiency'
      read*,eta
      txt='Pump quantum efficiency                  ='
      write(1,50)txt,eta
      print*,'Pump absorption "cross-section" (1/cm/@%)'
      read*,sigp
      txt='Pump absorption "cross-section" (1/cm/@%)   ='
      write(1,50)txt,sigp
      print*,'Lasing transition cross-section (1/cm/@%)'
      read*,sig0
      txt='Lasing transition cross-section (1/cm/@%)   ='
      write(1,50)txt,sig0
      print*,'Manifold 1 lifetime (s)'
      read*,tau1
      txt='Manifold 1 lifetime (s)                  ='
      write(1,50)txt,tau1
      print*,'Nd concentration (@%)'
      read*,conc
      txt='Nd concentration (@%)                    ='
      write(1,50)txt,conc
      print*,'Operating temperature (K)'
      read*,temp
      txt='Operating temperature (K)                ='
      write(1,50)txt,temp
      print*,'Rod length (cm)'
      read*,long
      txt='Rod length (cm)                          ='
      write(1,50)txt,long
      print*,'Pump beam waist size (cm)'
      read*,wp
      txt='Pump beam waist size (cm)                ='
      write(1,50)txt,wp
      print*,'Cavity mode waist size (cm)'
      read*,w0
      txt='Cavity mode waist size (cm)              ='
      write(1,50)txt,w0
      print*,'Output coupler transmission'
      read*,trns
      txt='Output coupler transmission              ='
      write(1,50)txt,trns
      end if
      close(unit=1)
C Done with 'berger.prm'.
C Calculate the boltzmann factors of the upper and lower lasing levels.
      call boltzmann(temp,fa,fb)
C See (4.4.4).
      g=fa/fb
      g1=1.+g
C See (5.6.3).
      alfp=sigp*conc
```

```fortran
C See (4.4.7), (5.4.1-2) and (5.1.1).
      ycap0=4./pi*sig0*lam0/hc*tau1*fb/trns
C See (4.4.6) and (5.4.4).
      x2cap0=2./pi*sigp*lamp/hc*tau1*eta
C See (5.6.4).
      coeff=2.*sig0*conc*fb
      wp2=wp*wp
      w02=w0*w0
C See (5.1.3).
      bp=pi*nrp*wp2/lamp
      b0=pi*nr0*w02/lam0
      bp2=bp*bp
      b02=b0*b0
C Axial mesh size.
      dz=long/zstp
C Open and read or write to data file 'berger.popi'.
      print*,'Read old data file (0) or write new one (<>0)?'
      read*,opt
      open(unit=1,file='berger.popi')
      if (opt.eq.0) then
        read(1,*)npnt
      else
        print*,'Number of ordered pairs'
        read*,npnt
        write(1,*)npnt
      end if
C Open output file 'berger.delta'.
      open(unit=2,file='berger.delta')
C Begin loop through P(out) versus P(in) data set.
      do 100 i=1,npnt
C Read or write ordered pair.
      if (opt.eq.0) then
        read(1,*)pin,pout
      else
        print*,'pin, pout (W)'
        read*,pin,pout
        write(1,*)pin,pout
      end if
C See (5.6.6).
      ycap1=ycap0*pout
C See (5.6.5).
      x2cap1=x2cap0*pin
C Initialize gain intergral.
      sum=0.
C Enter z integration loop.
      do 90 iz=1,zstp
      z=(iz-.5)*dz
      z2=z*z
C "zshft" accounts for the pump beam waist at the midpoint of the rod
C as implied in Berger et. al. (1987).
      zshft=z-.5*long
      zshft2=zshft*zshft
C See (5.1.2).
      wpz2=wp2*(1.+zshft2/bp2)
      w0z2=w02*(1.+z2/b02)
C See (5.4.8).
      gamma=w0z2/wpz2
C See (5.6.6).
      ycap2=ycap1/w0z2
C See (5.6.5).
      x2cap2=x2cap1/wpz2*exp(-alfp*z)
C Enter v [see (5.4.7)] integration loop.
      do 90 iv=1,vstp
      v=(iv-.5)/vstp
C See (5.6.4).
      ycap=ycap2*v
```

```
      x2cap=x2cap2*v**gamma
      sum=sum+(x2cap-g)/(1.+g1*ycap+x2cap)
90    continue
      write(2,*)pin,coeff*sum*dz/vstp
100   continue
      close(unit=1)
      close(unit=2)
      stop
50    format(A45,T50,E12.6)
      end
C********************************************************************
      subroutine boltzmann(t,fa,fb)
C Calculates the boltzmann factors of the upper and lower lasing levels.
      integer i
      real t,tb,fa,fb,ea(2:11),eb(2:2)
C Nd:YAG manifold 0 energy levels in 1/cm.
      data ea/134.,197.,311.,848.,2001.,2029.,2111.,2146.,2473.,2526./
C Nd:YAG manifold 1 energy levels in 1/cm.
      data eb/88./
C Convert temperature from Kelvin to inverse centimeters.
      tb=.6947*t
C Calculate the Boltzmann factors for lower and upper lasing levels.
      fa=1.
      do 8000 i=2,11
      fa=fa+exp(-ea(i)/tb)
8000  continue
      fa=exp(-ea(8)/tb)/fa
      fb=1.
      do 9000 i=2,2
      fb=fb+exp(-eb(i)/tb)
9000  continue
      fb=exp(-eb(2)/tb)/fb
      return
      end
```

```
C INVERSION by Geoffrey Wilson 22 August 1989
C
C Calculates the exact and approximate inversion population of the
C Er:YAG 1645 nm laser as a function of pumping, with no stimulated
C emission present (Y=0). Used to generate figures 4.4.1a-c. See
C section 4.4.
C
C Reads Er:YAG parameters from "eryaglaser.prm" (see "eryaglaser.f"
C source listing) and gets additional data from the terminal.
C
C Program output consists of "delta.exact" and " delta.aprox",
C which contain normalized data points (pumping,inversion).
C
      integer iv,vstp
      real lamp,lam0,nrp,nr0,eta,sigp,sig0,fa,fb,tau1,tau2,omega
      real a,g,u,qa,qb,qc,n0inv,n1inv,x2inv,xinv,h1,h2,dn1dx,chi
      real tlo,clo,vlo,vhi,vinc,v,n1e,n0e,x,x2,dlte,dlta,alfi
      character*45 txt
C Open and read or write to parameter file 'eryaglaser.prm'.
      open(unit=1,file='eryaglaser.prm')
      read(1,50)txt,lamp
      read(1,50)txt,lam0
      read(1,50)txt,nrp
      read(1,50)txt,nr0
      read(1,50)txt,eta
      read(1,50)txt,sigp
      read(1,50)txt,sig0
      read(1,50)txt,tau1
      read(1,50)txt,tau2
      read(1,50)txt,omega
      read(1,50)txt,alfi
      close(unit=1)
C Done with 'eryaglaser.prm'.
C Get Er concentration from terminal.
      print*,'Concentration in % :'
      read*,clo
C Get temperature from terminal.
      print*,'Temperature in K :'
      read*,tlo
C Calculate the boltzmann factors of the upper and lower lasing levels.
      call boltzmann(tlo,fa,fb)
C See (4.4.3) and (4.5.4).
      a=tau1*omega*clo**3.
C See (4.4.4).
      g=fa/fb
C See (4.4.5).
      u=tau2/tau1
C Calculate inversion threshold populations and pumping (4.4.8-10).
      qa=2.*a*g*g*u
      qb=1.+(1.+u)*g
      qc=1.
      if (2.*qa*qc.lt.qb/100.) then
        n0inv=qc/qb
      else
        n0inv=(sqrt(qb*qb+4.*qa*qc)-qb)/2./qa
      end if
      n1inv=g*n0inv
      x2inv=g*(1.+a*n1inv)
      xinv=sqrt(x2inv)
C See (4.4.18)
      h1=1.+2.*u*x2inv
      h2=1.-(1.+u)*n1inv-2.*u*a*n1inv*n1inv
      dn1dx=2.*xinv*h2/(2.*a*h1*n1inv+1.+(1.+u)*x2inv)
C See (4.4.17).
      chi=((h1+g*(1.-u))*dn1dx+4.*u*xinv*n1inv)/h1
C Get pumping range from the terminal.
```

```
C "v" is dimensionless pumping normalized to inversion pumping.
      print*,'Normalized pumping range; lo, hi, steps :'
      read*,vlo,vhi,vstp
      vinc=(vhi-vlo)/vstp
C Open output files.
      open(unit=1,file='delta.exact')
      open(unit=2,file='delta.aprox')
C Begin loop.
      do 100 iv=0,vstp
      v=vlo+iv*vinc
      x=xinv*v
      x2=x*x
C See (4.4.13).
      qa=a*(1.+2.*u*x2)
      qb=1.+(1.+u)*x2
      qc=x2
      if (2.*qa*qc.lt.qb/100.) then
        nle=qc/qb
      else
        nle=.5*(sqrt(qb*qb+4.*qa*qc)-qb)/qa
      end if
C See (4.4.14).
      n0e=(1.-(1.-u)*nle)/(1.+2.*u*x2)
C Calculate exact inversion population.
      dlte=nle-g*n0e
      write(1,*)v,dlte
C Calculate approximate inversion population.
      dlta=chi*(x-xinv)
      write(2,*)v,dlta
100   continue
      close(unit=1)
      close(unit=2)
      stop
50    format(A45,T50,E12.6)
      end
C*****************************************************************************
      subroutine boltzmann(t,fa,fb)
C Calculates the boltzmann factors of the upper and lower lasing levels.
      integer i
      real t,tb,fa,fb,ea(2:8),eb(2:7)
C Er:YAG manifold 0 energy levels in 1/cm.
      data ea/19.,57.,76.,411.,424.,523.,568./
C Er:YAG manifold 1 energy levels in 1/cm.
      data eb/52.,58.,235.,256.,274.,335./
C Convert temperature from Kelvin to inverse centimeters.
      tb=.6947*t
C Calculate the Boltzmann factors for lower and upper lasing levels.
      fa=1.
      do 8000 i=2,8
      fa=fa+exp(-ea(i)/tb)
8000  continue
      fa=exp(-ea(7)/tb)/fa
      fb=1.
      do 9000 i=2,7
      fb=fb+exp(-eb(i)/tb)
9000  continue
      fb=exp(-eb(3)/tb)/fb
      return
      end
```

```fortran
C OVERLAP by Geoffrey Wilson 14 August 1989
C
C Calculates normalized overlap integral between the pump beam
C and the cavity mode as a function of the pump beam confocal
C parameter normalized to the rod length and the ratio of
C waist area of the cavity mode to the waist area of the pump beam.
C Used to generate figure 5.3.1. See section 5.3.
C
      integer i
      real lam0,lamp,nr0,nrp,c1,c2,bpbyl,gamma,q,g,zeta
      character*4 fn
C Diode laser pumped Er:YAG laser data.
      lam0=1.645
      lamp=0.788
      nr0=1.809
      nrp=1.824
C See (5.3.4).
      c1=lam0*nrp/lamp/nr0
      c2=c1*c1
C Get output filename and pump confocal parameter normalized to rod
C length from the terminal.
      print*,'fn,bpbyl'
      read*,fn,bpbyl
      open(unit=1,file=fn)
      do 100 i=-25,25
      gamma=5.**(i/25.)
C See (5.3.3-5).
      q=1.+c2/gamma
      g=1.+gamma
      zeta=2.*sqrt(c1)*atan(sqrt(q/g)/bpbyl)/sqrt(g*q*atan(1./bpbyl)*
     &atan(c1/gamma/bpbyl))
      write(1,*)gamma,zeta
100   continue
      close(unit=1)
      stop
      end
```

APPENDIX B

B.1 Single Stripe Diode Lasers

Single stripe diode lasers exhibit waveguiding in both transverse dimensions, designated x for perpendicular and y for parallel to the plane of the epitaxial growth layers. Index-guiding is built into the epitaxial structure in the x dimension and the cavity mode is tightly-bound ($w_x \approx 0.5$ μm). In the y dimension, either index- or gain-guiding is used and $w_y \approx 2$ μm. The lasers usually operate in the fundamental mode in both dimensions, with the electric field polarized in the y direction (TE_{00} mode).

Since w_x, $w_y \approx \lambda_p$, the pump beam rapidly diffracts in both dimensions upon emergence from the diode laser. This is incompatible with minimizing the pumped volume in accordance with the difficulties of Er:YAG discussed in Section 5.2. Diffraction of the pump beam can be controlled by optics coupling the pump to the gain medium, or waveguiding in the gain medium.

An example of the first option is the end-pumped rod discussed in Chapter 5. The bulk Er:YAG provides no waveguiding, so an optical system is required to magnify the pump beam and remove its ellipticity.

The second option is exemplified by end-pumped Er:glass fibers, where both the pump beam and the cavity mode are guided within the fiber.

The output from a stripe diode laser is conveniently and accurately approximated by a TE_{00} elliptical gaussian beam emerging at the $z=0$ plane

and propagating along the $+z$ axis

$$\vec{u}(x,y,z) = \hat{y} \exp(-jkz)U(x,y,z) \qquad \text{(B.1.1)}$$

where $\hat{y}$ is the unit vector in the transverse dimension parallel to the epi-layers, $k \equiv 2\pi/\lambda_p$ and $U(x,y,z)$ is given by Equation C.1.

The unknown parameters $w_{x(y)}$ can be found from the measured far-field half-intensity half-angles $\theta_{1/2,x(y)}$ using Equation C.13.

An elliptical gaussian beam with waist at z-s can be characterized by a parameter[49]

$$q(z) \equiv s+jb \qquad \text{(B.1.2)}$$

for each transverse dimension. An elliptical beam has $b_x \neq b_y$, an astigmatic beam has $s_x \neq s_y$. The properties are independent and undesirable for good matching with a diffraction-limited minimum-volume circular gaussian cavity mode.

The output of an edge-emitting phased array diode laser can be modeled as the sum of n individual identical elliptical gaussian beams distributed evenly along the junction plane, with n-1 relative phases. It then becomes necessary to keep track of the transverse displacement y of the central ray of each emitter relative to the optical (z) axis, and its rate of change $y' \equiv dy/dz$. In all cases discussed here, $x=0$ and $x'=0$.

Figure 5.5.1 indicates that nearly 800 mW of CW pump power is required to yield the target power output of 50 mW, Depending on the efficiency of the coupling optics, the single stripe diode laser output must be at least this large. This is well beyond that which has been achieved to date,

and indeed, cannot reasonably be hoped for since the axial intensity at the output facet is

$$I(axial) = \frac{2}{\pi} \frac{P_{pump}}{w_x w_y} \approx 50 \ \frac{MW}{cm^2} \qquad (B.1.3)$$

which is well beyond the catastrophic failure limit.

Since single stripe devices cannot be used in the target device, no further consideration will be given to them in this work. They may be useful to pump lower power Er:YAG lasers in the development phase alluded to in the final paragraph of Chapter 6, as a convenient alternative to dye laser pumping.

Possible pumps include edge-emitting phased array diode lasers operating in-phase, and grating surface-emitting phased array diode lasers. These are discussed in Sections B.3 and B.4, respectively. A formalism for developing coupling optics systems is presented in Section B.2.

B.2   ABCD Matrix Formalism

A paraxial ray can be characterized at some plane z by (x,x',y,y'). An optical component can be characterized by the way it transforms the ray at the entrance plane into the ray at the exit plane. The transformations can be represented by a pair of ABCD matrices, which have the following action

$$\begin{bmatrix} y_{out} \\ y_{out}' \end{bmatrix} = \begin{bmatrix} A & B \\ C & D \end{bmatrix} \begin{bmatrix} y_{in} \\ y_{in}' \end{bmatrix} \qquad (B.2.1)$$

and similarly for the x dimension. Components with azimuthal symmetry

have $(ABCD)_x = (ABCD)_y$. ABCD matrices are unitary $(AD\text{-}BC{=}1)$ and a reversed component (entrance plane → exit plane) can be represented by interchanging the main diagonal elements (ABCD→DBCA). The action of element #1 followed by the action of element #2 can be described by the product matrix

$$\begin{bmatrix} A & B \\ C & D \end{bmatrix} = \begin{bmatrix} A_2 & B_2 \\ C_2 & D_2 \end{bmatrix} \begin{bmatrix} A_1 & B_1 \\ C_1 & D_1 \end{bmatrix} \tag{B.2.2}$$

ABCD transform the q-parameters of an elliptical gaussian beam as follows

$$q_{y,out} = \frac{Aq_{y,in}+B}{Cq_{y,in}+D} \tag{B.2.3}$$

and similarly for the x dimension.

The ABCD matrix for an air space of length d is

$$\begin{bmatrix} 1 & d \\ 0 & 1 \end{bmatrix} \tag{B.2.4}$$

and that of a spherical thin lens with focal length f is

$$\begin{bmatrix} 1 & 0 \\ -1/f & 1 \end{bmatrix} \tag{B.2.5}$$

Both have azimuthal symmetry and are invariant under reversal.

Equations B.2.4 and B.2.5 can be combined to find the matrix that transfers rays from the front focal plane to the back focal plane of a spherical thin lens

$$\begin{bmatrix} 0 & f \\ -1/f & 0 \end{bmatrix} \tag{B.2.6}$$

If the incoming beam waist is in the front focal plane, then $q_{in}=jb_{in}$, where b_{in} is the confocal parameter of the input beam. The outgoing beam waist will be in the back focal plane and given by

$$b_{out} = \frac{f^2}{b_{in}} \rightarrow w_{out} = \frac{\lambda_p f}{\pi w_{in}} \qquad (B.2.7)$$

Two of these focal-plane-to-focal-plane units cascaded has the composite matrix

$$\begin{bmatrix} -f_2/f_1 & 0 \\ 0 & -f_1/f_2 \end{bmatrix} \qquad (B.2.8)$$

$$b_{out} = M^2 b_{in} \rightarrow w_{out} = M w_{in} \qquad (B.2.9)$$

where lens #1 comes first and $M \equiv f_2/f_1$ is the transverse magnification.

B.3   Edge-Emitting Phased Array Diode Laser Pumps and Coupling Optics

In the following section, edge-emitting phased array diode lasers are taken to consist of n identical stripes, lying parallel in the y-z (p-n junction) plane with a center-to-center spacing of S between nearest neighbors. n is restricted to be even, and S is somewhat larger than w_y (S=10 μm is typical).

The normalized beam emitted by the array is

$$\bar{a}(x,y,z) = \frac{1}{n^{1/2}} \sum_{m=-n+1,\ m\ odd}^{n-1} \exp(-j\phi_m)\ \bar{u}(x,y-y_m,z) \qquad (B.3.1)$$

where the mth stripe is centered at

$$y_m = \frac{S}{2}m \qquad (B.3.2)$$

and has a relative phase ϕ_m.

Imaging the beam onto the Er:YAG rod will not work. This is because M_y cannot be made small enough to compress the array image into the necessary ≈ 40 μm half-width region without beam diffraction, which depends on the waist size of the individual stripe beams, becoming too rapid.

Another approach is to image the array beam in the x dimension, but use the far-field of the beam in the y dimension[50]. This requires using an array whose emitters operate in phase with each other, so that the far-field pattern has a single central lobe. No such device with a CW output of 1 W has yet been reported to the best of the author's knowledge, but there is no fundamental limitation as in the case of the single-stripe diode laser and the coupling optics system is presented in the hope that a suitable device will be developed.

A workable design is shown in Figure B.3.1. The array is assumed to have $w_x = 0.5$ μm, $w_y = 2$ μm, $S = 10$ μm and $n = 10$. Increasing n decreases the power per stripe needed, but makes it more difficult to maintain in-phase operation across the entire width of the device. Perhaps some other number of stripes would be optimum.

L1, L2 and L4 are plano-convex spherical lenses, but L3 is a plano-convex cylindrical lens with focusing in the x dimension. The overall magnification constraint is

$$M_x = \frac{f_2 f_4}{f_1 f_3} = 80 \tag{B.3.3}$$

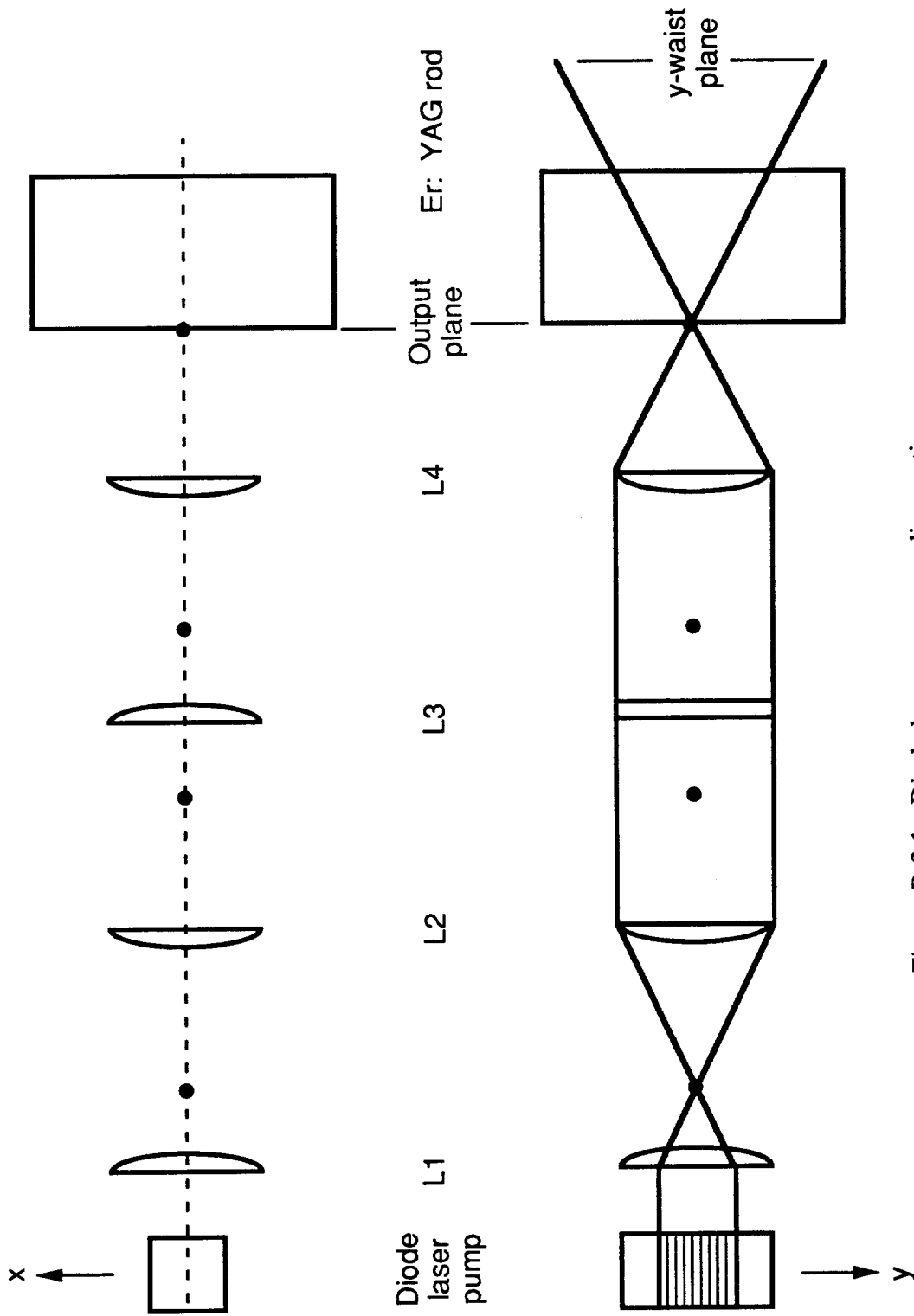In the y dimension, the central rays of the emitters converge at the back focal

Figure B.3.1: Diode laser array coupling optics

point of L4 (output plane). The central ray of the mth emitter emerges at an angle

$$\theta_m \approx \frac{f_2}{f_1} \frac{y_m}{f_4} \qquad (B.3.4)$$

with the z axis, where a small-angle approximation has been made. The beam parameter in the output plane is

$$q_y(\text{out}) = [-1+jB]\frac{f_4^2}{2f_3} \qquad B \equiv \frac{f_2^2 b_y(\text{in})}{2f_1^2 f_3} \qquad (B.3.5)$$

to first order in $B \ll 1$, which can be shown to hold for any case of interest. The quantity $[-1+jB]$ indicates that the beam waists are many confocal parameters to the right of the output plane, in the plane designated "y-waist" in Figure B.3.1. Using Equation B.3.1, the confocal parameter is

$$b_y(\text{out}) = \frac{M_x^2}{4}b_y(\text{in}) = 25.5 \text{ mm} \qquad (B.3.6)$$

using assumed parameter values. The spot size in the output plane is

$$w_y(\text{out}) = \frac{\lambda_p}{\pi w_y} \frac{f_1 f_4}{f_2} \qquad (B.3.7)$$

Because of their mutual coherence, the emitter beams interfere in any region where they overlap. The electric field of the beam is

$$\bar{a}(x,y) = \frac{1}{n^{\frac{1}{2}}} \sum_{m=-n+1,\, m \text{ odd}}^{n-1} \exp(-j\phi_m)\, \bar{u}(x, y\cos\theta_m, y\sin\theta_m) \qquad (B.3.8)$$

in the output plane, where $z \equiv 0$. Using small angle approximations and ignoring small variations in amplitude in favor of small phase shifts,

$$\bar{a}(x,y) \approx \frac{1}{n^{\frac{1}{2}}}\bar{u}(x,y,0) \sum_{m=-n+1, \, m \text{ odd}}^{n-1} \exp(-j\phi_m)\exp(-jky\theta_m) \qquad \text{(B.3.9)}$$

Summing over m and squaring, for an in-phase array (ϕ_m=0)

$$|a(x,y)|^2 = \frac{1}{n}|u(x,y,0)|^2 \frac{\sin^2(\pi nySf_2/\lambda_p f_1 f_4)}{\sin^2(\pi ySf_2/\lambda_p f_1 f_4)} \qquad \text{(B.3.10)}$$

and for an out-of-phase array (ϕ_m=i^m)

$$|a(x,y)|^2 = \frac{1}{n}|u(x,y,0)|^2 \frac{\sin^2(\pi nySf_2/\lambda_p f_1 f_4)}{\cos^2(\pi ySf_2/\lambda_p f_1 f_4)} \qquad \text{(B.3.11)}$$

The out-of-phase far-field has two major lobes, which may be useful in pumping a TEM_{10} cavity mode but is of no use in pumping a TEM_{00} cavity mode and will not be discussed further.

The in-phase far-field has a central lobe with a $1/e^2$ half-width of

$$W \approx 0.70 \frac{\lambda_p f_1 f_4}{nSf_2} \qquad \text{(B.3.11)}$$

assuming that $W << w_y(\text{out})$, which is always the case.

The design process begins by setting $W=w_x$=40 μm and combining Equations B.3.11 and B.3.3 to get

$$\frac{f_4^2}{f_3} = \frac{M_x WnS}{0.70 \, \lambda_p} = 580 \text{ mm} \qquad \text{(B.3.12)}$$

To minimize the overall length without making any one focal length too short, it is sensible to set

$$f_1 = f_3 \qquad f_2 = f_4 \quad \rightarrow \quad \frac{f_2}{f_1} = \frac{f_4}{f_3} = \sqrt{M_x} \qquad \text{(B.3.13)}$$

Then $f_{1,3}$=7.25 mm and $f_{2,4}$=65 mm. The spot size in the output plane is found using Equation B.3.7 to be w_y(out)=910 μm, which is indeed much greater than W.

At the far end of the rod, the central rays of the outer emitters are

$$\Delta y = \frac{f_2(n-1)SL_{rod}}{f_1 f_4 n_{r,p}} = 33.3 \ \mu m \qquad (B.3.14)$$

apart. This separation is small compared to w_y(out), so the beams continue to interfere with about the same lobe width along the entire length of the rod.

B.4   Grating Surface Emitter Pumps

Coherent emission from large apertures has been obtained from grating surface—emitters[51] with near diffraction-limited beam divergences and single-lobe far-fields in both transverse dimensions, indicating in-phase operation.

An idealized model considers the emission to be of constant phase and amplitude across a square aperture with side A. If the aperture is in the front focal plane of a spherical lens with focal length f, the far-field pattern appearing in the back focal plane is the product of identical "sinc" functions in each transverse dimension[52], with $1/e^2$ half-widths

$$w_p = 0.70 \ \frac{\lambda_p f}{A} \qquad (B.4.1)$$

which have been designated w_p in anticipation of their approximate correspondence to a circular gaussian waist size. Inserting w_p=40 μm and λ_p=788 nm gives f/A=73. Therefore, f=6.5 mm could be used if A=900 μm, a reasonable size for multiple-section grating surface emitter.

Although CW operation of grating surface emitters has not yet been achieved, it is expected to be soon forthcoming and 1 W power outputs are within reach[53].

APPENDIX C

$U(x,y,z)$ of Equation B.1.1 is given by

$$U(x,y,z) = \left[\frac{2}{\pi}\right]^{\frac{1}{2}} \exp\left[-\frac{j}{2}\tan^{-1}\left(\frac{z}{b_x}\right)\right] \frac{1}{w_x^{\frac{1}{2}}(z)}\exp\left[-\frac{x^2}{w_x^2(z)}\left(1+j\frac{z}{b_x}\right)\right] \times$$

$$\exp\left[-\frac{j}{2}\tan^{-1}\left(\frac{z}{b_y}\right)\right] \frac{1}{w_y^{\frac{1}{2}}(z)}\exp\left[-\frac{y^2}{w_y^2(z)}\left(1+j\frac{z}{b_y}\right)\right] \quad\quad (C.1)$$

where

$$w_{x(y)}(z) \equiv w_{x(y)}\left[1+\frac{z^2}{b_{x(y)}^2}\right]^{\frac{1}{2}} \quad\quad (C.2)$$

and

$$b_{x(y)} \equiv \frac{\pi w_{x(y)}^2}{\lambda_p} \quad\quad (C.3)$$

where $w_{x(y)}$ are the waist sizes of the beam.

$U(x,y,z)$ is a solution of the paraxial Helmholtz equation

$$\left[\nabla_t^2 - 2jk\frac{\partial}{\partial z}\right] U(x,y,z) = 0 \quad \nabla_t^2 \equiv \frac{\partial^2}{\partial x^2} + \frac{\partial^2}{\partial y^2} \quad\quad (C.4)$$

which assumes that

$$\left|\frac{\partial^2 U}{\partial z^2}\right| \ll \left|2k\frac{\partial U}{\partial z}\right| \quad\quad (C.5)$$

This holds if

$$2k \gg \frac{\partial}{\partial z} \approx \frac{1}{b_{x(y)}} \quad \rightarrow \quad \frac{\lambda_p}{2\pi} \ll w_{x(y)} \quad\quad (C.6)$$

which is marginally true in the present situation because $\lambda_p/2\pi \approx 1/8$ μm, $w_x = .5$ μm and $w_y = 2$ μm.

$U(x,y,z)$ is normalized such that

$$\int_{-\infty}^{+\infty} dx \int_{-\infty}^{+\infty} dy \mid U(x,y,z) \mid^2 = 1 \qquad (C.7)$$

This is allowed because of the conservation of the quantity on the left hand side:

$$\frac{\partial}{\partial z} \int_{-\infty}^{+\infty} dx \int_{-\infty}^{+\infty} dy \mid U(x,y,z) \mid^2 = \frac{1}{2jk} \int_{-\infty}^{+\infty} dx \int_{-\infty}^{+\infty} dy \; [U^* \nabla_t^2 U - U \nabla_t^2 U^*] = \quad (C.8)$$

$$\frac{1}{2jk} \int_{-\infty}^{+\infty} dx \int_{-\infty}^{+\infty} dy \; \nabla_t \cdot [U^* \nabla_t U - U \nabla_t U^*] = \frac{1}{2jk} \int_{R \to \infty} dC \; \hat{n} \cdot [U^* \nabla_t U - U \nabla_t U^*] = 0$$

where the first equality comes from taking the partial derivative inside the integrals and using Equation C.4 and the second comes from factoring $\nabla_t \cdot$. The third step is to use the divergence theorem, where C is a circular path centered on the z axis with radius R in the z=constant plane and $\hat{n}$ is the outward normal unit vector to path C. The line integral vanishes as $R \to \infty$ because of the rapidly diminishing gaussian function $U(x,y,z)$.

Although it is conserved across all z=constant planes, $\mid U(x,y,z) \mid^2$ is not precisely proportional to the intensity. The Poynting vector is

$$\bar{s} \propto \frac{j}{2k} [\bar{u}^* \times \nabla \times \bar{u} - \bar{u} \times \nabla \times \bar{u}^*] \qquad (C.9)$$

The flux in the direction of propagation is

$$\bar{s} \cdot \hat{n} = \mid U \mid^2 + \frac{j}{2k} \left[U^* \frac{\partial U}{\partial z} - U \frac{\partial U^*}{\partial z} \right] \approx \mid U \mid^2 \qquad (C.10)$$

where Equation C.6 justifies the neglect of the second term.

In the far field $(z >> b_{x(y)})$, this becomes

$$\vec{s}\cdot\hat{n} \rightarrow \frac{2\pi w_x w_y}{\lambda_p^2 z^2} \exp\left[-2\left(\frac{\pi w_x}{\lambda_p}\right)^2 \tan^2\theta_x\right] \exp\left[-2\left(\frac{\pi w_y}{\lambda_p}\right)^2 \tan^2\theta_y\right] \quad (C.11)$$

where

$$\tan\theta_{x(y)} \equiv \frac{x(y)}{z} \quad (C.12)$$

If $\theta_{\frac{1}{2},x(y)}$ is defined as the angle in the z-x(y) plane at which the intensity in the z=constant plane has decreased to half of its value on the axis, then

$$w_{x(y)} = \left[\frac{\ln(2)}{2}\right]^{\frac{1}{2}} \frac{\lambda_p}{\pi\tan\theta_{\frac{1}{2},x(y)}} \quad (C.13)$$

VITA

Geoffrey A. Wilson was born in Riverside, California on January 14, 1959. He received the B.S. degree (Cum Laude, Distinction) from Sonoma State University, Rohnert Park, California in June, 1984. In April 1987, he began his studies at Oregon Graduate Institute of Science and Technology.